

THE PROBLEMATIC ASPECTS OF ENERGY EFFICIENCY '21

EDITORS

MACIEJ ZAJKOWSKI • ZBIGNIEW SOŁJAN



THE PROBLEMATIC ASPECTS OF ENERGY EFFICIENCY '21

Editors
Maciej Zajkowski, Zbigniew Sołjan



OFICyna WYDAWNICZA POLITECHNIKI BIAŁOSTOCKIEJ
BIAŁYSTOK 2021

Reviewers:
Assoc. Prof. Krzysztof Siwek, PhD, DSc, Eng
Marcin Wesołowski, PhD, DSc, Eng

Science editor in the discipline of automation, electronic and electrical engineering:
Prof. Jan Dorosz, PhD, DSc

Copy editor:
Emilia Kiszycka

DTP & cover of a book:
Marcin Dominów

© Copyright by Białystok University of Technology, Białystok 2021

ISBN 978-83-66391-69-7 (eBook)
DOI: 10.24427/978-83-66391-69-7



The publication is available on license Creative Commons Recognition of authorship
– Non-commercial use – Without dependent works 4.0 (CC BY-NC-ND 4.0)

Full license content available

on the site creativecommons.org/licenses/by-nc-nd/4.0/legalcode.pl.

The publication is available on the Internet
on the site of the Publishing House of Białystok University of Technology.

Publishing House of Białystok University of Technology
Wiejska 45C, 15-351 Białystok
e-mail: oficina.wydawnicza@pb.edu.pl
www.pb.edu.pl

Table of contents

Introduction.....	4
Chapter 1	
Selection of ESP32 operating parameters in order to reach optimal energy efficiency during calculations	5
Chapter 2	
The new method of measuring the complex value of short circuit loop impedance	14
Chapter 3	
Light pollution from small sports facilities	23
Chapter 4	
Decomposition of the load's current supplied from a sinusoidal and asymmetrical voltage source in accordance with the Currents' Physical Components (CPC) Theory	35
Chapter 5	
Improving the cooling efficiency of industrial electronic components with the use of planar porous heat sinks.....	53
Chapter 6	
Luminance contrast distribution analysis in selected pedestrian crossings configurations.....	65
Chapter 7	
Low voltage electrical installations – energy efficiency functional aspects.....	76
Chapter 8	
The impact of electric energy receivers used in modern households on energy efficiency in the low-voltage network.....	86
Chapter 9	
The numerical analysis of the influence of geometry planar coil systems on the efficiency of the WPT system.....	100
Chapter 10	
Estimation of the maximum load power in periodic WPT systems.....	111
List of Tables.....	125
List of Figures.....	126

Introduction

The purpose of this monograph is the issue of energy efficiency, which, according to Article 2 of the Journal of Laws 2021.468, means "the ratio of the achieved magnitude of the useful effect of a given object, technical device or installation, under typical conditions of its use or operation, to the amount of energy consumption by this object, technical device or installation, or as a result of the performed service necessary to achieve this effect." This definition encompasses a wide range of technical, technological, managerial, and social solutions, so it allows energy efficiency policy to be implemented in its broad horizon.

Elements related to energy efficiency are present around us and within us, even when we are unaware of their presence. A mundane example of energy efficiency is our body's reaction to a cold floor - we put on our slippers. We lose the most heat through our feet, so in order to maintain the heat balance, we need to provide thermal energy by e.g.: drinking warm tea, taking a warm bath, increasing the temperature on the furnace or radiator, etc. However, the easiest way is to increase the heat resistance by wearing soft, comfortable house shoes, which will insulate your feet from the cold floor and create an energy-efficient effect.

The structure of the monograph is very simple and contains 10 articles related to energy efficiency. The issues addressed in the publication are thematically different, but their common denominator, in addition to the aforementioned energy efficiency, is the area of electricity-using technologies. The articles cover issues including wireless transmission of electricity, modern lighting techniques for pedestrian crossings, or topics related to light pollution or reactive power compensation problems.

Chapter 1

Selection of ESP32 operating parameters in order to reach optimal energy efficiency during calculations

*Agnieszka Choroszucho, Jakub Bednarek, Mateusz Sumorek and Jakub Żukowski
Bialystok University of Technology, Faculty of Electrical Engineering*

In the era of technological processes automation development, the popularization of house automation, constant limitation of human participation in these processes, as well as the intensification in the field of broadly understood IoT, such devices are increasingly used for remote monitoring and control of various processes. In recent years, the ESP32 platform has gained a significant increase in the popularity of the IoT market. It is often used for logging and remote controlled devices, mostly in smart home solutions. Such devices often have to be small and have long battery work-time. The test results presented in the article will allow for a proper selection of working parameters in order to achieve the most optimal energy efficiency (smallest losses) while performing the assumed task.

Index terms: embedded system, ESP32, Internet of Things, energy efficiency, smart homes, automation.

Introduction

The development of the automation of technological processes and the need for their remote monitoring, a growing popularity of smart home solutions and the collection of data derived from them is associated with the emergence of various needs. Growing interest in the broadly understood IoT results in the emergence of increasingly newer solutions from manufacturers striving to create the most comprehensive system. In recent years, the ESP32 family from Espressif Systems has gained particular popularity. It is a microcontroller based on an efficient 32-bit Xtensa LX6 microprocessor [1] equipped with a Wi-Fi and Bluetooth version 4.2. Thanks to these built-in functionalities, low price, refined documentation and large support of the constructor community, this system is very popular in such solutions as smart homes or remote data collection (e.g. logging of temperature and pressure measurement sensors).

Devices that are created for such purposes must meet certain requirements. The most common ones are small dimensions and the longest possible battery life. Despite the very dynamic development and well-developed battery solutions, it is still difficult to reconcile these two requirements. Thanks to the development of micro-processor systems, they are able to be very energy efficient. Currently, most solutions have a built-in sleep mode. The ESP32 microcontroller in sleep mode is able to limit power consumption to tens or even single μA [1]. This allows to significantly extend the on-battery lifetime of the device. Unfortunately, in this state the device is not able to perform any demanding tasks – only after waking up it can take the assumed actions, which is associated with increased power consumption.

This article presents the results of conducted research. They show with which operating parameters the lowest energy consumption can be obtained during the execution of an algorithm. This is to extend the device’s operating time while using battery-based power.

Research assumptions

A proper selection of the device’s operating parameters allows to extend its operating time without having to replace the battery or recharge it. Due to this procedure, maintenance work can be carried out less often. This is particularly important when the device is mounted in a hard-to-reach place. The limitation of servicing results in lower operating costs, which is primarily noticeable in large, distributed installations or systems.

In order to select the optimal operating parameters, the measurements of the algorithm execution time and the current consumption of the device were carried out during this process. These measurements concerned different values of the microcontroller clock speed and voltage of different values. As a calculation algorithm, the calculation of the π number was used in accordance with formula (1.1) [7]:

$$\pi = 4 \cdot \sum_{n=1}^{\infty} \frac{(-1)^{n-1}}{2n-1} = 4 \cdot \left(1 - \frac{1}{3} + \frac{1}{5} - \frac{1}{7} + \frac{1}{9} - \dots \right). \quad (1.1)$$

Figure 1.1 presents the algorithm written in MicroPython language [2], characterized by low computational efficiency [3], especially where the algorithm uses iterative methods [5, 6].

In connection with the fact that formula (1.1) is a slow convergent method [4] (requiring a large amount of iteration to achieve a satisfactory result), a significant load on the processor was forced, resulting in a significant increase in current consumption.

```

1. count = 0
2. machine.freq(24000000) #taktowanie zegara
3.
4. while(count < 1):
5.
6.     print('start')
7.     start = time.ticks_ms()
8.     a = 0
9.     for i in range (125000):
10.        a += ((-1)**i)/(2*i+1)
11.    end = time.ticks_ms()
12.    print(end - start) #zwróć czas obliczeń
13.    print(4*a)
14.    count = 1

```

FIGURE 1.1. Algorithm used to calculate the number of π .

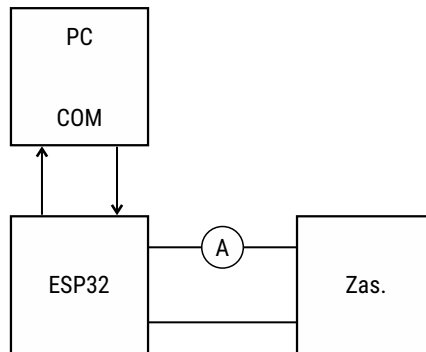


FIGURE 1.2. Measurement diagram, PC, ESP32 – tested microcontroller, Zas – laboratory power supply.

Two factors were selected as set parameters of the ESP32 microcontroller: supply voltage and clock speed of the processor. The value of the supply voltage, according to the manufacturer’s documentation, should be in the range $\langle 2.7; 3.6 \rangle$ V (current recommendation of the manufacturer is 3.0 V – 3.6 V) [1]. In tests, measurements in the range of $\langle 2.7; 3.3 \rangle$ V were conducted. For each given supply voltage, measurements for different clock speeds in the range of 20 – 240 MHz (from available settings options) were performed.

The measurement of the time needed to complete the task and also the time of increased power consumption was made at the level of the algorithm that returned the value to the computer through the serial port (Fig. 1.2). As preliminary current measurements using the oscilloscopic method showed that the current consumed during the calculations is constant during their duration (no fluctuations were noted), it was accepted with satisfactory accuracy that the measurement of the current

value using an ammeter would be appropriate (Fig. 1.2). In the test, the supply voltage of the system using a stabilized power supply was set, which in combination with the current measurement, enabled the determination of energy consumption in mWh during calculations in accordance with formula (1.2):

$$E = U \cdot I \cdot \frac{t}{3600}, \tag{1.2}$$

where:

E – used energy in mWh,

U – supply voltage,

I – current consumption under load,

t – time of algorithm execution.

Results

Figure 1.3 shows the dependence of the calculation time on the processor clock frequency. The curves in Fig. 4 show a family of characteristics of the dependence of consumed energy on the processor clock frequency, taking into account the system supply voltage.

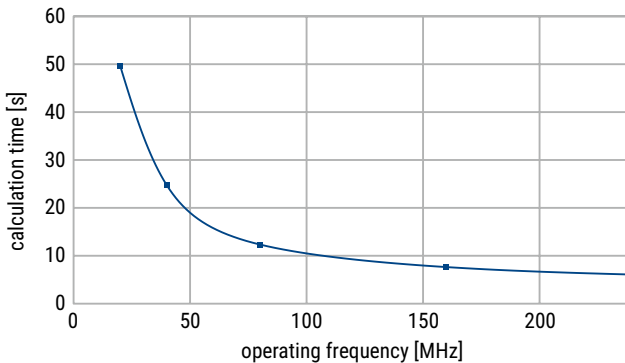


FIGURE 1.3. Characteristics of the dependence of calculation time on clock frequency.

The drawn family of characteristics (Fig. 1.4) allows to observe the linearity of the device’s energy consumption along with the reduction of the processor’s supply voltage.

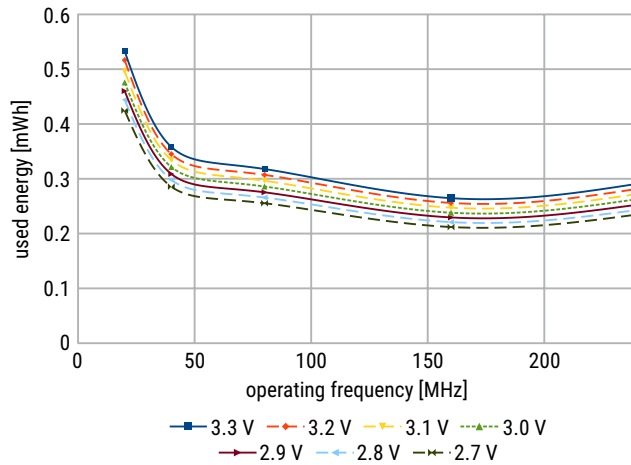


FIGURE 1.4. Family of characteristics showing energy consumption depending on processor clock speed including supply voltage.

Figure 1.5 shows the dependence of the used energy on supply voltage on the processor clock frequency.

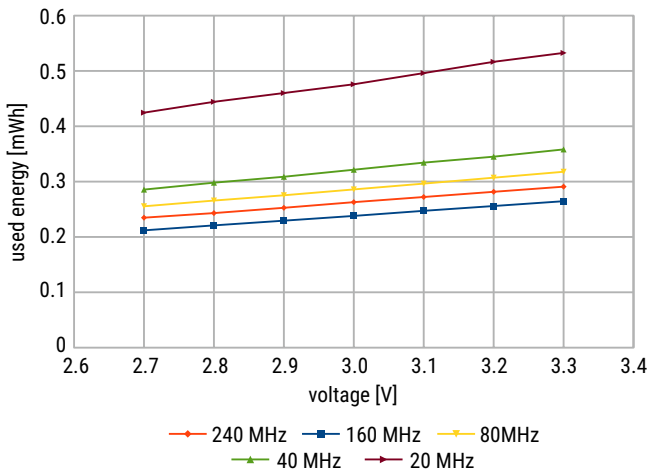


FIGURE 1.5. Family of characteristics showing energy consumption as a function of supply voltage.

Based on the conducted measurements, it can be concluded that supply voltage does not affect the duration of the performed calculations (Table 1.1).

TABLE 1.1. Measurement results

Power supply [V]	Frequency [MHz]	Calculation time [ms]	Used energy [mWh]
3.3	20	49664	0.5326
	40	24729	0.3582
	80	12339	0.3178
	160	7635	0.2646
	240	6068	0.2909
3.2	20	49664	0.5165
	40	24729	0.3451
	80	12339	0.3071
	160	7635	0.2559
	240	6068	0.2816
3.1	20	49664	0.4961
	40	24729	0.3343
	80	12339	0.2964
	160	7635	0.2472
	240	6068	0.2722
3	20	49664	0.4759
	40	24729	0.3215
	80	12339	0.2859
	160	7635	0.238
	240	6068	0.2629
2.9	20	49664	0.4601
	40	24729	0.3088
	80	12339	0.2753
	160	7635	0.2294
	240	6068	0.2527
2.8	20	49664	0.4442
	40	24729	0,2981
	80	12339	0,2658
	160	7635	0.2209
	240	6068	0.2431
2.7	20	49664	0.4246
	40	24729	0.2856
	80	12339	0.2554
	160	7635	0.2119
	240	6068	0.2348

Discussion

Analyzing the processor’s documentation, it can be observed that in its structure at the power input there are linear stabilizers responsible for supplying individual sections of the microcontroller, such a decrease is directly related to them (Fig. 1.6). The losses are proportional to the voltage drop across the voltage regulator. This means that bringing the supply voltage closer to the minimum value that allows an element to work correctly will result in the smallest energy loss on it.

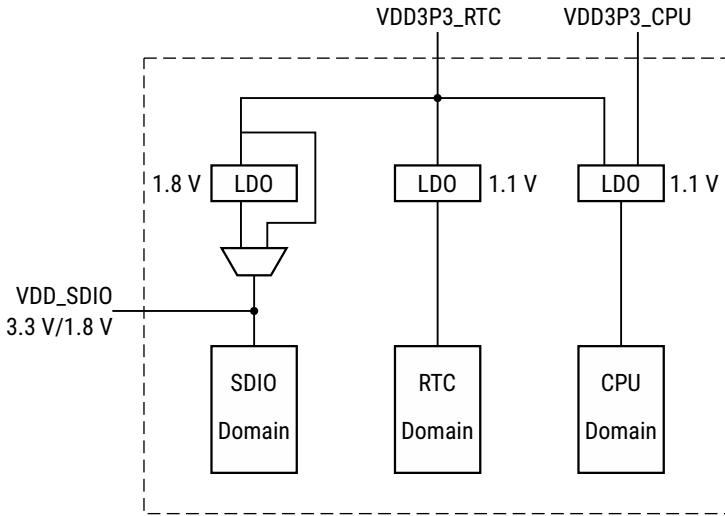


FIGURE 1.6. ESP32 processor power input structure from the manufacturer’s documentation [1]

In Figure 1.4 the presented characteristics clearly show the optimal operating point of the microcontroller, which determines the supply voltage of 2.7 V and the processor clock speed of 160 MHz. This assumption works when the processor uses only basic peripherals for mathematical calculations. With this assumption, energy consumption for carrying out the task equaled 0.211 mWh. The system working with standard parameters, which are 3.3 V and 240 MHz, used 0.263 mWh. A decrease in energy consumption is classified at around 20% relative to the standard operating parameters of the controller. Taking into account the updated recommendations of the ESP32 manufacturer (supply voltage range), it should be in the range of 3.0 V – 3.6 V. The optimal operating point is the following: supply voltage of 3.0 V and clock speed equal to 160 MHz. ESP32 at these parameters consumed 0.238 mWh, which means a decrease in energy consumption by about 10% compared to standard parameters. The characteristics show a significant increase in energy consumption by the microcontroller when operating at low clock frequencies (Fig. 1.3). Despite a significant decrease in the controller’s current consumption at low clock speeds, the calculation time lengthened significantly, resulting in an increase in energy consumption.

Additional characteristics of the dependence of the system's energy consumption are presented in Fig. 4. It was also observed that the exponential increase in calculation time along with a decreased calculation time on the clock operating frequency were drawn up in the article to determine the main impact on the in-clock speed is visible. Based on both characteristics, a significant correlation can be made between them in the low clock frequency range.

Conclusions

The article presents the results of testing energy consumption of the ESP32 microcontroller manufactured by Espressif Systems. The purpose of the measurements was to determine the optimal operating parameters of the system in order to most efficiently use energy to perform a given task, and evaluate the extension of the potential operating time of the device in battery supply conditions. According to the measurements made, the reduction of the clock frequency reduces the value of the current consumed by the microcontroller, but significantly extends the calculation time. The value of the current consumed and the calculation time allow for determining the system's operating parameters at which it is possible to reduce energy consumption by up to 20% as compared to standard operating parameters. The research will be continued using other research methods that take into account different operating conditions of the device.

This work was supported by Ministry of Science and Higher Education in Poland under work No. MB/WE/5/2018.

Authors: A. Choroszucho (e-mail: a.choroszucho@pb.edu.pl), J. Bednarek (e-mail: j.bednarek@student.pb.edu.pl), M. Sumorek (e-mail: mateusz.sumorek@gmail.com) and J. Żukowski (e-mail: jakubzzukowski@gmail.com), Białystok University of Technology, Faculty of Electrical Engineering, Wiejska 45D Str., 15-351 Białystok, Poland.

References

- [1] EspressifSystems. (September 2020). Espressif.com [Online]. Accessed: https://www.espressif.com/sites/default/files/documentation/esp32-wroom-32_datasheet_en.pdf.
- [2] Tollervey N. H., "Programming with MicroPython: Embedded Programming with Microcontrollers and Python," O'Reilly Media (2017).
- [3] A. Choroszucho, P. Golonko, J. Bednarek, M. Sumorek, J. Żukowski, "Comparison of high-level programming languages efficiency in embedded systems," *SPIE 11176, Photonics Applications in Astronomy, Communications, Industry, and High-Energy Physics Experiments 2019*, (6 November 2019); doi: 10.1117/12.2537143, 2019
- [4] Borwein J.M., Borwein P.B., Bailey D.H., "The American Mathematical Monthly," 96(3), 201-219, Mathematical Association of America (March 1989).

- [5] A. Steckiewicz, A. Choroszucho, “Optimization-based synthesis of a metamaterial electric cloak using nonhomogeneous composite materials,” *Journal of Electromagnetic Waves and Applications*, Vol. 33, No. 14, 1933–1941 (2019).
- [6] Thomas H. Cormen, Charles E. Leiserson, Ronald L. Rivest, Clifford Stein, “Introduction to Algorithms,” The MIT Press (1989), pp. 15–38.
- [7] Debnath, Lokenath, “The Legacy of Leonhard Euler: A Tricentennial Tribute,” World Scientific (2009).

Chapter 2

The new method of measuring the complex value of short circuit loop impedance

Grzegorz Hołdyński, Zbigniew Skibko
Białystok University of Technology, Faculty of Electrical Engineering

The article presents the basic assumptions of a new method of measuring the complex value of short circuit loop impedance by the polynomial approximation method. It involves determining the module value and the loop impedance angle and is later based on calculating the resistance and reactance values of the short circuit at the measuring point.

Index terms: measurement of short circuit loop impedance, complex values of short circuit loop impedance, fault resistance and reactance.

The Purpose of Measuring Short Circuit Loop Impedance

The most common means of protection against electric shock in the event of damage is self-acting power-off. It is intended to protect against electric shock as well as to protect the installation and electrical devices against disturbances in their operation or destruction. Protection by self-acting power-off is effective if, in the event of a phase wire short circuit to the enclosure (connected to the protective wire):

- a) a protective device (fuse, over-current circuit-breaker, residual current circuit-breaker) automatically switches off the power supply in the required time;
- b) permissible for regulations of the value of allowable long-term touch voltage U_L is not exceeded.

The maximum allowable power switch-off time in TN network systems was specified in PN-HD 60364-4-41: 2009 [1] and is 0.4 s (for a rated value of phase voltage equal to 230 V). This switch-off time applies to plug-in circuits with a rated current of not more than 63 A, and for the circuits supplying loads which are permanently installed, the rated current cannot be more than 32 A. For distribution circuits, this time may be longer than 0.4 s, but it cannot exceed 5 seconds.

To check compliance (concerning the conditions of protection against electric shock by self-acting power-off) of real systems with the provisions of the PN-HD 60364-4-41 standard should be:

- 1) measure (according to PN-HD 60364-6 [2]) the value of fault loop impedance,
- 2) check compliance of the protective device rating data.

The short circuit loop in a properly made TN system includes a transformer winding, electric wires and cables (on the transformer – load section) and a metal enclosure of the device (Fig. 2.1).

To check the effectiveness of the protection against an electric shock by self-acting switching off the power supply in the TN system, it is necessary to determine whether the measured value of short circuit loop impedance meets the condition [1]:

$$Z_s \leq \frac{U_0}{I_a} \tag{2.1}$$

where:

- Z_s – short circuit loop impedance in the tested system,
- I_a – current of the protection causing power-off in due time,
- U_0 – rated voltage of the network relative to the earth.

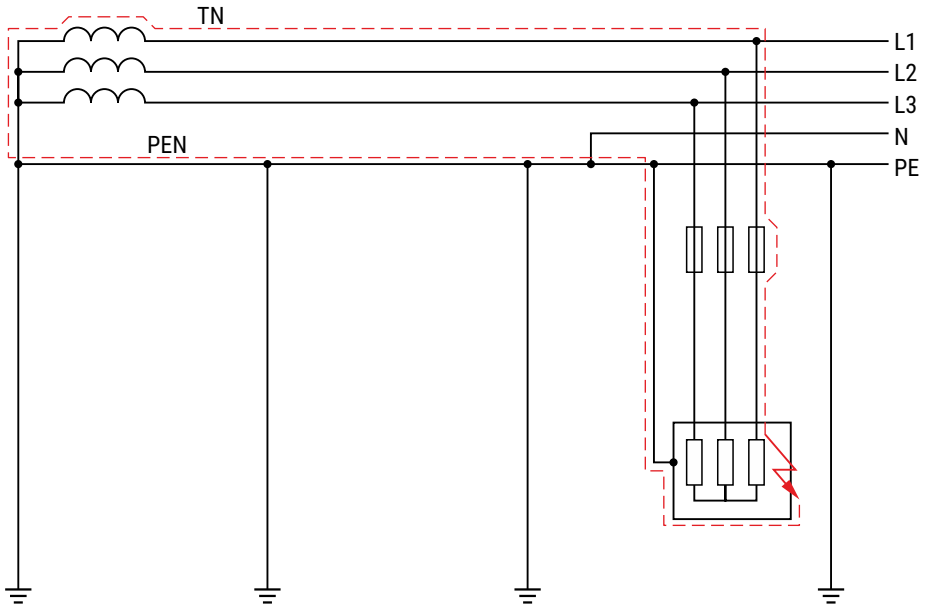


FIGURE 2.1. Short circuit loop L – PE in the TN system [3]

Knowable Methods of Metering Short Circuit Loop Impedance

1. Measurement of short circuit loop impedance using the technical method

The measurement of short circuit loop impedance using the technical method, i.e. using a voltmeter and an ammeter, is shown in Figure 2.2. In this method, the values of resistance R_x and reactance X_x of the tested short circuit loop should be measured separately. The searching impedance of the short circuit loop Z is then the geometric sum of the measured values of resistance and reactance X_x :

$$Z_s \leq \sqrt{R_x^2 + X_x^2} \quad (2.2)$$

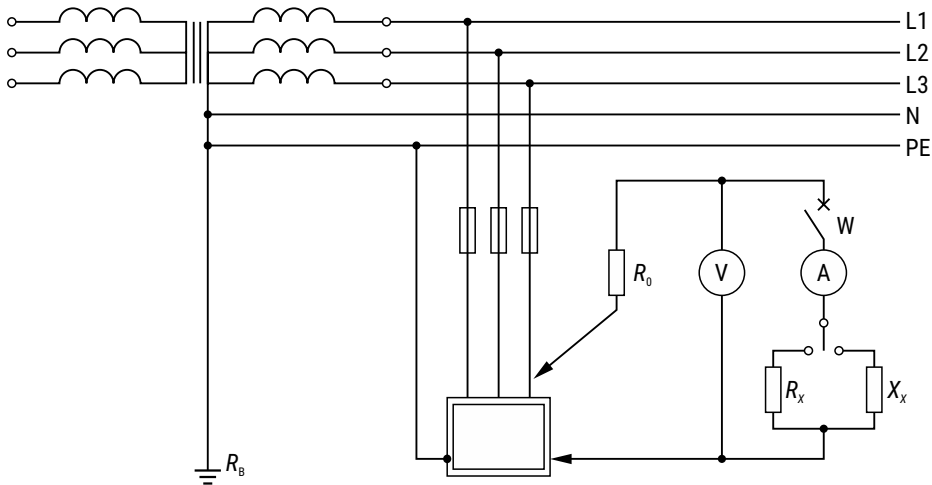


FIGURE 2.2. Measurement of short circuit loop impedance by technical method [3]

When using this method in TN-C systems, there is a risk of dangerous contact voltage loads appearing on the conductive parts. It may occur as a result of a break in the PEN protective conductor.

The technical method of measuring short circuit loop impedance is currently used very rarely.

2. Measurement of short circuit loop impedance using voltage drop method

The circuit for measuring short circuit loop impedance by the voltage drop method (using the so-called “artificial fault”) is shown in Figure 2.3. This is currently the most common way of defining the value of short circuit loop impedance.

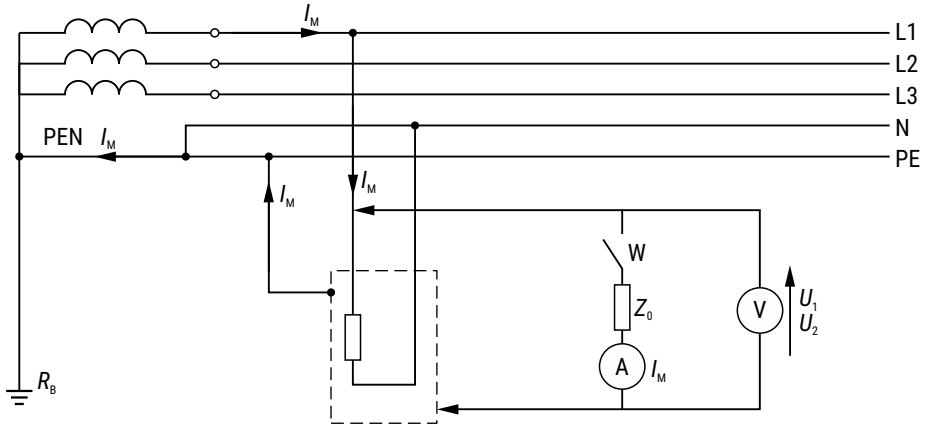


FIGURE 2.3. Measurement of short circuit loop impedance by voltage drop method [3]

In this method, short circuit loop impedance of the studied circuit is defined by switching on, for a short time, of the load with known impedance Z_0 . Then the two voltage values should be measured: U_1 before the measuring load and U_2 – after switching on. The sought value of short circuit loop impedance Z could then be calculated by the formula:

$$\underline{Z} = \underline{Z}_0 \frac{\underline{U}_1 - \underline{U}_2}{\underline{U}_2} = \underline{Z}_0 \left(\frac{\underline{U}_1}{\underline{U}_2} - 1 \right) \quad (2.3)$$

where:

Z – measured impedance,

Z_0 – metering load impedance,

U_1 – voltage measured before switching on the metering load,

U_2 – voltage measured after switching on the metering load.

There are two basic ways to measure the searched values: direct and indirect.

The indirect measurement consists of two stages. In the first stage, using the resistive load, resistance of the investigated circuit is determined. In the second case, reactance of the circuit is determined using the reactance load. The main disadvantage of this method is the complexity of measurement as well as the large size of the measuring instruments, resulting from the release of a significant amount of heat in the resistance during the flow of the measuring current through it. An extension of this method of performing measurements is the use of a resistance-reactance load. The disadvantage of this type of solution is not only the weight and size of the device itself but also time-consuming measurements, resulting from the need to make at least three readings for different sets of X/R values.

The second group of short circuit loop impedance measurement methods includes methods based on a direct measurement of the difference or ratio of the voltage of a tested network in loaded and unloaded conditions. The first way to directly measure the impedance of a short circuit loop is that in one voltage period, the tested circuit is loaded with metering current, and in the next period, the system is without the load. Such measuring cycles are repeated several times, measuring the difference or ratio of the voltage in a loaded and unloaded measuring period, and the phase of the measuring current is adjusted to obtain the highest value of this difference (ratio). The disadvantage of this solution is primarily a step regulation, which introduces a variable measurement error, depending on the value of the measured impedance.

Another method of direct measurement of short circuit loop impedance is the way based on comparing the voltage between the phase wire and the protective wire, with the metering load being on or off. The value of the searched resistance or impedance of the circuit is obtained by dividing the maximum value of the voltage occurring in the system loaded with metering impedance during the one-half period to the peak value of the voltage occurring in the unloaded system measured during one or several half-periods.

Another method to directly measure short circuit loop impedance in low voltage electrical installations is to measure the voltage difference (or ratio) over two half-periods or entire periods of the testing system voltage in which the test circuit alternately loads or does not load the test circuit with the metering current. The measured voltage is saved in a metering system that detects the differences and maximum values of voltage occurring at a metering load or no metering load. The number of load cycles of the system should be selected during the measurement so that the measurement of short circuit loop resistance or impedance takes place within the allowable transient state limits.

The method of direct measurement of short circuit loop impedance, in which the measurement sensitivity to supply voltage distortion is limited consists of measuring, with the metering load being switched off, the values of instantaneous voltages at time t and $t+T/2i$ (where T is the period of supply voltage, and i – harmonic order), from which sums are made and which are the orthogonal component of the unloaded voltage. These operations are repeated as many times as much we want to eliminate harmonics.

To sum up, short-circuit loop impedance measurement systems known to date consist of a measuring load element composed of series-connected thyristor switch and load impedor, to which a measurement and control system element is connected in parallel. The measurement consists of determining the maximum difference (ratio) of voltages in unloaded conditions and under load with the metering current. However, a common disadvantage of such solutions is the uncertainty of measurement strictly dependent on the degree and type of the load occurring in the network and the complexity of the metering systems.

The New Method for Measuring Short Circuit Loop Impedance

The method of metering the complex value of short circuit loop impedance proposed by the authors [4] is based on the measurement of the RMS value of the investigated network voltage, in which the studied system is loaded in one period, and in the second period, the investigated circuit is not loaded by the metering current. During the measurement, an impedor composed of three different known (from module and phase) impedances (Fig. 2.4) is connected to the studied system. The complex value of the sought short circuit impedance of the tested system is determined using a second-degree polynomial.

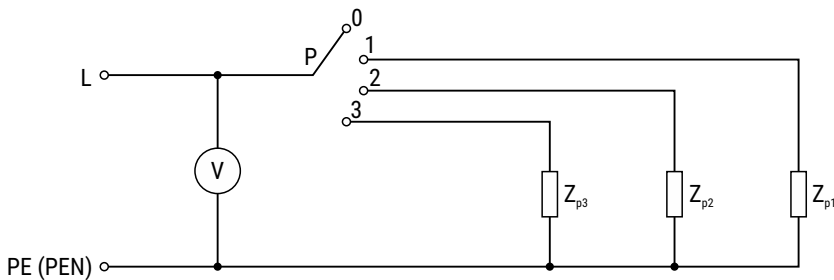


FIGURE 2.4. Scheme showing the idea of measuring short circuit loop impedance [4]

At the first moment of measurement, the RMS value of the low voltage E_{i1} is measured over the full period, after which the first measuring branch with impedance Z_{p1} is switched on. After t_1 time has elapsed since switching on the first load impedance (where t_1 is the time of transient states resulting from switching on impedance), the first RMS value of voltage U_{p1} is measured for the full period. Then after the measuring time T (where T is the voltage period of the investigated system), the first impedance is switched off. After t_1 time, from switching off the measuring impedance, the RMS value of the low voltage network E_{i2} is measured again. If $E_{i2} \neq E_{i1}$, the measurement is repeated from the beginning. If $E_{i2} = E_{i1}$, the RMS value of measuring voltage U_{p1} and the voltage of the network $E_i = E_{i2}$ is saved, and the second measuring branch, with impedance Z_{p2} , is switched on. After t_1 time, from the moment of switching on the second measuring impedance, the second RMS value of voltage U_{p2} is measured for the full period. The same applies to the remaining measuring branches. Based on the measured RMS values of the voltages of the tested network (E_1, E_2, E_3) and the RMS values of voltages (U_{p1}, U_{p2}, U_{p3}) obtained for individual measuring members, the modules of short circuit loop impedance Z_{si} are determined (where $i = 1, 2$, and stands for the number of the metering branch).

$$\begin{cases} Z_{s1} = Z_{p1} \cdot \frac{E_1 - U_{p1}}{U_{p1}} \\ Z_{s2} = Z_{p2} \cdot \frac{E_2 - U_{p2}}{U_{p2}} \\ Z_{s3} = Z_{p3} \cdot \frac{E_3 - U_{p3}}{U_{p3}} \end{cases} \quad (2.4)$$

The relationship of the value of the module of short circuit loop impedance (Z_{si}) as a function of the measuring impedance angle (ψ_{pi}) is approximated by a second-degree polynomial:

$$Z_{si}(\psi_{pi}) = a \cdot \psi_{pi}^2 + b \cdot \psi_{pi} + c \quad (2.5)$$

Polynomial's coefficients (a , b , c) are determined based on phase angles values (ψ_{pi}) of metering impedances and calculated short circuit loop impedances (Z_{si}) for three measurement points, solving the following system of equations:

$$\begin{cases} a \cdot \psi_{p1}^2 + b \cdot \psi_{p1} + c = Z_{s1} \\ a \cdot \psi_{p2}^2 + b \cdot \psi_{p2} + c = Z_{s2} \\ a \cdot \psi_{p3}^2 + b \cdot \psi_{p3} + c = Z_{s3} \end{cases} \quad (2.6)$$

By using the Cramer method to solve the system of equations (6), determinants of the matrix of system coefficients are obtained, and then the values of the polynomial's coefficients are determined.

The searched, the actual value of the short circuit loop impedance module (Z_s) of the investigated circuit is the maximum of function $Z_{si}(\psi_{pi})$:

$$Z_s = \max\{Z_{si}(\psi_{pi})\} \quad (2.7)$$

The argument (ψ_r) at which the maximum of function $Z_{si}(\psi_{pi})$ occurs is also the actual angle of short circuit loop impedance:

$$\psi_r = \frac{-b}{2a} \quad (2.8)$$

The authentic value of the short circuit loop impedance module (Z_s) is determined based on the relationship:

$$Z_s = a \cdot \psi_r + b \cdot \psi_r + c \quad (2.9)$$

Thus, the real complex value of short circuit loop impedance (Z_s) for the investigated low voltage circuit is:

$$\underline{Z}_s = Z_s \cdot e^{j\psi_r} = Z_s (\cos \psi_r + j \sin \psi_r) \quad (2.10)$$

A system for measuring the complex value of short circuit loop impedance, in which the measuring terminals are connected to the input terminals, consisting of load impedance and a breaker, controlled by the central unit (built from the control, measuring and counting part). The factor of the measurement result, according to the invention, is characterized in that three input load elements are connected to the input terminals, in which the thyristor controlled switch is connected in series with the impedance. The input terminals are also connected in parallel to the main input of the central control-measuring-counting unit, whose control outputs are coupled with controlled switches and the measurement result display, which is also connected in parallel to the input terminals. The block diagram of the meter implementing the proposed method of metering the complex value of short circuit loop impedance is shown in Figure 2.5.

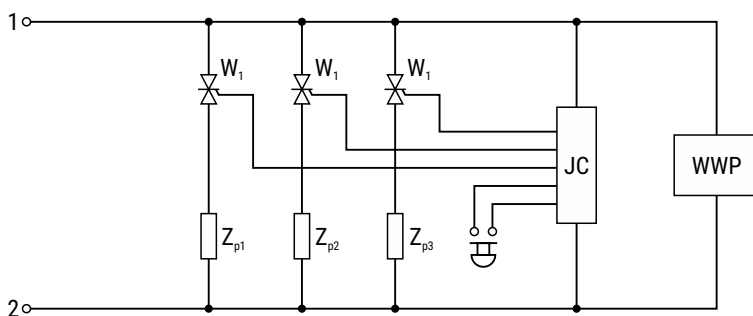


FIGURE 2.5. Block diagram of the meter implementing the proposed method of measuring the complex value of short circuit loop impedance [4]

Conclusions

Measuring short circuit loop impedance is necessary to determine the effectiveness of the protection against an electric shock by the self-acting power-off. There are two basic methods for determining it, i.e. the technical method (rarely seen today), and the voltage drop method (with direct or indirect measurement). The method proposed by the authors also belongs to the group of direct methods. The advantage of this method primarily involves the elimination of the influence of system operating loads on measurement accuracy. The simplicity of measurements is also important, as well as the fact that the complex value of short circuit loop impedance is determined based on measurements of RMS values of currents and voltages. Also, it is not required to maintain the same value of the modules of metering impedances.

Authors: G. Hołdyński, (g.holdynski@pb.edu.pl), Z. Skibko, (z.skibko@pb.edu.pl), Białystok University of Technology, Faculty of Electrical Engineering, Department of Electrical Power Engineering, Photonics and Lighting Technology, Wiejska 45D Str., 15-351 Białystok, Poland.

References

- [1] PN-HD 60364-4-41:2017 Low-voltage electrical installations. Protection for safety. Protection against electric shock.
- [2] PN-HD 60364-6:2016 Low-voltage electrical installations. Part 6: Verification.
- [3] Jankiewicz Z., “Verification of safety measures.” BEZEL website about electrical safety, bezel.com.pl (DOA: August 1, 2018).
- [4] Hołdyński G., Skibko Z., “The method and system for metering the short circuit loop impedance.” Patent granted by the Patent Office of the Republic of Poland no. PL 233 169 B1, 30/09/2019.

Chapter 3

Light pollution from small sports facilities

Magdalena Sielachowska, Maciej Zajkowski

*Bialystok University of Technology, Department of Photonics and Light Engineering,
Faculty of Electrical Engineering*

The article assesses the degree of night sky pollution with artificial light emitted by existing sports facilities. The paper shows the standard requirements that have to be met by properly designed lighting systems for sports and analyzes the effect of the reflection coefficients of the luminous flux on light pollution. The existing sports complex in Bialystok was analyzed.

Index terms: outdoor lighting, light pollution, luminous flux, sports facilities

Introduction

The concept of light pollution appeared for the first time in 1985, when Dutch ecologist F. J. Verheijen described the negative impact of artificial light on nature as photopollution, while separating the issue into two groups: the pollution of biological-ecological and astronomical nature [1]. The term, describing pollution by artificial light of the night sky and significantly limiting or completely preventing the observations of constellations, astronomers then described as light pollution.

The problem of light pollution is mainly related to population density. Urbanized areas are equipped with a much larger number of lighting solutions, such as street lighting, roads, parking lots, advertising billboards, architecture illuminations and greenery areas, in relation to rural or urban-rural areas. Artificial light pollution of the night sky is also strongly influenced by sports facilities such as football fields, tennis courts and athletics stadiums. The lighting criteria related to games and match broadcasts are high, while the requirements set for sports facilities, due to the need to limit the emission of luminous flux in the upper half-space, are very often treated as loose tips and are not subject to any control or verification.

Normative requirements for sports facilities

Designing lighting systems, in the case of sports facilities, is not the easiest task because it requires taking into account both the comfort and safety of players, viewers, as well as adapting the installation to the requirements of television broadcasts. All available guidelines and standards take into account the type and rank of games that are carried out in a given sports complex, and also need to consider the type of television broadcasts performed within their area.

Currently, the most important documents defining the criteria to be met by properly designed lighting systems in sports facilities are:

- Report IES RP-6-15 Sports and Recreational Area Lighting [2],
- Polish Standard PN-EN 12193: 2008 Light and lighting – Lighting in sport [3],
- Sports federation documents relating to the sport discipline represented by the organization, e.g. Report FIFA Football Stadiums Technical Recommendations and Requirements [4]

In each of these documents, a division into lighting classes was made, depending on the type of gameplay, audience size or type of transmission, different normative requirements were presented for each class.

The IES Report RP-6-15 [2] categorizes four lighting classes:

- Class I – Facilities with audiences above 5000
- Class II – Facilities with audiences below 5000
- Class III – Facilities with audiences below 2000
- Class IV – Facilities with limited or no audience (recreational game only).

The required minimum average illuminance value for the lowest class IV is 200 lx, in the case of the highest class I, this value increases to 1000 lx (Table 3.1). For sports facilities of a training and recreational nature, average illuminance values on the horizontal plane constitute the basic reference parameter. In the case of facilities with television broadcasting, it is necessary to take into account an additional parameter, which is the illumination on the vertical plane.

TABLE 3.1. Recommended illuminance level for football fields [2]

Class	Horizontal illuminance [lx]	E_{\max} / E_{\min}
Class I	1000	1.7:1 or less
Class II	500	2.0:1 or less
Class III	300	2.5:1 or less
Class IV	200	3:1 or less

In addition to regulations regarding the selection of lighting, required levels of lighting, luminance and uniformity, the document also deals with the topic of light pollution. The specification stipulates the need to minimize the distribution of light outside the area of sports facilities, which may obstruct the observation of stars and disrupt the functioning of living organisms in the area.

Another document to consider when designing a lighting system in a sports facility is the Polish Standard PN-EN 12193: 2008 Light and lighting – Lighting in sport [3]. It defines the requirements for lighting intensity, uniformity, luminance and methods for measuring these quantities, indoors and outdoors, during the most popular European sports.

The requirements indicated in the standard [3] specify the maximum permissible value of disturbing light coming from external lighting installations divided into four environmental zones, from a completely dark zone E1, through zone E2 with low brightness, zone E3 with medium brightness, up to zone E4, characterized by high brightness.

For each zone, the standard [3] determines the percentage of luminaire luminous flux that is radiated above the horizon, i.e. the so-called ULR. It is defined as the percentage share of the luminous flux emitted by a lighting fixture or lighting system in the upper half-space, in relation to the installed flux [5]. The values of the maximum allowable interfering light from external lighting installations are summarized in Table 3.2.

TABLE 3.2. Maximum obtrusive light permitted for exterior lighting installations [3]

Environmental zone	Light on properties		Luminaire intensity		Upward light
	E_v [lx]		I [cd]		ULR [%]
	Pre-curfew *	Post-curfew	Pre-curfew	Post-curfew	
E1	2	0	2500	0	0
E2	5	1	7500	500	5
E3	10	2	10000	1000	15
E4	25	5	25000	2500	25

* If no curfew regulations are available, the higher values shall not be exceeded and the lower values should be taken as preferable limits

One of the most restrictive guidelines related to the design of lighting installations in sports facilities is the one presented in the FIFA Football Stadiums Technical Recommendations and Requirements report [4]. The regulations are presented for five lighting classes (Class I – training and recreation without television broadcasts, Class II – leagues and clubs without television broadcasts, Class III – national games without television broadcasts), including two that require special lighting in connection with television broadcasts (Class IV – national games with television broadcast, Class V – international games with television broadcast).

Specifications for events transmitted in the media are presented in Table 3.3. Reference values, in the case of the FIFA report [4], are primarily the values of vertical and horizontal illuminance. For the fourth and fifth class, the average vertical illumination fluctuates between 1400 and 2400 lux, while the values of average horizontal illumination can reach values even above 3500 lux. All the values indicated in the document are so-called preserved values, which means that when designing the lighting system, the maintenance factor for a given sports facility should also be taken into account. As a result, the required average illuminance values can be up to one and a half times higher than the values given in Table 3.3.

The assumptions that were included in the report IES RP-6-15, Polish Standard PN-EN 12193: 2008 [3] and in the report of the FIFA federation are intended to guarantee the comfort and safety of practicing a given sports discipline, meet the dimensions of the facility and ensure the comfort of watching the game and its coverage. Designers and investors should also not forget about the existence of one more problem related to excessive emission of the luminous flux in the upper half-space, i.e. light pollution. Limiting the distribution of artificial light outside the area of a given sports facility is necessary to maintain the comfort of life of people living in the vicinity of stadiums and reduce the consumption of eclectic energy for the lighting of sports complexes.

TABLE 3.3. Lighting specifications for televised events [4]

		Vertical illuminance			Horizontal illuminance		
		E_v	U		E_v	U	
Class	Calculation towards	Lux	U1	U2	Lux	U1	U2
Class V	Fixed camera	2 400	0.5	0.7	3 500	0.6	0.8
	Field camera (at pitch level)	1 800	0.4	0.65			
Class IV	Fixed camera	2 000	0.5	0.65	2 500	0.6	0.8
	Field camera (at pitch level)	1 400	0.35	0.6			

* All indicated illuminance values are maintained values. A maintenance factor of 0.7 is recommended; therefore, initial values will be approximately 1.4 times as those indicated above

Some documents and regulations highlight the negative impact of artificial light, emitted by existing objects and external lighting, on living organisms and introduce guidelines forcing control and reduction of the amount of artificial light emitted in the upper half-space (Table 3.4).

TABLE 3.4. Enviromental factor [4]

Angle of illumination	Distance from stadium perimeter	
Horizontal spill	50 m from stadium perimeter	25 lx
Horizontal spill	200 m further	10 lx
Maximum vertical	50 m from stadium perimeter	40 lx
Maximum vertical	200 m from stadium perimeter	20 lx

Luminous flux transmission

In the literature, the concept of “luminous flux” is defined as a photometric quantity derived from the energy flux (radial power), based on the assessment of radiation using a receiver with relative spectral sensitivity corresponding to the spectral sensitivity of the human eye adapted to photopic conditions (brightness) and described by formula (1) [6], [7]:

$$\Phi = K_m \int_{380}^{780} \Phi_{e,\lambda} V_\lambda [lm], \quad (3.1)$$

where:

$K_m = 683$ [lm/W) – photometric radiation equivalent,

$\Phi_{e,\lambda}$ – spectral distribution of radial power (energy stream),

V_λ – relative luminous efficiency of monochrome radiation.

The luminous flux falling on a given surface, depending on its type, may be reflected, transmitted or absorbed. Usually, two of the above phenomena occur simultaneously, i.e. reflection and absorption, due to the fact that there are neither perfectly reflecting nor perfectly absorbing bodies in nature [7], [8].

Transmission and absorption phenomena are not included in this article. In order to describe the degree of light pollution from existing sports facilities, the Lambertian reflection phenomenon of the object’s surfaces was used. A relationship was used that determines the luminance value of a given surface (2), depending on its reflection coefficient and level of illuminance [10]:

$$L = \frac{\rho}{\pi} \cdot E [cd/m^2], \quad (3.2)$$

where:

ρ – reflection coefficient,

$\pi = 3.14$ – mathematical constant,

E – illuminance on the plane.

In order to determine the balance of luminous flux emanating outside the area of the analyzed sports complex and to analyze the excessive distribution of artificial light, it was assumed that a given sports facility constitutes a kind of lighting fixture (Figure 3.1).

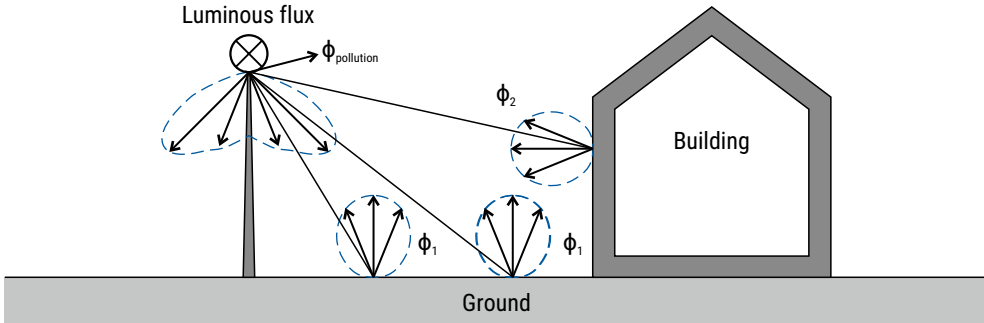


FIGURE 3.1. Luminous flux balance

It is worth noting that the luminous flux can be emitted in the upper half-space in two ways: directly or by reflection from various types of surfaces. The part of the light emitted directly towards the sky can be described by the so-called ULOR (Upward Light Output Ratio), formula (3.3) [11].

$$ULOR = \frac{\Phi_{up}}{\Phi_c} \cdot 100\%, \quad (3.3)$$

where:

- Φ_{up} – luminous flux emitted in the upper half-space,
- Φ_c – luminous flux of the light source in the luminaire.

The luminous flux balance can be described by formula (3.4).

$$\Phi = \Phi_1 + \Phi_2 + \Phi_{pollution} \text{ [lm]}, \quad (3.4)$$

where:

- Φ_1 – luminous flux reflected from the ground,
- Φ_2 – luminous flux reflected from existing objects,
- $\Phi_{pollution}$ – luminous flux directed directly towards the upper half-space.

It should be noted that the light reflected from the ground and nearby objects is directed upwards, and then bounces off the cloud layer and returns to the ground. This not only causes excessive illumination of the night sky, but also an increase in illumination on the earth's surface. It is not possible to completely eliminate the luminous flux emitted in the upper half-space, but it is possible to use the luminous flux returning to the ground, among others, to improve the energy efficiency of road lighting, which will be presented later in the article.

Light pollution for selected sports complexes

The assessment of light pollution, based on the analysis of light beam distribution, was made on the example of existing sports complexes located in Bialystok (53° 07' N 23° 09' E). Two facilities were examined: the large-size Municipal Stadium and the Sports School, located in a small urban housing estate.

In the article “Estimating light pollution from sports facilities using DIALux simulation software” [12], the authors determined the amount of luminous flux emitted outside the studied sports facility – the Municipal Stadium in Bialystok, at different cloud heights, taking into account the actual light reflection coefficients. The obtained results showed that about 20% of the luminous flux comes out of the football field and increases the effect of sky pollution [12].

For the same facility, an analysis of light distribution in the upper half-space was also carried out, depending on the value of the stadium’s surface reflection coefficients. During simulations, the values of light reflection coefficients on the stands surface (0.1 ÷ 0.9) and the main board of the object (0.1 ÷ 0.4), i.e. a football field, were modified [7]. The characteristics of the change in the value of lighting intensity together with the increase in the reflection coefficient of the stands and the differences between the lowest and the highest value for individual cases are presented in Figure 3.2.

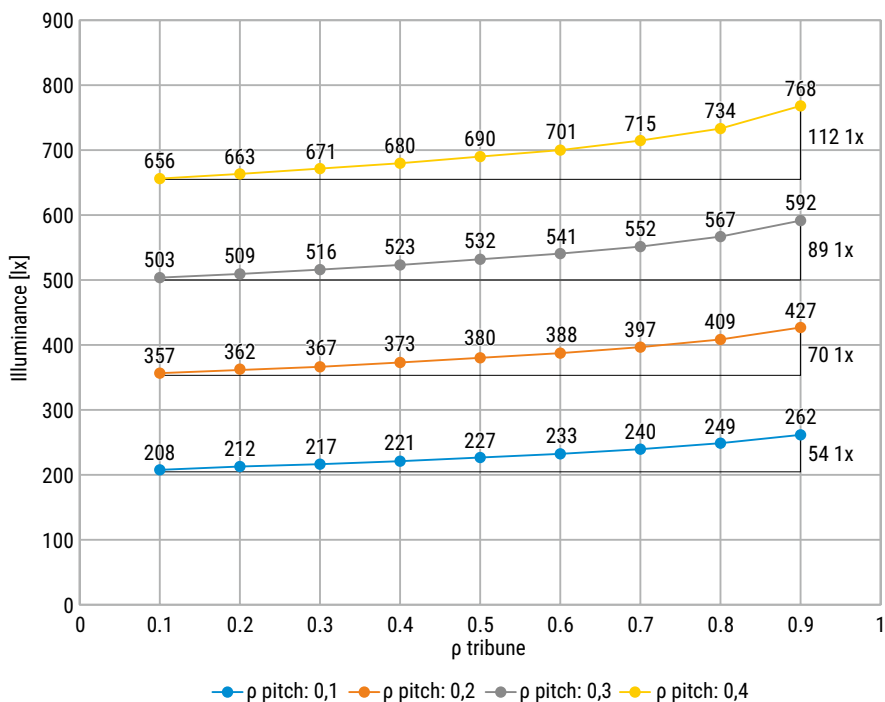


FIGURE 3.2. Graph of change in average illuminance as a function of tribune reflection coefficient [7]

The average illuminance values obtained by means of computer simulations oscillated between 208 and even 768 lux, which indicates a significant emission of the luminous flux from the stadium in the upper half-space.

Table 3.5 summarizes the calculated percentage values of the luminous flux escaping into the upper half-space. The amount of light that can be emitted by any football stadium, category IV (national games with television broadcasts) can reach [7]:

- from 3% for $\rho_{pitch} = 0.1$ and $\rho_{tribune} = 0.1$
- from 23% for $\rho_{pitch} = 0.4$ and $\rho_{tribune} = 0.9$.

TABLE 3.5. Average lighting distribution on adjoining streets surrounding the sports school in Bialystok

Gdańska Street	Lwowska Street	Lwowska Street	Pod Krzywą Street
Illuminance [lx]			
1.50 – 1.96	0.78 – 1.22	0.02 – 0.28	1.93 – 2.43
Luminance [cd/m ²]			
0.18 – 0.23	0.09 – 0.14	0.002 – 0.03	0.23 – 0.28

This article analyzes the next sports complex at the Sports School in Bialystok (Figure 3.3). The school has a football field, two basketball fields and a tennis court. The fields are illuminated with 20 LED luminaires, each with a power of 450 W.

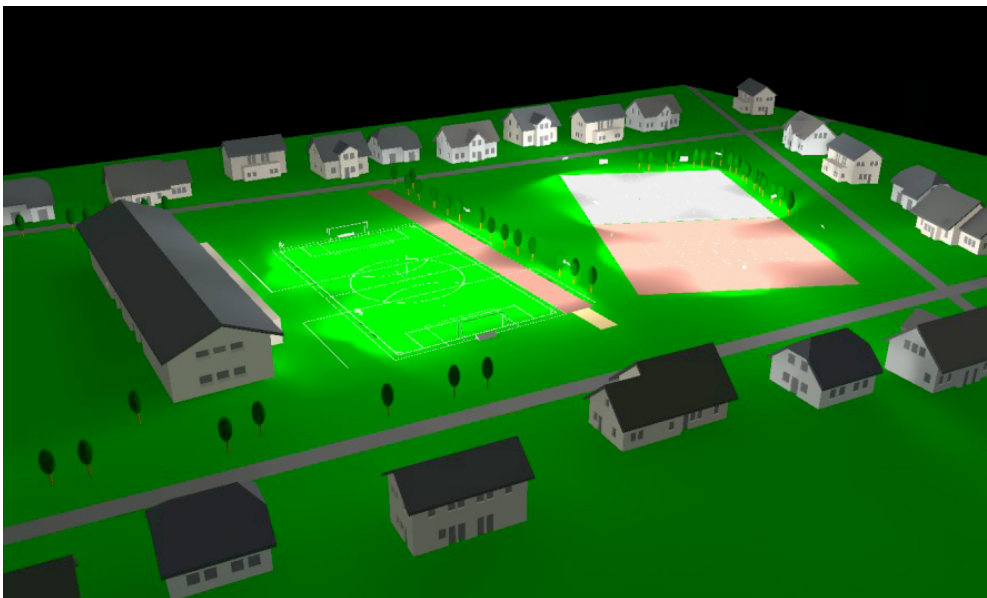


FIGURE 3.3. Sports School in Bialystok – view in the DIALux program

The school is surrounded by four streets (Figure 3.4), for which the possibility of reducing electricity consumption for the lighting of roads was analyzed, using the phenomenon of light pollution. Pod Krzywą Street is the best lit up, here the values oscillate between 1.93 and 2.43 lux, similarly in the case of Gdańska Street, from 1.5 to almost 2 lux. By comparing the results obtained with the required values, given in the lighting standard [3], it can be calculated to what extent it is possible to reduce energy consumption for the lighting of roads and streets located in the vicinity of a given sports facility (Figure 3.5).

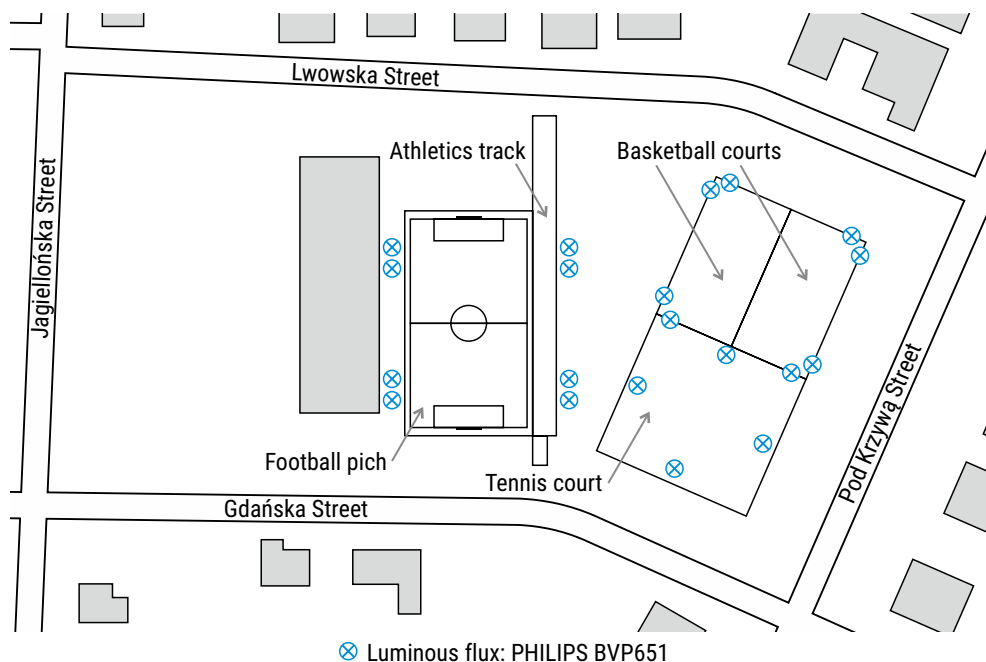


FIGURE 3.4. Sports School in Białystok – top view

The average distribution of illuminance on adjacent streets is shown in Table 3.5. In the case of the Sports School, it is possible to reduce energy consumption for the lighting of Pod Krzywą Street by about 24% while the lighting installation of the fields is switched on. For Gdańska Street, this is a saving of 20%, for Lwowska Street about 13% and less than 5% for Jagiellońska Street.

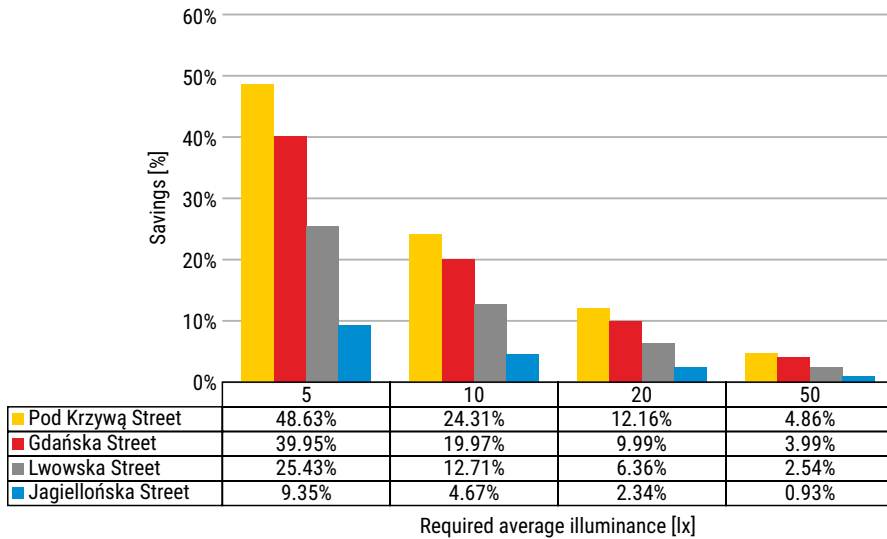


FIGURE 3.5. Improving the energy efficiency of road lighting around the Sports School in Białystok

The following charts (Fig. 3.6 and 3.7) show the possibility of limiting the power of road lighting luminaires at night for the analyzed objects.

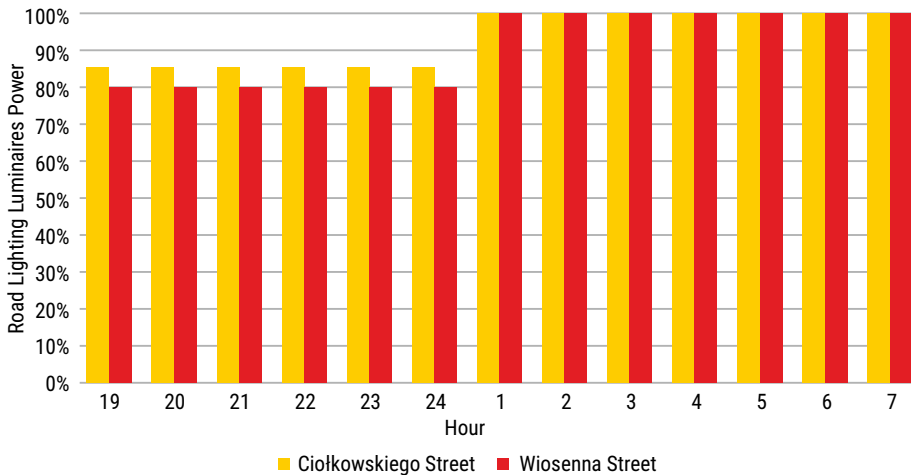


FIGURE 3.6. Reduction of energy consumption for road lighting in the vicinity of the Municipal Stadium in Białystok

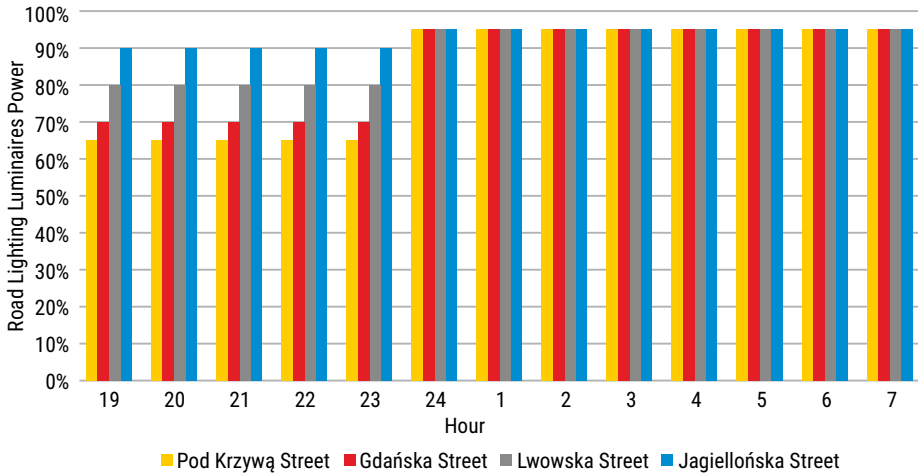


FIGURE 3.7. Reduction of energy consumption for road lighting in the vicinity of the Sports School in Białystok

In the case of the Municipal Stadium, it is possible to limit the luminous flux of luminaires to 80 – 85% between 19:00 and 24:00.

For the Sports School, this means reducing energy consumption by up to 35% for Pod Krzywą Street between 19:00 and 23:00 and reducing the power of road lighting fittings throughout the night by 5%, due to the luminance of the sky itself.

Conclusion

Sports facilities, regardless of their size, significantly contribute to increasing the effect of pollution of the night sky with artificial light. The simulation analysis shows that it is possible to emit a light beam in the upper half-space even at a level of 50% from existing sports complexes. Such high values above all prove the ineffective lighting of sports facilities. It is possible to reduce light pollution by reducing the reflection coefficients of stadium structures, or in the case of closed facilities, by modifying their structure. However, none of these solutions will eliminate the problem of light pollution in full. Therefore, the authors of the article suggest the use of luminous flux emitted in the upper half-space, and then returning to the ground to improve the energy efficiency of road lighting. It is possible to partially reduce the energy consumption needed to illuminate the roads located in the vicinity of sports facilities when the lighting of the fields is on.

The article was realized in the Department of Photonics and Light Engineering at the Faculty of Electrical Engineering, Białystok University of Technology as part of the statutory work S/WE/3/2018 and as part of the work WI/WE-IA/10/2020 funded by the Ministry of Science and Higher Education.

Authors: mgr inż. Magdalena Sielachowska (e-mail: m.sielachowska@doktoranci.pb.edu.pl), dr hab. inż. Maciej Zajkowski, prof. nzw. w PB (e-mail: m.zajkowski@pb.edu.pl), Białystok University of Technology, Faculty of Electrical Engineering, Department of Photonics and Light Engineering, Wiejska 45D Str., 15-351 Białystok, Poland.

References

- [1] Verheijen, F. J., “Photopollution: artificial light optic spatial control systems fail to cope with. Incidents, causation, remedies,” *Exp. Biol.* (1985), 44(1), 1–18W.-K. Chen, *Linear Networks and Systems*. Belmont, CA, USA: Wadsworth, 1993, pp. 123–135.
- [2] Illuminating Engineering Society: IES RP-6-15 Sports and Recreational Area Lighting (2015).
- [3] PN-EN 12193:2008 Światło i oświetlenie – Oświetlenie w sporcie.
- [4] FIFA: Football Stadiums Technical Recommendations and Requirements, Fédération Internationale de Football Association, Zurich (2007).
- [5] Sielachowska M., Tyniecki D., Zajkowski M., “The Concept of Measuring Luminous Flux Distribution Emitted from Sports Facilities Using Unmanned Aerial Vehicles, Methods and Techniques of Signal Processing in Physical Measurements,” Springer. 548 (2019), pp. 306–318.
- [6] Żagan W., “Podstawy Techniki Świetlnej,” Oficyna Wydawnicza Politechniki Warszawskiej, Warszawa (2014).
- [7] Sielachowska M., Zajkowski M., “Assessment of Light Pollution Based on the Analysis of Luminous Flux Distribution in Sports Facilities,” *Engineer of the XXI Century*, Springer, 70 (2019), pp. 139–150.
- [8] Musiał E., “Podstawowe pojęcia techniki oświetleniowej,” *Biuletyn SEP INPE Informacje o normach i przepisach elektrycznych*, No. 75, Warszawa (2005), pp. 3–38.
- [9] Tabaka P., “Klasyfikacja odbicia światła od materiałów stosowanych na odbłyśniki” [Online]. Accessed: http://www.przemyslawtabaka.info/materialy/czynniki_osw/publikacja1.pdf.
- [10] Wandachowicz K., “Wyznaczanie rozkładu luminancji we wnętrzach z uwzględnieniem kierunkowo-rozproszonych charakterystyk odbiciowych materiałów,” Poznań: Politechnika Poznańska (2000).
- [11] Estrada-Garcia R. and others, “Statistical modelling and satellite monitoring of upward light from public lighting,” *Lighting Research Technology*, 48 (2016), pp. 810–822.
- [12] Sielachowska M., Zajkowski M., “Szacowanie zanieczyszczenia światłem od obiektów sportowych za pomocą oprogramowania symulacyjnego DIALux,” *Poznan University of Technology Academic Journals. Electrical Engineering*, No. 96, Poznan (2018), pp. 219–229.

Chapter 4

Decomposition of the load's current supplied from a sinusoidal and asymmetrical voltage source in accordance with the Currents' Physical Components (CPC) Theory

Zbigniew Sołjan, Michał Dziemiańczyk
Białystok University of Technology, Faculty of Electrical Engineering

The correct description of circuits supplied from an asymmetrical and sinusoidal voltage source in which the load can be asymmetric or unbalanced necessitates a well-defined approach. The present development of electrical engineering allows for describing three-phase three-wire systems with asymmetric sinusoidal or non-sinusoidal supply. In addition, it is possible in that kind of systems to balance the load and compensate for reactive power.

The subject of this article is to exhibit the possibility of describing three-phase circuits powered from an asymmetric sinusoidal voltage source. Determining the physical components of the current associated closely with specific physical phenomena makes it possible to distinguish the components of unbalanced active and reactive components. Each of these currents, excluding the active current, contributes to the power of unbalanced and reactive power, which should be minimized or completely removed from the circuit.

Index terms: Current's Physical Components (CPC), power definitions, power theory, asymmetric voltage source

Introduction

Transmission of electricity from sources to loads through power systems, where it is transformed adequately to the needs of the consumer, is described by power theories [1, 2, 3, 4, 5, 6, 7, 17]. Over 100 years of energy transmission, many different approaches have been created.

The description of power theory is divided into two domains, i.e. time and frequency. The characterization within the time domain, in view of the speed of calculation, is primarily used to control semiconductor devices in active or hybrid power filters [4, 5, 11, 12, 13, 14, 15, 16, 17, 18]. The most common time domain methods are [4, 5, 6, 17]. The description in the frequency domain [1, 3, 25], using Fourier transform, causes delays in the measuring length; however, the methods based on frequency description are more precise and are also used to generate the reference current of the active power filter [8, 9, 10]. In power theories quoted above, the mathematical description and, as a result, the obtained results are correct, on the assumption that the voltage source is symmetry.

In publications [19, 20, 21] a description of asymmetrical sinusoidal three-phase three-wire power circuits is presented. In addition, in these articles, the possibility of building an unbalanced and reactive power compensator has been demonstrated.

This publication proposes an expansion of the Currents' Physical Components (CPC) Theory for asymmetrical sinusoidal three-phase four-wire power systems, i.e. circuits with a neutral conductor (N) and/or a protective earth conductor (PE).

Currents' physical components in three-phase four-wire systems at sinusoidal and asymmetric voltage supply

The source voltage of the distribution system can be referred to as a three-phase vector, where its elements are the voltages at terminals R, S, T, namely $\mathbf{e} = [e_R \ e_S \ e_T]$. This voltage as asymmetrical can have symmetrical components of the positive sequence $-\mathbf{e}^p$, negative sequence $-\mathbf{e}^n$ and zero sequence $-\mathbf{e}^z$. It should also be mentioned that in the event of asymmetrical power supply, the internal impedance of the power source should be considered; therefore, the ideal source should not be used – which is a departure from pure theory. In connection with the above, the line voltage is defined by vector $\mathbf{u} = [u_R \ u_S \ u_T]^T$ that has three components, i.e.: $\mathbf{u} = \mathbf{u}^p + \mathbf{u}^n + \mathbf{u}^z$ [24].

An unbalanced linear time-invariant (LTI) load supplied by a sinusoidal but asymmetric voltage source is shown in Figure 4.1.

Symbols \mathbf{u} and \mathbf{i} denote voltage and current vectors:

$$\begin{aligned}\mathbf{u}(t) &= [u_R(t) \ u_S(t) \ u_T(t)]^T, \\ \mathbf{i}(t) &= [i_R(t) \ i_S(t) \ i_T(t)]^T.\end{aligned}\tag{4.1}$$

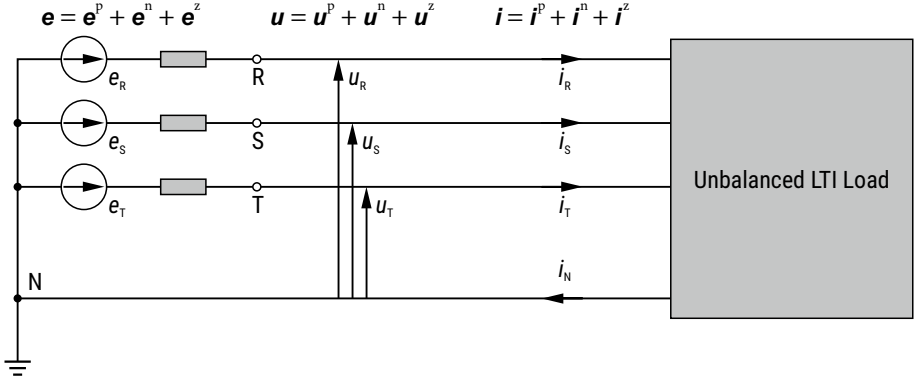


FIGURE 4.1. LTI load supplied by a four-wire line

The sinusoidal voltage supplied linear time-invariant (LTI) unbalanced load can be presented in the form of:

$$\mathbf{u}(t) = \begin{bmatrix} u_R(t) \\ u_S(t) \\ u_T(t) \end{bmatrix} = \sqrt{2} \operatorname{Re} \begin{bmatrix} U_R \\ U_S \\ U_T \end{bmatrix} e^{j\omega t} = \sqrt{2} \operatorname{Re} \{ \mathbf{U} e^{j\omega t} \} \quad (4.2)$$

The line current can be depicted identically, namely:

$$\mathbf{i}(t) = \begin{bmatrix} i_R(t) \\ i_S(t) \\ i_T(t) \end{bmatrix} = \sqrt{2} \operatorname{Re} \begin{bmatrix} I_R \\ I_S \\ I_T \end{bmatrix} e^{j\omega t} = \sqrt{2} \operatorname{Re} \{ \mathbf{I} e^{j\omega t} \} \quad (4.3)$$

The supply voltage \mathbf{u} could be asymmetrical – Figure 4.1; therefore, it is possible to present it as the sum of the voltages of the positive, negative and zero sequences:

$$\mathbf{u} = \mathbf{u}^p + \mathbf{u}^n + \mathbf{u}^z = \sqrt{2} \operatorname{Re} \{ (\mathbf{U}^p + \mathbf{U}^n + \mathbf{U}^z) e^{j\omega t} \} = \sqrt{2} \operatorname{Re} \{ (\mathbf{1}^p \mathbf{U}^p + \mathbf{1}^n \mathbf{U}^n + \mathbf{1}^z \mathbf{U}^z) e^{j\omega t} \}, \quad (4.4)$$

where U^p, U^n and U^z are the complex rms (crms) values of the symmetrical components of the positive, negative and zero sequences, described by the Fortesque Transformation [7, 21]:

$$\begin{bmatrix} U^p \\ U^n \\ U^z \end{bmatrix} = \frac{1}{3} \begin{bmatrix} 1 & \alpha & \alpha^* \\ 1 & \alpha^* & \alpha \\ 1 & 1 & 1 \end{bmatrix} \begin{bmatrix} U_R \\ U_S \\ U_T \end{bmatrix}, \quad (4.5)$$

where $\alpha = 1e^{j120^\circ}$, $\alpha^* = 1e^{-j120^\circ}$, and symbols

$$\mathbf{1}^p = \begin{bmatrix} 1 \\ \alpha^* \\ \alpha \end{bmatrix} = \begin{bmatrix} 1 \\ 1e^{-j120^\circ} \\ 1e^{j120^\circ} \end{bmatrix}, \quad \mathbf{1}^n = \begin{bmatrix} 1 \\ \alpha \\ \alpha^* \end{bmatrix} = \begin{bmatrix} 1 \\ 1e^{j120^\circ} \\ 1e^{-j120^\circ} \end{bmatrix}, \quad \mathbf{1}^z = \begin{bmatrix} 1 \\ 1 \\ 1 \end{bmatrix} \quad (4.6)$$

denote unit symmetrical three-phase coefficients of the positive – $\mathbf{1}^p$, negative – $\mathbf{1}^n$, and zero sequences – $\mathbf{1}^z$, shown in Figure 4.2.

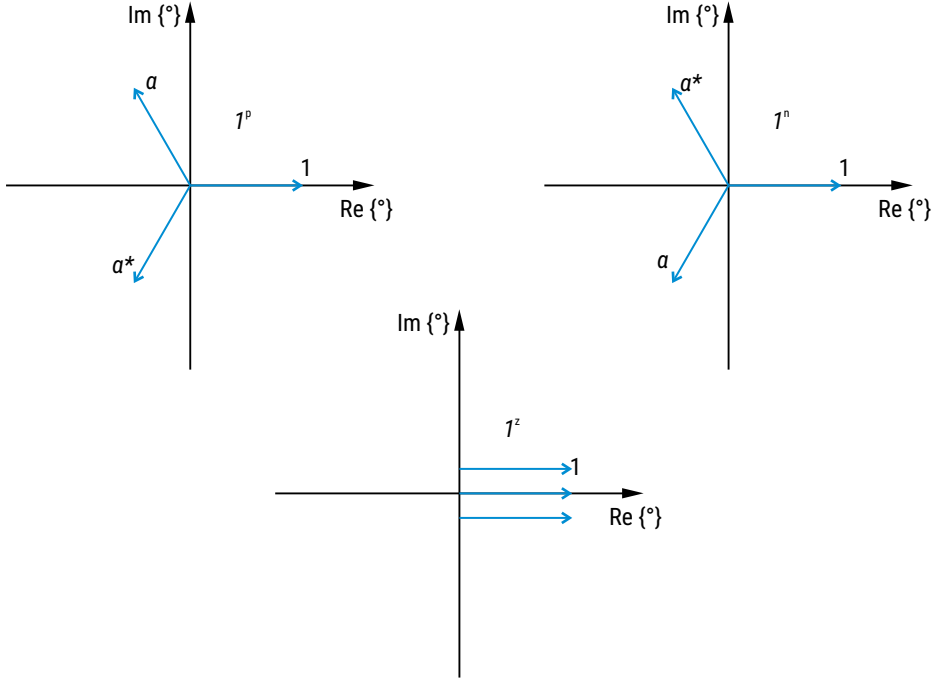


FIGURE 4.2. Unit symmetrical vectors

In publications [19, 20, 21], the difference between the apparent power module, apparent power and complex power, which is marked as \mathbf{C} , will be used later in the article.

For a linear balanced and time-invariant load supplied by the four-wire system is considered the load powered by sinusoidal symmetric voltage, despite the current asymmetry. For each unbalanced load, it is possible to find a balanced load, equivalent to it for active power P and reactive power Q . In order for it to be equivalent to the original circuit due to active power P and reactive power Q , its phase admittance takes the value of:

$$\mathbf{Y}_b = G_b + jB_b = \frac{P - jQ}{\|\mathbf{u}\|^2} = \frac{\mathbf{C}^*}{\|\mathbf{u}\|^2}, \quad (4.7)$$

where $\|\mathbf{u}\|$ denotes three-phase rms value of the voltage supply, equal to:

$$\|\mathbf{u}\| = \sqrt{\frac{1}{T} \int_0^T \mathbf{u}^T(t) \mathbf{u}(t) dt} = \sqrt{U_R^2 + U_S^2 + U_T^2}, \quad (4.8)$$

and the Y_b admittance defined by (7) will be described as the **equivalent admittance of the balanced load**, which is presented in Figure 4.3.

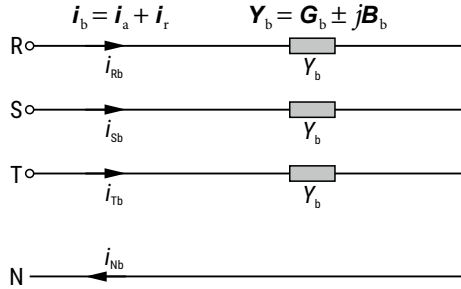


FIGURE 4.3. Balanced load, equivalent to the original load due to active and reactive power

The balanced load, shown in Figure 4.3, loads the supply source by the balanced current i_b , which has an active component:

$$i_a = G_b \mathbf{u} = \sqrt{2} \operatorname{Re} \left\{ G_b (\mathbf{U}^p + \mathbf{U}^n + \mathbf{U}^z) e^{j\omega t} \right\} = \sqrt{2} \operatorname{Re} \left\{ G_b (\mathbf{1}^p U^p + \mathbf{1}^n U^n + \mathbf{1}^z U^z) e^{j\omega t} \right\} \quad (4.9)$$

and a reactive component:

$$\begin{aligned} i_r &= B_b \mathbf{u} (t + T/4) = \sqrt{2} \operatorname{Re} \left\{ jB_b (\mathbf{U}^p + \mathbf{U}^n + \mathbf{U}^z) e^{j\omega t} \right\} = \\ &= \sqrt{2} \operatorname{Re} \left\{ jB_b (\mathbf{1}^p U^p + \mathbf{1}^n U^n + \mathbf{1}^z U^z) e^{j\omega t} \right\} \end{aligned} \quad (4.10)$$

Three-phase rms value of the active current i_a and reactive current i_r are respectively:

$$\|i_a\| = G_b \|\mathbf{u}\| = \frac{P}{\|\mathbf{u}\|}, \quad (4.11)$$

$$\|i_r\| = |B_b| \|\mathbf{u}\| = \frac{|Q|}{\|\mathbf{u}\|}. \quad (4.12)$$

With respect to the fact that these currents are proportional to the voltage and supply voltage shifted in time by a quarter period, they, therefore, have exactly the same degree of asymmetry as the supply voltage. However, the current of the original load i , as a consequence of its being unbalanced, does not have the same asymmetry as the supply voltage \mathbf{u} . The current of the imbalanced load may, therefore, have an unbalanced component:

$$i - (i_a + i_r) = i - i_b = i_u, \quad (4.13)$$

where its waveform is as follows:

$$\mathbf{i}_u = \sqrt{2} \operatorname{Re} \{ \mathbf{I}_u e^{j\omega t} \} = \sqrt{2} \operatorname{Re} \{ (\mathbf{I} - \mathbf{I}_b) e^{j\omega t} \} = \sqrt{2} \operatorname{Re} \{ (\mathbf{I} - \mathbf{Y}_b \mathbf{U}) e^{j\omega t} \}. \quad (4.14)$$

Upon rearrangement (13), the load current can be expressed as follows:

$$\mathbf{i} \sim \mathbf{i}_a + \mathbf{i}_r + \mathbf{i}_u, \quad (4.15)$$

which means that the current of the load is the sum of the active current, reactive current and unbalanced current. Each component is associated with a different physical phenomenon. The active current \mathbf{i}_a is related to the permanent flow of energy from the source to the load. The reactive current \mathbf{i}_r is related to the displacement of the load current in relation to the supply voltage. The unbalanced current \mathbf{i}_u is the result of the asymmetry of the currents caused by the unbalanced condition of the load. On the grounds of the unambiguous connection of these currents with separate physical phenomena in the circuit, they can be treated as Currents' Physical Components of the load current.

The three-phase rms value of the load's current supplied by the sinusoidal asymmetrical voltage source is equal to:

$$\|\mathbf{i}\|^2 = \|\mathbf{i}_a\|^2 + \|\mathbf{i}_r\|^2 + \|\mathbf{i}_u\|^2. \quad (4.16)$$

Equation (16) is true provided that the current components of the load are mutually orthogonal. Orthogonality is presented in Appendix A.

In order to demonstrate the possibility of building a balancing compensator of the negative and zero sequences and the reactive power compensator, the components of the unbalanced current should be decomposed.

Equivalent admittance of the balanced load (7) can be expressed by the parameters of the load and the supply voltage as follows:

$$\mathbf{Y}_b = G_b + jB_b = \frac{P - jQ}{\|\mathbf{u}\|^2} = \frac{\mathbf{Y}_R U_R^2 + \mathbf{Y}_S U_S^2 + \mathbf{Y}_T U_T^2}{\|\mathbf{u}\|^2}. \quad (4.17)$$

At the symmetry condition of the supply voltage, i.e.: $U_R = U_S = U_T = \|\mathbf{u}\|$, equivalent admittance of the balanced load assumes the form:

$$\mathbf{Y}_b = \frac{1}{3} (\mathbf{Y}_R + \mathbf{Y}_S + \mathbf{Y}_T) = \mathbf{Y}_e \quad (4.18)$$

and is called **the equivalent admittance of the load supplied by the symmetric voltage source**.

The difference between admittances expressed in (4.17) and (4.18) is:

$$\mathbf{Y}_d = G_d + jB_d = \mathbf{Y}_e - \mathbf{Y}_b = \frac{1}{3} (\mathbf{Y}_R + \mathbf{Y}_S + \mathbf{Y}_T) - \frac{\mathbf{Y}_R U_R^2 + \mathbf{Y}_S U_S^2 + \mathbf{Y}_T U_T^2}{\|\mathbf{u}\|^2} \quad (4.19)$$

and denotes **the voltage asymmetry dependent admittance**.

According to [22, 23] in four-wire systems supplied from a source of sinusoidal voltage, the two admittances respond to the imbalanced form of the load, i.e.: **the unbalanced admittance of the negative sequence**, described in the relationship:

$$A^n = \frac{1}{3}(Y_R + \alpha Y_S + \alpha^* Y_T) \quad (4.20)$$

and **the unbalanced admittance of the zero sequence**:

$$A^z = \frac{1}{3}(Y_R + \alpha^* Y_S + \alpha Y_T). \quad (4.21)$$

Based on (4.17), (4.18) and (4.19), the crms current value can be represented as follows:

$$\begin{aligned} I_R = Y_R U_R &= \frac{1}{3}(Y_R + Y_S + Y_T)U_R + \left(\frac{1}{3} \begin{bmatrix} 1 \\ \alpha \\ \alpha^* \end{bmatrix}^T \begin{bmatrix} Y_R \\ Y_S \\ Y_T \end{bmatrix} + \frac{1}{3} \begin{bmatrix} 1 \\ \alpha^* \\ \alpha \end{bmatrix}^T \begin{bmatrix} Y_R \\ Y_S \\ Y_T \end{bmatrix} \right) U_R = \\ &= Y_e U_R + (\mathbf{1}^{nT} Y_e + \mathbf{1}^{pT} Y_e) U_R \end{aligned} \quad (4.22)$$

and can be transformed using (4.20) and (4.21) into:

$$I_R = Y_e U_R + (A^n + A^z) U_R^p + (A^n + A^z) U_R^n + (A^n + A^z) U_R^z. \quad (4.23)$$

Then (23) is further transformed and, using the $Y_e = Y_b + Y_d$ condition, the current in the R-line can be expressed:

$$I_R = (Y_b + Y_d) U_R + (A^n + A^z) U_R^p + (A^n + A^z) U_R^n + (A^n + A^z) U_R^z. \quad (4.24)$$

The crms current values of the current in the S-line can be expressed in the same way, i.e.:

$$I_S = (Y_b + Y_d) U_S + (\alpha^* A^n + \alpha A^z) U_S^p + (\alpha^* A^n + \alpha A^z) U_S^n + (\alpha^* A^n + \alpha A^z) U_S^z \quad (4.25)$$

and the T-line current as:

$$I_T = (Y_b + Y_d) U_T + (\alpha A^n + \alpha^* A^z) U_T^p + (\alpha A^n + \alpha^* A^z) U_T^n + (\alpha A^n + \alpha^* A^z) U_T^z. \quad (4.26)$$

The relationship (4.28) can be further transformed and then the vector of crms values is as follows:

$$\begin{aligned} \mathbf{I}_u &= \mathbf{1}^p \mathbf{Y}_d \mathbf{U}^p + \mathbf{1}^n \mathbf{Y}_d \mathbf{U}^n + \mathbf{1}^z \mathbf{Y}_d \mathbf{U}^z + \mathbf{1}^p \left(\mathbf{A}^n \mathbf{U}^z + \mathbf{A}^z \mathbf{U}^n \right) + \\ &+ \mathbf{1}^n \left(\mathbf{A}^n \mathbf{U}^p + \mathbf{A}^z \mathbf{U}^z \right) + \mathbf{1}^z \left(\mathbf{A}^n \mathbf{U}^n + \mathbf{A}^z \mathbf{U}^p \right) = \mathbf{I}_u^p + \mathbf{I}_u^n + \mathbf{I}_u^z, \end{aligned} \quad (4.32)$$

- the waveform of the unbalanced current of the positive sequence \mathbf{I}_u^p is:

$$\mathbf{i}_u^p = \sqrt{2} \operatorname{Re} \left\{ \mathbf{I}_u^p e^{j\omega t} \right\} = \sqrt{2} \operatorname{Re} \left\{ \mathbf{1}^p \left(\mathbf{Y}_d \mathbf{U}^p + \mathbf{A}^n \mathbf{U}^z + \mathbf{A}^z \mathbf{U}^n \right) e^{j\omega t} \right\} \quad (4.33)$$

and the crms value is equal to:

$$\mathbf{I}_u^p = \mathbf{1}^p \left(\mathbf{Y}_d \mathbf{U}^p + \mathbf{A}^n \mathbf{U}^z + \mathbf{A}^z \mathbf{U}^n \right), \quad (4.34)$$

- the waveform of the unbalanced current of the negative sequence \mathbf{I}_u^n is:

$$\mathbf{i}_u^n = \sqrt{2} \operatorname{Re} \left\{ \mathbf{I}_u^n e^{j\omega t} \right\} = \sqrt{2} \operatorname{Re} \left\{ \mathbf{1}^n \left(\mathbf{Y}_d \mathbf{U}^n + \mathbf{A}^n \mathbf{U}^p + \mathbf{A}^z \mathbf{U}^z \right) e^{j\omega t} \right\} \quad (4.35)$$

and the crms value is equal to:

$$\mathbf{I}_u^n = \mathbf{1}^n \left(\mathbf{Y}_d \mathbf{U}^n + \mathbf{A}^n \mathbf{U}^p + \mathbf{A}^z \mathbf{U}^z \right), \quad (4.36)$$

- the waveform of the unbalanced current of the zero sequence \mathbf{I}_u^z is:

$$\mathbf{i}_u^z = \sqrt{2} \operatorname{Re} \left\{ \mathbf{I}_u^z e^{j\omega t} \right\} = \sqrt{2} \operatorname{Re} \left\{ \mathbf{1}^z \left(\mathbf{Y}_d \mathbf{U}^z + \mathbf{A}^n \mathbf{U}^n + \mathbf{A}^z \mathbf{U}^p \right) e^{j\omega t} \right\} \quad (4.37)$$

and the crms value is equal to:

$$\mathbf{I}_u^z = \mathbf{1}^z \left(\mathbf{Y}_d \mathbf{U}^z + \mathbf{A}^n \mathbf{U}^n + \mathbf{A}^z \mathbf{U}^p \right). \quad (4.38)$$

The load's current has five physical components:

$$\mathbf{i} = \mathbf{i}_a + \mathbf{i}_r + \mathbf{i}_u^p + \mathbf{i}_u^n + \mathbf{i}_u^z. \quad (4.39)$$

With this respect all current components are mutually orthogonal (appendix A), the three-phase rms values of the load's current are:

$$\|\mathbf{i}\|^2 = \|\mathbf{i}_a\|^2 + \|\mathbf{i}_r\|^2 + \|\mathbf{i}_u^p\|^2 + \|\mathbf{i}_u^n\|^2 + \|\mathbf{i}_u^z\|^2. \quad (4.40)$$

By multiplying (40) by the square of the rms value of the three-phase voltage $\|\mathbf{u}\|^2$, we obtain the power equation of the load supplied from an asymmetrical sinusoidal voltage source:

$$S^2 = P^2 + Q^2 + D_u^{p2} + D_u^{n2} + D_u^{z2}, \quad (4.41)$$

where individual powers are

- the apparent power:

$$S = \|\mathbf{u}\| \|\mathbf{i}\|, \quad (4.42)$$

- the active power:

$$P = \|\mathbf{u}\| \|\mathbf{i}_a\|, \quad (4.43)$$

- the reactive power:

$$Q = \|\mathbf{u}\| \|\mathbf{i}_r\|, \quad (4.44)$$

- the unbalanced power of the positive sequence:

$$D_u^p = \|\mathbf{u}\| \|\mathbf{i}_u^p\|, \quad (4.45)$$

- the unbalanced power of the negative sequence:

$$D_u^n = \|\mathbf{u}\| \|\mathbf{i}_u^n\|, \quad (4.46)$$

- the unbalanced power of the zero sequence:

$$D_u^z = \|\mathbf{u}\| \|\mathbf{i}_u^z\|. \quad (4.47)$$

The power factor λ of that circuit is equal to:

$$\lambda = \frac{P}{S} = \frac{P}{\sqrt{P^2 + Q^2 + D_u^{p2} + D_u^{n2} + D_u^{z2}}} = \frac{\|\mathbf{i}_a\|}{\|\mathbf{i}\|} = \frac{\|\mathbf{i}_a\|}{\sqrt{\|\mathbf{i}_a\|^2 + \|\mathbf{i}_r\|^2 + \|\mathbf{i}_u^p\|^2 + \|\mathbf{i}_u^n\|^2 + \|\mathbf{i}_u^z\|^2}}. \quad (4.48)$$

Three-Phase Four-Wire Circuit Supplied by Sinusoidal and Asymmetrical Voltages – The Measuring Example

The authors of the article built a three-phase four-wire system in order to verify the CPC theory for circuits supplied from an asymmetric sinusoidal voltage source (VSI). The circuit is shown in Figure 4.5.

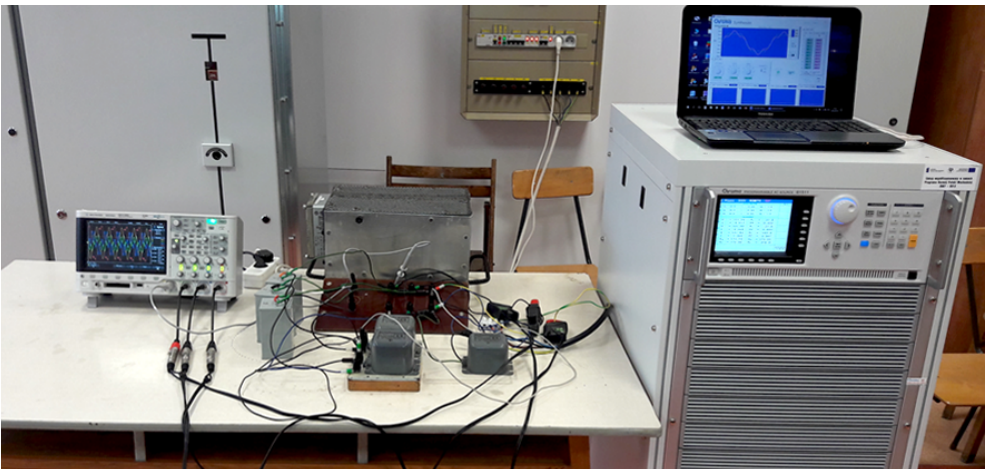


FIGURE 4.5. View of the three-phase four-wire system with the asymmetrical sinusoidal voltage source

According to the assumptions, the load shown in Figure 4.5 is linear and time-invariant (LTI). It was built of resistors, reactors, and capacitors. The parameters of individual elements are listed in Table 4.1.

TABLE 4.1. Parameters of elements used in the measurement system

Parameter	Phase R	Phase S	Phase T
Resistance	63 Ω	68 Ω	65 Ω
Inductance	460 mH	460 mH	460 mH
Capacity	9.8 μF	9.8 μF	9.8 μF
Frequency	50 Hz		

Table 4.2 lists the measured values of asymmetric sinusoidal supply voltage and line currents.

TABLE 4.2. The values of the measured supply voltage and line currents

Parameter	Phase R	Phase S	Phase T
Voltage	$79.89e^{j0^\circ}$ V	$120.02e^{j230^\circ}$ V	$100.06e^{j130^\circ}$ V
Current	$0.319e^{-j81.7^\circ}$ A	$1.886e^{j109.3^\circ}$ A	$0.373e^{j84^\circ}$ A

Figure 4.6 shows the circuit diagram from Figure 4.5.

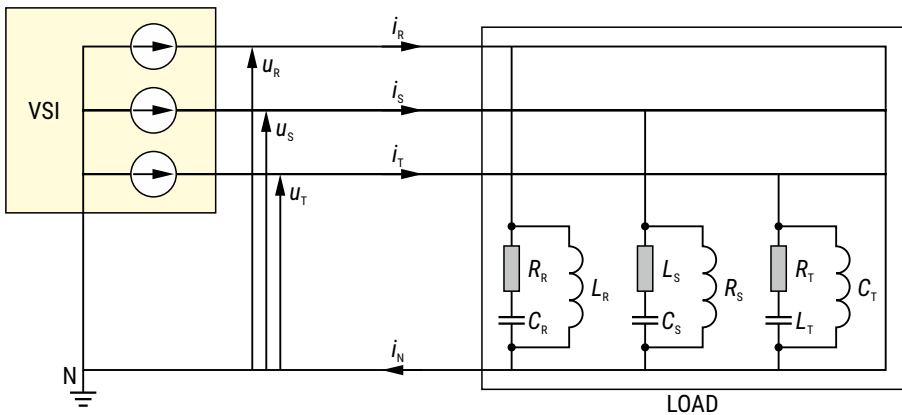


FIGURE 4.6. Diagram of the measurement circuit from Figure 4.5

On the basis of (8) three-phase rms values of supply voltage and line current are:

$$\|\mathbf{u}\| = 175.497 \text{ V}, \|\mathbf{i}\| = 1.949 \text{ A}$$

Figure 4.7 presents the waveform of the instantaneous value of the phase voltage (2).

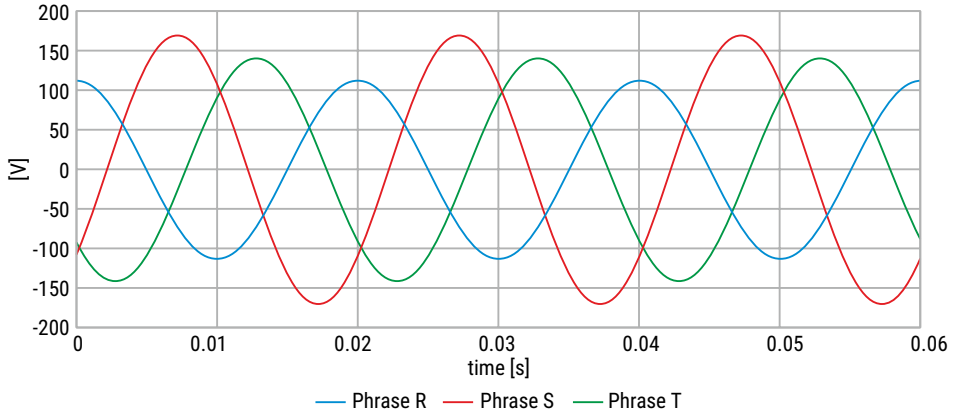


FIGURE 4.7. The waveform of the instantaneous value of the phase voltage

Figure 4.8 shows the waveform of the instantaneous current value of the line (3).

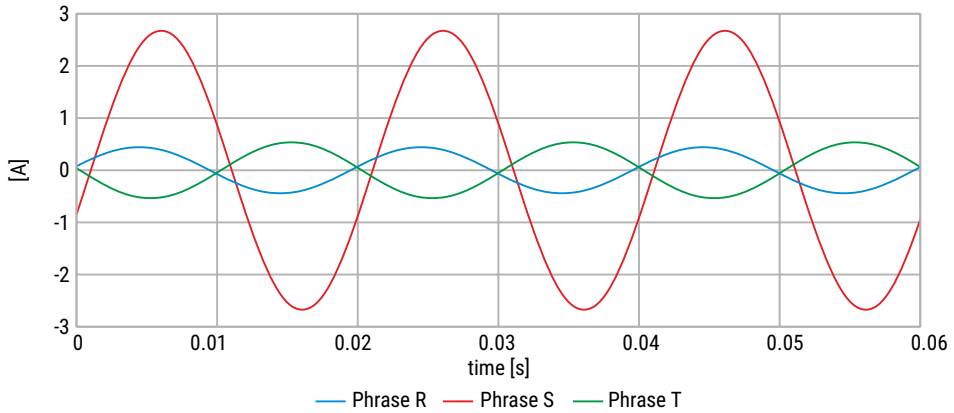


FIGURE 4.8. The waveform of the instantaneous current value of the line

According to (5) the Symmetric Fortesque Components are equal to:

$$\begin{bmatrix} U^p \\ U^n \\ U^z \end{bmatrix} = \begin{bmatrix} 98.882e^{-j0.67^\circ} \\ 6.439e^{j76.17^\circ} \\ 21.148e^{-j166.05^\circ} \end{bmatrix} \text{ V.}$$

On the basis of (4.17–21) the admittances are equal:

- $Y_b = 7.891e^{j6.6^\circ} \text{ mS}$,
- $Y_e = 5.968e^{-j3.5^\circ} \text{ mS}$,
- $Y_d = 2.268e^{-j146.1^\circ} \text{ mS}$,
- $A^n = 5.343e^{j161.4^\circ} \text{ mS}$,
- $A^z = 5.4303e^{-j93.4^\circ} \text{ mS}$.

According to (11), (12), (34), (36) and (38) the rms values of the load's currents are:

- $\|i_a\| = 1.376 \text{ A}$,
- $\|i_r\| = 0.159 \text{ A}$,
- $\|i_u^p\| = 0.257 \text{ A}$,
- $\|i_u^n\| = 1.007 \text{ A}$,
- $\|i_u^z\| = 0.896 \text{ A}$.

The waveform of the instantaneous value of the active current (9) is shown in Figure 4.9.

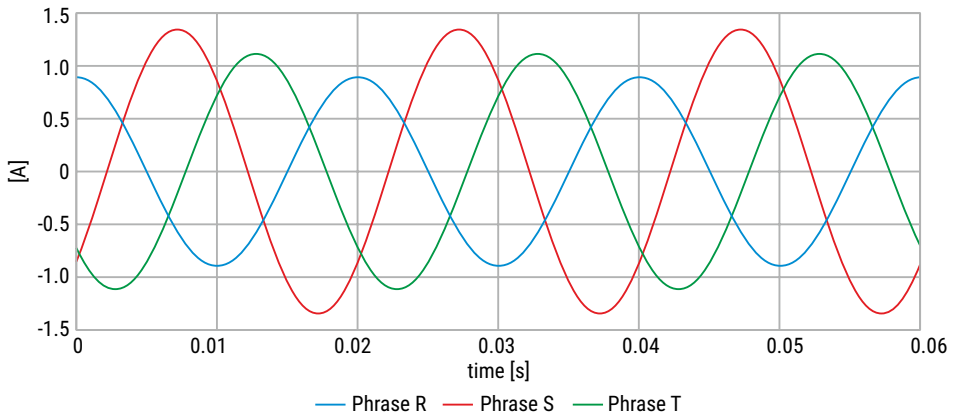


FIGURE 4.9. The waveform of the instantaneous value of the active current

Figure 4.10 presents the waveform of the instantaneous value of the reactive current (10).

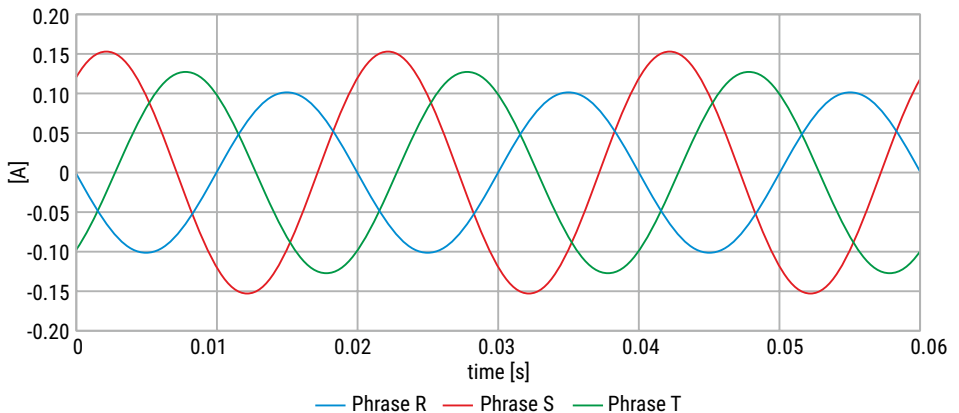


FIGURE 4.10. The waveform of the instantaneous value of the reactive current

Figure 11 shows the waveform of the instantaneous value of the unbalanced current of the positive sequence (33).

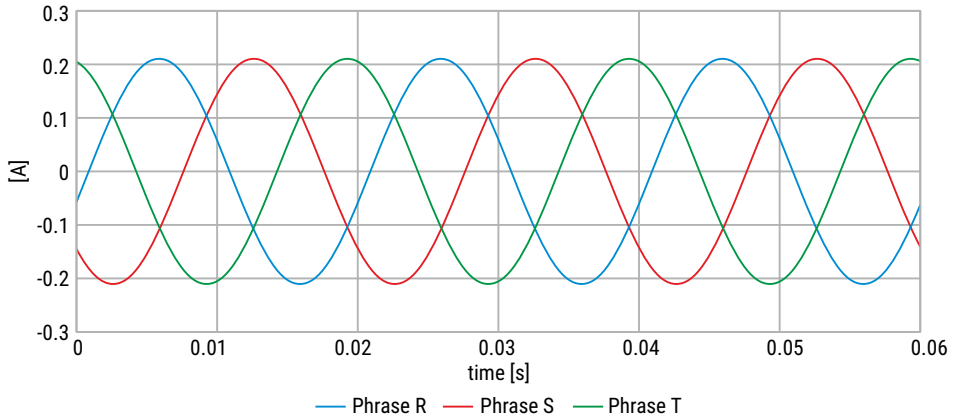


FIGURE 4.11. The waveform of the instantaneous value of the unbalanced current of the positive sequence

The waveform of the instantaneous value of the unbalanced current of the negative sequence (35) is shown in Figure 4.12.

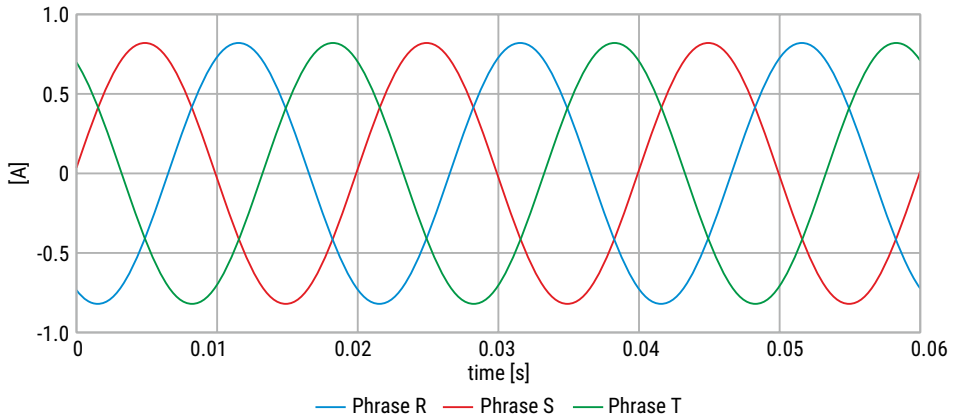


FIGURE 4.12. The waveform of the instantaneous value of the unbalanced current of the negative sequence

Figure 4.13 presents the waveform of the instantaneous value of the unbalanced current of the zero sequence (37).

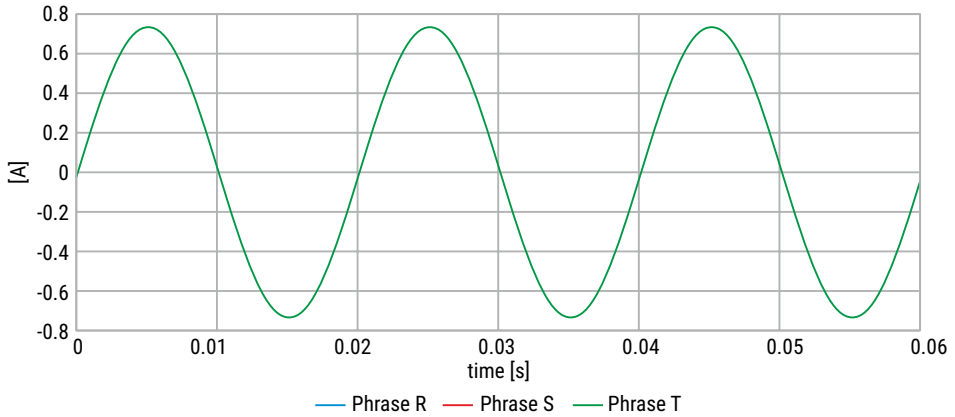


FIGURE 4.13. The waveform of the instantaneous value of the unbalanced current of the zero sequence

Summing up the instantaneous waveforms of the component currents of the load shown in Figures 4.9–4.13, we obtain the instantaneous waveform identical to that shown in Figure 4.8. In addition, according to (40), the three-phase rms value of the line current is equal to the three-phase rms value expressed by (8).

Conclusion

The article shows that the physical components of the load’s current are associated with specific physical phenomena and are possible to describe in the asymmetry of the supply voltage.

Chapter III presents the measurements of electrical quantities, i.e. asymmetrical sinusoidal supply voltage and the line current of the unbalanced load. As it has been proved, the distribution of the measured line current by dependencies derived in Chapter II makes it possible to determine the physical components of the current of the load. In addition, each of the current components is mutually orthogonal, which means the opportunity to calculate the balancing reactance compensator parameters contributing to the compensation of reactive power and balancing the load.

The equations shown in this article allow for describing three-phase four-wire systems with the asymmetrical sinusoidal supply voltage. This is another step in the development of the Currents’ Physical Components Theory, which was until then described only with symmetrical power supply.

In addition, this is the commencement of the description of the possibility to determine the parameters of the balancing reactance compensator in asymmetrical four-wire power systems supplied from a sinusoidal or non-sinusoidal voltage source.

Appendix – Orthogonality

Vectors are mutually orthogonal when the three-phase scalar product [1,2] is equal to zero:

$$(\mathbf{x}, \mathbf{y}) = \frac{1}{T} \int_0^T \mathbf{x}(t)^T \cdot \mathbf{y}(t) dt = 0. \quad (4.A1)$$

If three-phase quantities are expressed in the form of complex rms values, namely:

$$\mathbf{x} = \sqrt{2} \text{Re}\{\mathbf{X}e^{j\omega t}\}, \quad \mathbf{y} = \sqrt{2} \text{Re}\{\mathbf{Y}e^{j\omega t}\}, \quad (4.A2)$$

then their scalar product is equal to:

$$(\mathbf{x}, \mathbf{y}) = \frac{2}{T} \int_0^T \text{Re}\{\mathbf{X}^T e^{j\omega t}\} \text{Re}\{\mathbf{Y}e^{j\omega t}\} dt = \text{Re}\{\mathbf{X}^T \mathbf{Y}^*\}. \quad (4.A3)$$

The active and reactive currents are mutually orthogonal since they are shifted by a quarter of a period. There remains the question of the orthogonality of the sum of these currents relative to the unbalanced current. The value of the scalar product of these currents is:

$$\begin{aligned} (\mathbf{i}_b, \mathbf{i}_u) &= \text{Re}\{\mathbf{I}_b^T \mathbf{I}_u^*\} = \text{Re}\left\{\mathbf{I}_b^T (\mathbf{I} - \mathbf{I}_b)^*\right\} = \text{Re}\left\{\mathbf{Y}_b \mathbf{U}^T (\mathbf{I} - \mathbf{Y}_b \mathbf{U})^*\right\} = \\ &= \text{Re}\left\{\mathbf{Y}_b \mathbf{U}^T \mathbf{I}^* - \mathbf{Y}_b \mathbf{U}^T \mathbf{Y}_b^* \mathbf{U}^*\right\} = \text{Re}\left\{\mathbf{Y}_b (\mathbf{U}^T \mathbf{I}^* - \mathbf{U}^T \mathbf{Y}_b^* \mathbf{U}^*)\right\} = \text{Re}\left\{\mathbf{Y}_b (\mathbf{C} - \mathbf{C}_b)\right\} = 0. \end{aligned}$$

The currents of the positive and negative sequence are mutually orthogonal because of the opposite of their sequence. The scalar product of the unbalanced current of the positive and zero sequence $(\mathbf{i}_u^p, \mathbf{i}_u^z)$ is calculated as follows:

$$\begin{aligned} (\mathbf{i}_u^p, \mathbf{i}_u^z) &= \text{Re}\left\{\mathbf{I}_u^{pT} \mathbf{I}_u^{z*}\right\} = \\ &= \text{Re}\left\{\left(\mathbf{1}^p (\mathbf{Y}_d \mathbf{U}^p + \mathbf{A}^n \mathbf{U}^z + \mathbf{A}^z \mathbf{U}^n)\right)^T \cdot \left(\mathbf{1}^z (\mathbf{Y}_d \mathbf{U}^z + \mathbf{A}^n \mathbf{U}^n + \mathbf{A}^z \mathbf{U}^p)\right)^*\right\} = \\ &= \text{Re}\left\{\left(\mathbf{Y}_d \mathbf{U}^p + \mathbf{A}^n \mathbf{U}^z + \mathbf{A}^z \mathbf{U}^n\right)^T \cdot \left(\mathbf{Y}_d \mathbf{U}^z + \mathbf{A}^n \mathbf{U}^n + \mathbf{A}^z \mathbf{U}^p\right)^* (1 + \alpha^* + \alpha)\right\} = 0 \end{aligned}$$

and the unbalanced current of the negative and zero sequence $(\mathbf{i}_u^n, \mathbf{i}_u^z)$:

$$\begin{aligned} (\mathbf{i}_u^n, \mathbf{i}_u^z) &= \text{Re}\left\{\mathbf{I}_u^{nT} \mathbf{I}_u^{z*}\right\} = \\ &= \text{Re}\left\{\left(\mathbf{1}^n (\mathbf{Y}_d \mathbf{U}^n + \mathbf{A}^n \mathbf{U}^p + \mathbf{A}^z \mathbf{U}^z)\right)^T \cdot \left(\mathbf{1}^z (\mathbf{Y}_d \mathbf{U}^z + \mathbf{A}^n \mathbf{U}^n + \mathbf{A}^z \mathbf{U}^p)\right)^*\right\} \\ &= \text{Re}\left\{\left(\mathbf{Y}_d \mathbf{U}^n + \mathbf{A}^n \mathbf{U}^p + \mathbf{A}^z \mathbf{U}^z\right)^T \cdot \left(\mathbf{Y}_d \mathbf{U}^z + \mathbf{A}^n \mathbf{U}^n + \mathbf{A}^z \mathbf{U}^p\right)^* (1 + \alpha + \alpha^*)\right\} = 0. \end{aligned}$$

With respect to the fact that all currents are mutually orthogonal, relationship (40) is accomplished.

Authors: Z. Soljan (e-mail:z.soljan@pb.edu.pl), M. Dziemiańczyk (e-mail: michaldziemiańczyk@gmail.com), Białystok University of Technology, Faculty of Electrical Engineering, Wiejska 45D Str., 15-351 Białystok, Poland.

References

- [1] L.S. Czarnecki, "Power in electrical circuits with nonsinusoidal waveform of currents and voltages," *Oficyna Wydawnicza Politechniki Warszawskiej*, Warszawa, pp. 136–145, 2005 [in Polish].
- [2] L.S. Czarnecki, "Orthogonal decomposition of the currents in a three-phase nonlinear asymmetrical circuit with nonsinusoidal voltage source," *IEEE Trans. IM*, Vol. 37, No. 1, pp. 30–34, 1988.
- [3] C. I. Budeanu, "Puissances reactives et fictives," Institut Romain de l'Energie, Bucharest.
- [4] H. Akagi, Y. Kanazawa, A. Nabae, "Generalized theory of the instantaneous reactive power in three-phase circuits," *Proceedings of JIEE-IPEC*, pp. 1375–1380, 1983.
- [5] H. Kim, F. Blaabjerg, B. Bak-Jensen, J. Choi, "Instantaneous power compensation in three-phase systems by using p-q-r theory," *IEEE Trans. on Power Electr.*, Vol. 17, No. 5, pp. 701–710, 2002.
- [6] P. Tenti, H. K. Morales Paredes, P. Mattavelli, "Conservative power theory, a framework to approach control and accountability issues in smart microgrids," *IEEE Trans. on Power Electr.*, Vol. 26, No. 3, pp. 664–673, 2011.
- [7] C.I. Fortescue, "Method of symmetrical co-ordinates applied to the solution of polyphase networks," *34th An. Con. Of the Amer. Inst. Of Electr. Eng.*, pp. 1027–1140, 1918.
- [8] Petrascu, M. Popescu, V. Suru, "CPC theory implementation for active filtering and its limits," *Inter. Conf. on App. And Theo. Electr. (ICATE)*, pp. 1–6, 2012.
- [9] N. Jelani, M. Molinas, "Shunt active filtering by constant power load in microgrid based on IRP p-q and CPC reference signal generation scheme," *IEEE Inter. Conf. on Pow. Sys. Techn. (POWERCON)*, pp. 1–6, 2012.
- [10] H. Ginn, G. Chen, "Switching compensator control strategy based on CPC power theory," *Inter. Sch. On Nonsin. Cur. And Comp.*, pp. 1–11, 2008.
- [11] H. Akagi, A. Nabae, "Control strategy of active power filters using multiple voltage-source PWM converters," *IEEE Trans. On Ind. App.*, Vol. IA-22, No. 3, pp. 460–465, 1986.
- [12] O. Montes, G. Ramos, "Instantaneous p-q theory for harmonic compensation via shunt active power filter," *Work. On Pow. Elect. And Pow. Qual. App. (PEPQA)*, pp. 1–4, 2013.
- [13] G. S Raj, K. Rathi, "P-Q theory based shunt active power filter for power quality under ideal and non-ideal grid voltage conditions," *IEEE Inter. Conf. on Pow., Inst., Cont. and Comp. (PICC)*, pp. 1–5, 2015.
- [14] M. Aredes, H. Akagi, E. H. Watanabe, E. V. Salgado, L. F. Encarnacao, "Comparison between the p-q and p-q-r theories in three-phase four-wire systems," *IEEE Trans. On Pow. Elect.*, Vol. 24, No. 4, pp. 924–933, 2009.
- [15] T. D. Rachmildha, A. Llor, M. Fadel, P. A. Dahono, Y. Haroen, "Hybrid direct power control using p-q-r power theory applied on 3-phase 4-wire active power filter," *IEEE Pow. Elect. Spec. Conf.*, pp. 1183–1189, 2008.
- [16] F. Z. Peng, G. W. Ott, D. J. Adams, "Harmonic and reactive power compensation based on the generalized instantaneous reactive power theory for 3-phase 4-wire systems," *Ann. IEEE Pow. Elect. Spec. Conf.*, Vol. 2, pp. 1089–1095, 1997.
- [17] F. Z. Peng, J. S. Lai, "Generalized instantaneous reactive power theory for three-phase power systems," *IEEE Trans. On Inst. And Meas.*, Vol. 45, No. 1, pp. 293–297, 1996.

- [18] Nabae, T. Tanaka, "A new definition of instantaneous active-reactive current and power based on instantaneous space vector on polar coordinates in three-phase circuits," *IEEE Trans. On Pow. Deliv.*, Vol. 11, No. 3, pp. 1238–1243, 1996.
- [19] L.S. Czarnecki, P. Bhattarai, "Currents' Physical Components (CPC) in three-phase systems with asymmetrical voltage," *Przegl. Elektr.*, Vol. 91, No. 6, pp. 40–47, 2015.
- [20] L.S. Czarnecki, P. Bhattarai, "Reactive compensation of LTI loads in three-wire systems at asymmetrical voltage," *Przegl. Elektr.*, Vol. 91, No. 12, pp. 7–11, 2015.
- [21] L.S. Czarnecki, P. Bhattarai, "Power and compensation in circuits with distorted and asymmetrical current and voltage waveforms. Vol. 8, Power and compensation of circuits with asymmetrical supply voltage," *Aut., Elektr., Zakł.*, Vol. 6, No. 1(19), pp. 8–18, 2015 [in Polish].
- [22] L. S. Czarnecki, P. M. Haley, "Unbalanced power in four-wire systems and its reactive compensation," *IEEE Trans. On Pow. Deliv.*, Vol. 30, No. 1, pp. 53–63, 2015.
- [23] L. S. Czarnecki, P. M. Haley, "Reactive compensation in three-phase four-wire systems at sinusoidal voltages and currents," *Int. Sch. On Nonsin. Curr. And Comp. (ISNCC 2013)*, pp. 1–6, 2013.
- [24] Z. Sołjan, G. Hołdyński, M. Zajkowski, "Description of systems supplied by asymmetrical sinusoidal voltage according to the Currents' Physical Components Theory," *Wiad. Elektr.*, Vol. 87, No. 4, pp. 10–18, 2019 [in Polish].
- [25] Z. Sołjan, G. Hołdyński, M. Zajkowski, "The mathematical concept of the currents' asymmetrical components in three-phase four-wire systems with sinusoidal and asymmetric voltage supply," *Bull. of the Pol. Acad. of Scien.: Techn. Scien.*, Vol. 67, No. 2, pp. 271–278, 2019.

Chapter 5

Improving the cooling efficiency of industrial electronic components with the use of planar porous heat sinks

*Adam Steckiewicz, Gabriela Druć and Jacek Maciej Stankiewicz
Bialystok University of Technology, Faculty of Electrical Engineering*

The article presents an analysis of the cooling efficiency of planar porous heat sinks, dedicated to improve thermal operating conditions of some electronic components. A single axial coil, placed on the laminate and convectionally cooled by a 2D laminated heat sink, was examined. The coil was supplied by a low frequency electric current. The three-dimensional numerical model of an electronic system was computed using the finite element method (FEM). Three cases are considered, where the element was operating without additional passive cooling, with the heat sink formed as a homogeneous copper plate as well as the element combined with the planar heat sink with modified internal structure.

Index terms: temperature distribution, printed circuit board, passive cooling, thermal energy efficiency

Introduction

Power and industrial electronics grapple with the efficient cooling of electronic components and elements which are often enclosed in the smallest possible packages [1, 2]. The reduction of energy consumption by electric devices as well as constant demand for their effective work, force designers to utilize passive, instead of active, cooling structures [3] in the most sensitive parts of a circuit. The most popular plate and fin heat sinks, including those with complex project and implementation based on the 3D printing technique [4], are relatively massive and occupy a lot of space. Additionally, in the case of electronic elements with round shapes, one may find some difficulties with assembling a cooling and operating device together. This indicates that solutions which allow cooling electronic components with minimal cost, sizes and energy consumption are needed [5].

The most popular methods of dissipating the heat are additional passive structures. There are many solutions, such as thermal vias system filled with a high thermal conductivity material [6, 7] or planar, thermally conductive plates for increasing effective surface which dissipate heat from the electronic elements [8]. They are placed directly on or under the cooled element [9, 10] as well as on the other side of the printed circuit board (PCB) and connected with an element by thermal bridges. Those solutions dissipate lower power (less than several watts [11]) than fin heat sinks or active cooling; however their compact and build-in laminate structure allows for an application in systems with complex geometry.

The determination of an element's temperature during the steady state, under given ambient conditions, gives an ability to estimate its reliability and stability. There are several methods of temperature field analysis, such as analytical [12] and numerical approaches [13, 14], where calculations are carried out in the time-domain or steady state in systems characterized by heterogeneous thermal conductivity distribution. Utilizing an electrical-analog model, it is possible to analyze thermal effects using a lumped model [15]. Thermal resistance and capacity can be determined, for example on the basis of a comparison with measurement results or by identification technique using optimization methods [16]. Every overrun of critical temperature for a considered system may lead to thermal damage (e.g. local melting of the structure) or disturbances of the system and surrounding objects [9].

Reduced size (order of mm) and round geometry (small contact surface with a cooling device) may introduce difficulties with dissipation of generated or accumulated heat. One of the solutions is "printing" flat, thermally conductive structure under the cooled element [11]. Uniform lamina [2] or a "dog bone" plate [1] are exemplary solutions. If such a heat sink is placed on PCB, then etching the copper layer may lead to a structure consisting of periodically arranged pores inside the cooling plate, which will increase effective surface dissipating heat, thereby reducing the temperature of an electronic element [16].

In this paper we analyze an exemplary part of an electronic circuit with an axial coil. The heat is dissipated from the element by natural convection. We discuss the cases without passive cooling and configurations where planar porous heat sinks with modified internal design were applied. The aim of the study is to investigate the efficiency of this type of passive cooling structures. On the basis of the obtained results, the optimum structure is determined, where the terms of decreasing the coil's temperature and reducing material are the most crucial. The element's temperature and thermal field distribution depending on the ambient temperature, heat sink design and supply current are shown and characterized.

Methods

Electric and thermal field analysis

The operating conditions of components within the electrical system satisfy the overall power balance

$$Q_I + Q_G - Q_O - Q_A = 0. \tag{5.1}$$

Undesirable temperature change in an element is a result of its unbalance, where both input Q_I and generated power Q_G have to be equal to output power Q_O . The accumulated power Q_A is a difference between them. A decrease in the temperature value of the considered element is directly related with the decrease of Q_A . Additionally, the parasitic interactions inside the system are indirectly limited. Decreasing the temperature statistically increases mean time between failures as well as improves the efficiency of entire system. Then, prolonged work of the element is possible for provided power supply parameters or even at insignificant overload.

The analysis was focused on hybrid systems with surface-mount technology. The input power Q_p , resulting from thermal conduction between packaged components, consists of the heat conducted to an element and transmitted by other interactions (e.g. radiation). These factors are highly dependent on the system's geometry and casing. The impact of parasitic effects has been taken into account indirectly, by assuming the ambient temperature T_{ext} . The power dissipated in components surrounding the considered element will increase the internal temperature and cause a general deterioration of the heat transfer conditions.

Heat power generation is a result of the changes of energy, occurring due to an electric power supply and related with parasitic effects. Hence, the generated power Q_G characterizes possible changes in temperature distribution resulting from energy transformations. In the case of an axial coil the generated power consists of eddy current losses, hysteresis losses and the heat from the alternating current flowing through resistive material (winding). The power Q_G is also affected by phenomena related to thermal and electromagnetic field interactions.

The power generated in the system is dissipated as a result of the conduction, convection and radiation phenomena. The purpose of the presented technical solution is to increase power Q_O , dissipated from the element by introducing build-in planar heat sinks integrated with PCB. A heat sink is a part of laminate, where its geometry and layout (circuit paths placed at the bottom of a plate) are intended to increase conducted heat and transfer it to the ambient by convection and radiation.

The discussed phenomena are described by differential equations, which take into account material heterogeneity. The voltage distribution V in [V] satisfy the differential equation

$$\nabla \cdot (\sigma \nabla V) = 0, \quad (5.2)$$

where σ is electric conductivity in [S/m]. The vector of a current density distribution \mathbf{J} in [A/m²] inside the element is defined as

$$\mathbf{J} = \sigma \mathbf{E}, \quad (5.3)$$

where:

\mathbf{E} – electric field vector in [V/m].

Taking into account only conduction currents, the power density distribution p in [W/m³] is described by a formula

$$p = \frac{|\mathbf{J}|^2}{\sigma}. \quad (5.4)$$

Due to low-frequency current, expected values of magnetic induction and application of a ferrite core, the eddy current and hysteresis losses were omitted. Their values, based on analytic calculations, did not exceed 1.16% of the ohmic losses. From the perspective of the analysis of thermal working conditions, taking these losses into account does not change the general assumptions and conclusions. An increase in considered power losses was observed in an area close to the ohmic loss. On this basis the temperature T in [°C], in thermal steady state, can be calculated using

$$\nabla \cdot (\lambda \nabla T) = -p, \quad (5.5)$$

where: λ is the thermal conductivity of a material in [W/mK].

We have considered conjugate phenomena occurring in electric and thermal fields. The temperature distribution in the system was described by (5.5) and solved on the basis of the calculated current density values using (5.2) and (5.3).

Numerical model of the system

We have considered the part of electronic system (Fig. 5.1) with the element mounted on a laminate. Both working conditions as well as axial coil Πe of the length $de = 15$ mm and base diameter $\Phi e = 7.5$ mm were analyzed. The coil, covered by epoxy resin, had an internal ferrite core and winding with resistance of $R = 1.4 \Omega$.

The coil was mounted in the central part of the system, whose base Πp was an insulator (FR-4) with dimensions $dx \times dy \times dz$ equal to $25 \times 25 \times 1$ mm, respectively. The copper contacts Πs of a thickness $dl = 0.07$ mm provided current supply to the element, connected to contacts Πs by leads Πd (diameter $\Phi d = 0.7$ mm). Typical layout was complemented by a printed copper heat sink, introduced as an area Πr with dimensions of $de \times dy \times dl$. Its purpose was to dissipate the heat from Πe to the ambient with constant temperature T_{ext} by natural convection.

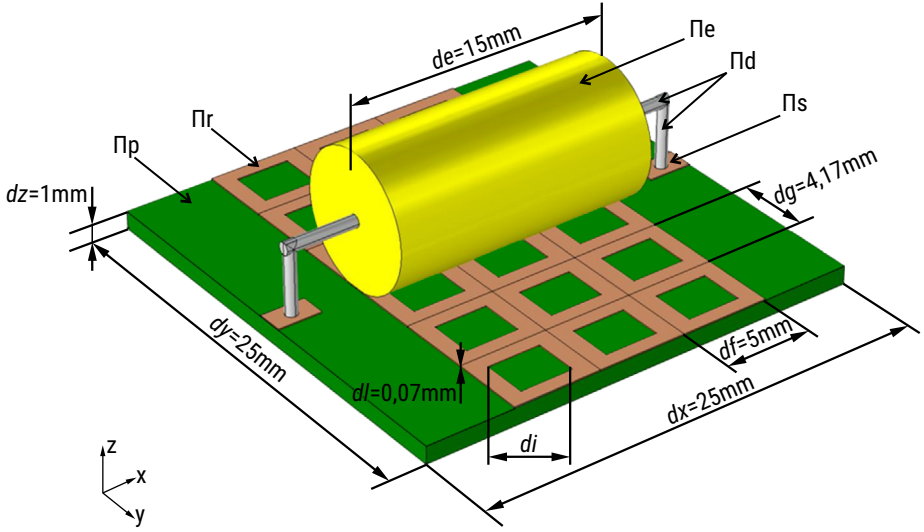


FIGURE 5.1. A view on the analyzed model with specified dimensions

The properties of the heat sink Πr with constant external dimensions were adjusted by modification of internal geometry. The structure was synthesized of 18 unit cells with dimensions $df \times dg \times dl$ ($5.00 \times 4.17 \times 0.07$ mm). The change of the diagonal of inner opening di modifies the geometry of the cell, which has a direct effect on reducing the amount of copper forming the heat sink and increasing the porosity of the cooling structure. Due to a specific geometry of the heat sink we are able to specify its structure using parameter

$$k_v = \frac{v_k}{v_c} = \frac{v_c - v_i}{v_c} = 1 - \frac{v_i}{df \cdot dg \cdot dl}, \quad (5.6)$$

where:

v_k – volume of a single unit cell in $[m^3]$;

v_c – volume of uniform rectangular structure of a size $df \times dg \times dl$ in $[m^3]$;

v_i – volume of an internal resection of a diagonal di in $[m^3]$.

This parameter characterizes the relation between the volume of the porous heat sink and the uniform cooling plate. For the homogeneous heat sink $di = 0$ and $k_v = 1$, however, when the parameter is $di = \sqrt{df^2 + dg^2}$, the heat sink area is reduced to zero ($k_v = 0$). By adjusting di value, it is possible to form a periodic array (Fig. 5.2), whose internal resection led to different cooling efficiency. In order to specify those properties of the heat sink we have proposed the parameter

$$e = \left[1 - \frac{T_{k,\max}}{T_{\vartheta,\max}} \right] \cdot 100\%. \quad (5.7)$$

The value of the temperature decrease effectiveness (e) was calculated on the basis of: $T_{k,max}$ – maximum temperature in the system cooled by optimal porous heat sink ($k_v = 0.6$) in [°C] and $T_{\vartheta,max}$ – maximum temperature in the system cooled by uniform heat sink ($T_{\vartheta,max} = T_{j,max}$) or without any cooling structure ($T_{\vartheta,max} = T_{b,max}$) in [°C].

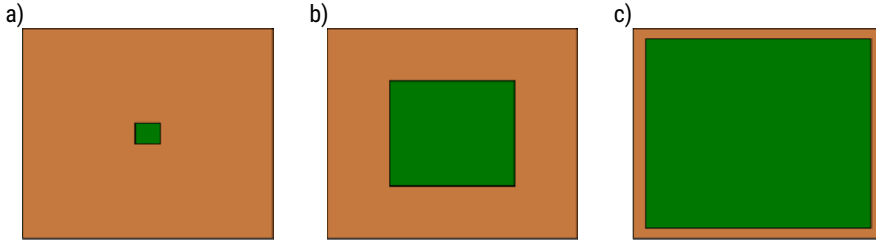


FIGURE 5.2. Exemplary periodic porous structures: a) $di = 0.65$ mm ($k_v = 0.99$); b) $di = 3.25$ mm ($k_v = 0.75$); c) $di = 5.86$ mm ($k_v = 0.19$)

The cooling conditions as well as the spectrum and effective value of supply current are known. The excitation is added to the numerical model as a constant current density $\mathbf{J} = [J_x \ 0 \ 0]$ at terminals Π s of the element. Current density distribution as well as winding resistance determine the intensity and heat sources distribution in the system.

The Joule-Lenz heat dissipated in the electronic element is a distributed excitation for thermal field calculations, introduced upon the electric field distribution. In a steady state the thermal field depended on two key phenomena:

- heat conduction from generation area (coil interior) by contacts, material connections and thermal bridges to other objects in the system,
- heat transfer to the ambient by convection and radiation phenomena.

Therefore, according to the presented assumptions, the natural convection boundary conditions (no forced airflow) are assigned to the external boundaries of the system. The field problem is solved using the finite element method (FEM), where the presented model was discretized in a 3-dimensional space using a tetrahedral h-adaptive mesh.

Results

Impact of heat sink structure on element temperature

The considered system was computed numerically. The coil was supplied by low-frequency, nominal current. Temperature distribution at the surface of the model depends on the geometry of heat sink, localized on PCB and assembled with an electronic element (Fig. 5.3).

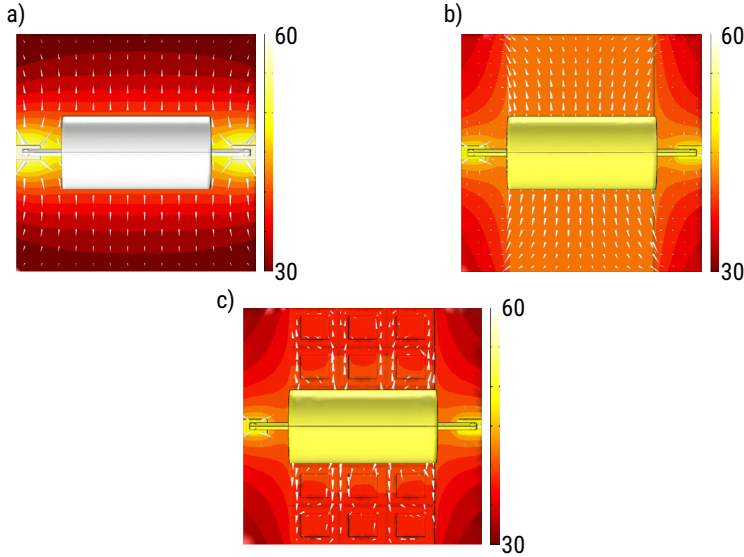


FIGURE 5.3. Temperature distribution (yz plane) and heat flow conducted through the surface of the structure at $T_{ext} = 20^\circ\text{C}$ and $I = I_n$ in the system: a) without passive cooling; b) cooled by uniform plate; c) cooled by porous heat sink

The system without the heat sink was characterized by the highest temperature values and heat flowing through copper contacts and leads (Fig. 5.3a). When the planar heat sink was placed, temperature distribution changed. For example, temperature values became more uniform at central area and the heat flux started to flow from the element to the upper and bottom edge through the heat sink's surface. However, the porous heat sink (Fig. 5.3c) had an approximately identical temperature as a laminate and heat flux appeared in the contact area between the element and the cooling plate. In the same region the most part of the heat was dissipated to the ambient.

For the assumed convective cooling conditions (natural, unforced convection) and current supply, the relation between the coil's maximum temperature and k_v (Fig. 5.4) were obtained. When $k_v = 0$, it meant that no heat sink was presented, however, for $k_v = 1$ the heat sink was a homogeneous plate. Intermediate values of k_v characterized different porous heat sinks. In a steady state, the temperature of the element depended significantly on the cooling conditions (Fig. 5.4). The reference temperature $T_0 = 65,954^\circ\text{C}$ was a maximum value at the surface of coil without any cooling structure at nominal operating conditions ($I = I_n = 0.655\text{A}$ and $T_{ext} = 20^\circ\text{C}$). When the amount of copper in the heat sink's structure increased, the temperature value decreased to $0.8T_0$. After $k_v = 0.65$, temperature raised to $0.85T_0$. When the coil was cooled by the uniform plate ($k_v = 1$), the temperature was approximately 15% lower than without the heat sink. For some porous heat sinks ($0.3 < k_v < 0.9$) we were able to achieve identical or more efficient cooling performance with a minimum temperature at $k_v = 0.6$. It was a result of dissipating heat by the entire heat sink and the laminate's surface as well as by internal side surfaces of the pores.

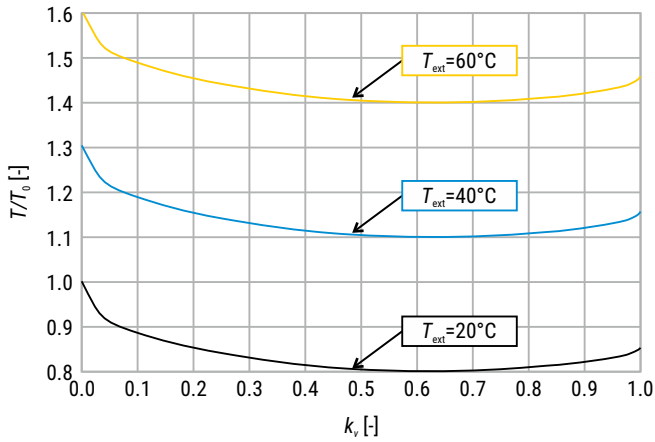


FIGURE 5.4. Maximum relative temperature for different heat sinks and T_{ext} , $l = ln$

Numerical computations were performed for three cooling conditions which were modeled as different ambient temperatures T_{ext} . A significant impact of T_{ext} on heat transfer in the system was clearly observed. In a steady state and at $T_{ext} = 60^\circ\text{C}$, the maximum temperature raised more than 60%, compared to the $T_{ext} = 20^\circ\text{C}$ case. Additionally, a higher temperature decreased cooling effectiveness when any type of planar heat sink was used. For example, at $k_v = 0.6$ and $T_{ext} = 20^\circ\text{C}$ coil temperature was reduced by 20% compared to the case without the heat sink, although at $T_{ext} = 40^\circ\text{C}$ the relative change was 15%.

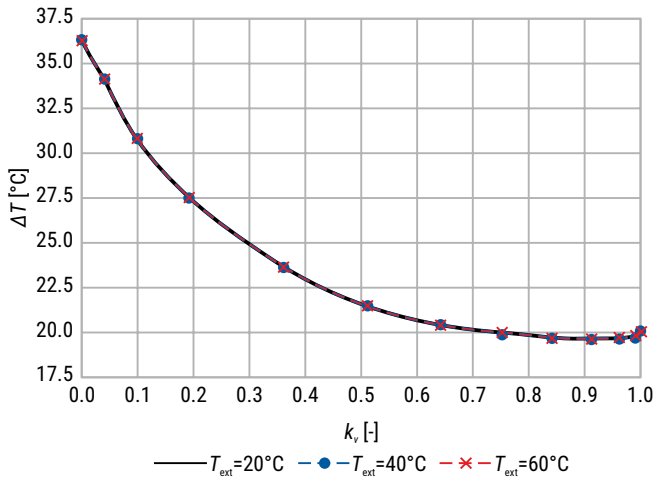


FIGURE 5.5. Temperature difference between the hottest and coolest point at the system surface for different heat sink structures at $T_{ext} = \text{var}$ and $l = ln$

We also defined the temperature difference ΔT between the warmest (coil surface) and coolest (laminate surface) points of the system. The application of planar heat sinks has a positive impact on temperature difference reduction (Fig. 5.5). We observed an exponential decrease with increasing k_v . In an optimal case ($k_v = 0.9$) maximum $\Delta T = 19.5^\circ\text{C}$, while at $k_v = 0$, the temperature difference was almost twice higher ($\Delta T = 36^\circ\text{C}$). What is more, external temperature has no impact on ΔT since curves for different T_{ext} overlapped each other. For $k_v = 0.6$, which was an optimal structure for cooling the element, ΔT decreased to 20.38°C , which means that it was 2.44% less effective than the uniform heat sink.

Current load impact on heat sink efficiency

From a practical point of view it is also important to define thermal operating conditions for electronic elements at different than nominal current supply. An ability to overload electronic elements is acceptable in particular situations; however it is the reason of possible damage to electronic components due to exceeding the recommended temperature range. For the considered coil, the maximum operating temperature was $T_m = 125^\circ\text{C}$. Numerical analysis for three variants:

- the system without the heat sink,
- the system with the uniform copper plate,
- the system with the optimal porous heat sink ($k_v = 0.6$),

was intended to find the relation between mean temperature of the coil and supply current. The cooling effectiveness was also investigated for the coil supplied by current ranging from $0 \div 2I_n$ (Fig. 5.6). We defined temperature decrease effectiveness when using the porous heat sink, with relation to the system without the cooling device and with the uniform heat sink (Fig. 5.7).

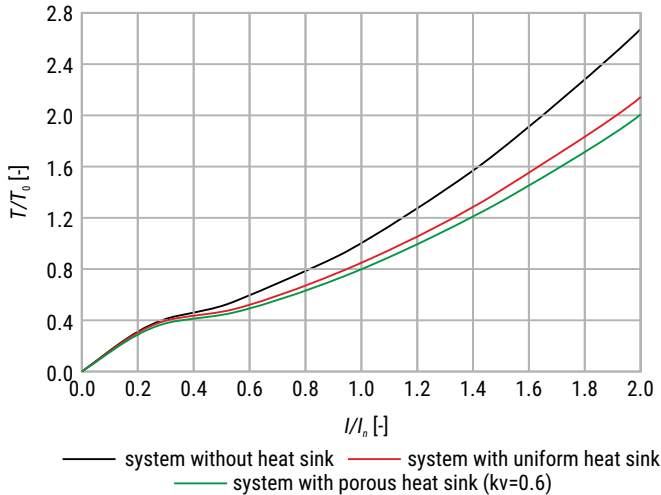


FIGURE 5.6. Maximum relative temperature for different supply currents and three types of the systems at $T_{ext} = 20^\circ\text{C}$

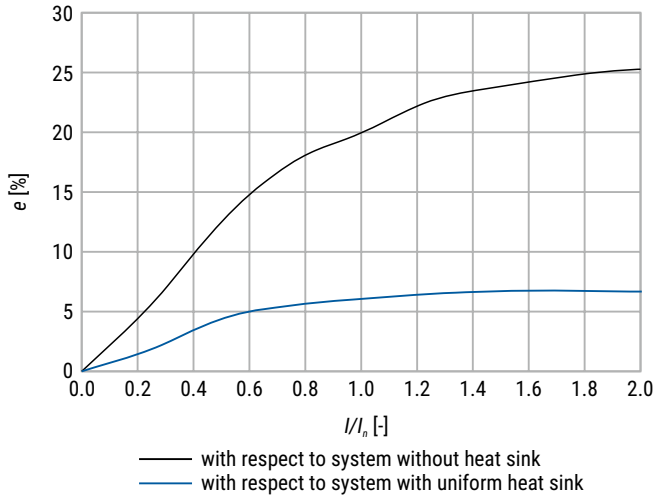


FIGURE 5.7. Temperature decrease effectiveness of a coil with porous heat sink for different supply currents at $T_{ext} = 20^\circ\text{C}$

When the element was supplied by low-value current ($0 \div 0.4I_n$), the coil's temperature was similar despite the heat sink structure (Fig. 5.6). For higher currents, differences in temperature values and a change in cooling effectiveness were observed. Maximum operating temperature for coil $T_m = 1.9T_0$ was reached without the heat sink at $I = 1.55I_n$, however, with the porous heat sink it was $I = 1.95I_n$. In other words, the optimal planar heat sink gave an ability to overload the element by current almost twice higher than nominal, but still preserved the recommended temperature range.

It is also possible to interpret the obtained results in a reversed relation. For example, at $I/I_n = 1.2$ relative temperature of the system without the heat sink was $T/T_n \approx 1.3$, but for the optimal porous cooling structure ($k_v = 0.6$) it was $T/T_n = 0.95$. In this variant, the coil's operating conditions will be preserved. Furthermore, mean time between failures will lengthen since critical operating conditions will not be achieved.

According to formula (5.7) we calculated the cooling effectiveness which is a relative temperature decrease of the element for different supply currents. An optimal porous heat sink was able to reduce (at $I = 0.5I_n$) mean temperature of the coil by 12.5% with relation to the system without any cooling device and 4% to the system with the uniform heat sink. This effectiveness increased with increasing current, hence at $I = 2I_n$ the temperature was decreased by 25.4% and 6.68% respectively. The obtained characteristics (Fig. 5.6 and Fig. 5.7) indicate that the cooling effectiveness of porous heat sinks raises at higher current values. The optimal porous structure is even more effective than the uniform one. This may lead to mass reduction, where after applying the porous heat sink there is a possibility to use 80% less material ($k_v = 0.2$) and preserve similar cooling performance (Fig. 5.4, Fig. 5.6) as a homogeneous plate.

Conclusions

The paper presents an analysis and the results of the thermal operation conditions of an exemplary, conventionally cooled electronic device. The cooling effectiveness of an axial coil is discussed, before and after the periodic low-power heat sink with modified internal geometry was applied. Several different thermal conditions, at which a coil was operating, were investigated and analyzed. The electronic device, supplied by the low frequency AC current, was combined with planar cooling structures. In addition, some cases where the coil was carrying current different than nominal were considered. Then, we compared the cooling effectiveness of the homogeneous plate and porous, periodic heat sinks. Numerical calculations of the model were performed by finite element method (FEM), in order to solve the conjugate heat transfer field problem, simulated in a three-dimensional coordinate system.

The numerical results indicate very different thermal field distributions at the surface of the entire model for the cases, where planar cooling structures with different geometries were simulated. The application of these porous heat sinks allowed for lowering the temperature of the electronic device by 20%, compared with the case without heat sink. The discussed structures were also at least 6% more effective at cooling the coil than the homogeneous copper plate. Furthermore, the cooling effectiveness of the axial coil rose with higher values of the supplying current, which theoretically allows for overloading the device with current higher than nominal. In this situation, mean temperature may be reduced by 25% compared with the case without the heat sink. The porous heat sink gives an ability to achieve better or at least identical cooling effectiveness such as the homogeneous one, however, periodic porous structures have less weight, which introduces material savings and the use of the laminate's surface.

This work was supported by Ministry of Science and Higher Education in Poland under work No. WZ/WE-IA/2/2020.

Authors: A. Steckiewicz (e-mail: a.steckiewicz@pb.edu.pl), G. Druć (e-mail: gabriela.druc2d@gmail.com), J. M. Stankiewicz (e-mail: j.stankiewicz@doktoranci.pb.edu.pl), Białystok University of Technology, Faculty of Electrical Engineering, Wiejska 45D Str., 15-351 Białystok, Poland.

References

- [1] Y. Liu, "Power electronic packaging: design, assembly process, reliability and modeling," New York, USA: Springer, 2012.
- [2] S. Horton, "PCB-cooling techniques and strategies for IC packages," *Electronic Products*, April 2011. [Online]. Accessed: https://www.electronicproducts.com/Thermal_Management/Heat_Sinks_and_Thermal_Materials/PCB-cooling_techniques_and_strategies_for_IC_packages.aspx.
- [3] P. Górecki, "Radiatory część 3," *Elektronika Praktyczna*, Vol. 5, No. 94, 1994.
- [4] D. Shamvedi, O.J. McCarthy, E. O'Donoghue, C. Danilenkoff, P. O'Leary and R. Raghavendra, "3D Metal printed heat sinks with longitudinally varying lattice structure sizes using direct metal laser sintering," *Virtual and Physical Prototyping*, Vol. 13, No. 4, 2018.

- [5] G. Langer, M. Leitgeb, J. Nicolics, M. Unger, H. Hoschopf and F. Wenzl, "Advanced Thermal Management Solutions on PCBs for High Power Applications," *Journal of Microelectronics and Electronic Packaging*, Vol. 11, No. 3, 2014.
- [6] A.S. Koohbanani, M. Ahmadi and M. Bahrami, "Improving Thermal Performance of Printed Circuit Boards by Thermal VIAs," [in:] *Proc. 43rd Annual Conference of North American Thermal Analysis Society*, Montreal, Canada, 2015.
- [7] N. Kafadarova and A. Andonova, "PCB thermal design improvement through thermal vias," [in:] *Proc. of the 8th WSEAS International Conference on Circuits, Systems, Electronics, Control & Signal Processing (CSECS '09)*, Tenerife, Spain, 2009.
- [8] A.C. Yunus and J.G. Afshin, "Heat and Mass Transfer: Fundamentals and Applications," 5th edition, New York, USA: McGraw-Hill, 2015.
- [9] A. Fan, R. Bonner, S. Sherratt and Y. Sungataek Ju, "An Innovative Passive Cooling Method for High Performance Light-emitting Diodes," [in:] *Proc. 28th IEEE SEMI-THERM Symposium*, March 2012, pp. 319–324.
- [10] W.W. Wits, "Integrated cooling concepts for printed circuit boards," Ph.D. dissertation, Faculty of Engineering Technology (CTW), University of Twente, Enschede, Netherlands, 2008.
- [11] P. Górecki, "Radiatory w sprzęcie elektronicznym," *Elektronika dla Wszystkich*, Vol. 12, No. 99, 1999.
- [12] M. Zareba, "Application of Duhamel's Theorem in the Analysis of the Thermal Field of a Rectangular Busbar," *Journal of Electrical Engineering and Technology*, Vol. 14, No. 1, 2019.
- [13] M. Zareba, "Comparison of heating curves of a rectangular busbar in different conditions of heat abstraction during the short-circuit heating," *Bulletin of the Polish Academy of Sciences. Technical Sciences*, Vol. 66, No. 1, 2018.
- [14] Choroszucho, "Analysis of the influence of the complex structure of clay hollow bricks on the values of electric field intensity by using the FDTD method," *Archives of Electrical Engineering*, Vol. 65, No. 4, 2016.
- [15] K. Siwek and S. Osowski, "Particle swarm optimization in synthesis of electric circuits," [in:] *Proc. 17th International Conference Computational Problems of Electrical Engineering (CPEE)*, Sandomierz, Poland, 2016.
- [16] M. Taya, "A constrained discrete layer model for heat conduction in laminated composites," *Computers & Structures*, Vol. 83, No. 21–22, pp. 1705–1718, 2005.

Chapter 6

Luminance contrast distribution analysis in selected pedestrian crossings configurations

*Damian Tyniecki, Maciej Zajkowski, Łukasz Budzyński
Białystok University of Technology, Faculty of Electrical Engineering*

Dedicated lighting fittings for pedestrian crossings have increased the sense of security. Despite this, accidents often occur at nighttime. The paper contains legal and normative requirements regarding illumination of pedestrian crossings. The results of the calculation of luminance contrast at selected configurations of pedestrian crossings meeting the lighting requirements are shown.

Index terms: lighting design, lighting of roads, lighting of pedestrian crossings, luminance contrast

Introduction

According to EuroStat data [1], in Poland there are 9 fatalities per 100 road accidents, which is the highest number in Europe. This number decreases year by year, but the situation is quite different on Polish pedestrian crossings. From 2012 to 2017, there were 95,000 incidents involving pedestrians, of which 37,000 occurred at pedestrian crossings. Over the years, a concerning increase in the number of injuries and victims in incidents at crossings has been noted. It is therefore justified to install additional lighting fixtures within pedestrian crossings. The article points out that the existing requirements in this area should be adjusted to take into account luminance distribution.

Normative and technical requirements

All important requirements for road lighting are contained in the PN-EN 13201 standard [2]. The first part of this document contains a division into road lighting classes (Table 6.1), while the second part contains the operational requirements for road lighting.

In July 2018, the Ministry of Infrastructure and the National Road Safety Council recommended the use of the following document in designing “Guidelines for organizing safe pedestrian traffic. Guidelines for proper lighting of pedestrian crossings” [3]. An additional PC lighting class was established in the guidelines for dedicated lighting at pedestrian crossings. This solution consists in setting additional lighting fixtures as shown in Figure 6.1.

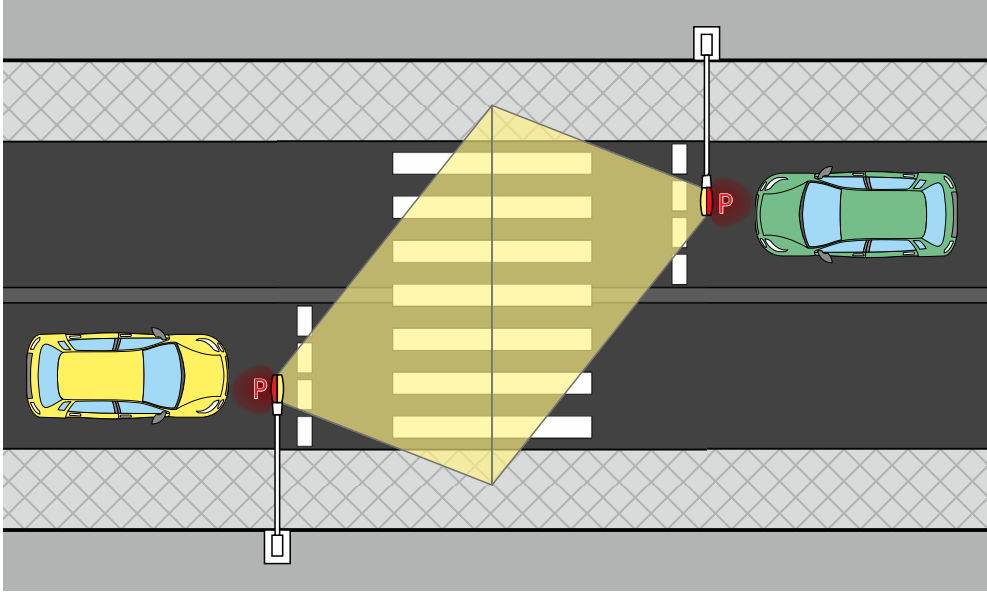


FIGURE 6.1. Example of dedicated pedestrian crossing lighting solution [3]

It is necessary to use lighting fittings with asymmetrical light distributions shown in Figure 6.2. The PC class determines the values of vertical and horizontal lighting intensity within the pedestrian crossing, depending on the lighting class of the road in which the dedicated pedestrian crossing lighting is designed. Tables 6.2 and 6.3 contain the requirements of PC classes for various classes M or C, while Figure 6.3 shows the geometry of measuring the horizontal illuminance E_h and vertical illuminance E_v . The indications of the guidelines [3] coincide with the requirements of PN-EN 13201 and supplement the standard. The General Directorate for National Roads and Motorways, citing the requirements of the Czech Ministry of Transport regarding pedestrian crossing lighting [4], published guidelines for pedestrian crossing lighting [5] which are similar to the indications described below.

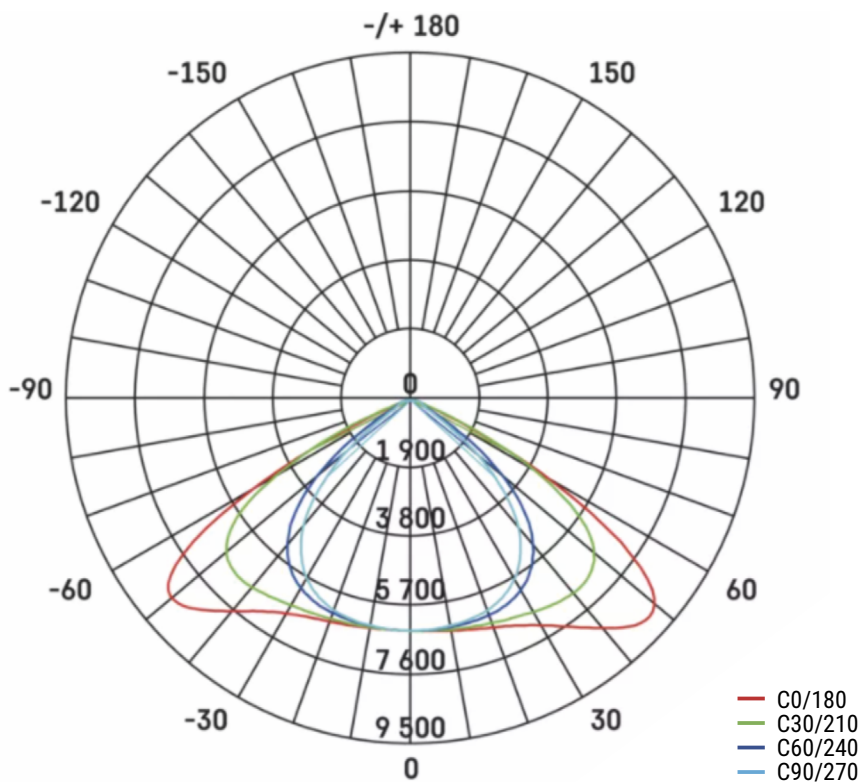


FIGURE 6.2. Example of light distribution of luminaires for pedestrian crossing in the PC class [3]

TABLE 6.1. Road lighting classes and their applications in accordance with PN-EN 13201 [2]

Lighting classes	Class application
M	The main road users are motor vehicle drivers. There may be communication routes. Medium and high speed.
C	Conflict areas (simultaneous occurrence possible): motor vehicles, pedestrians, cyclists; used for areas with variable road geometry or increased collision probability.
P	The main road users are pedestrians and cyclists. Used for lighting sidewalks and bicycle paths. Permitted movement of motor vehicle drivers at low speeds – residential streets.
EV	Additional class: used when the visibility of vertical surfaces must be ensured.
HS	Additional class: pedestrian traffic mainly on pedestrian roads, parking lanes, traffic surfaces lying separately or along the road, housing estate roads.
PC	Additional class used when the main purpose of lighting is to identify people, objects and road surfaces.

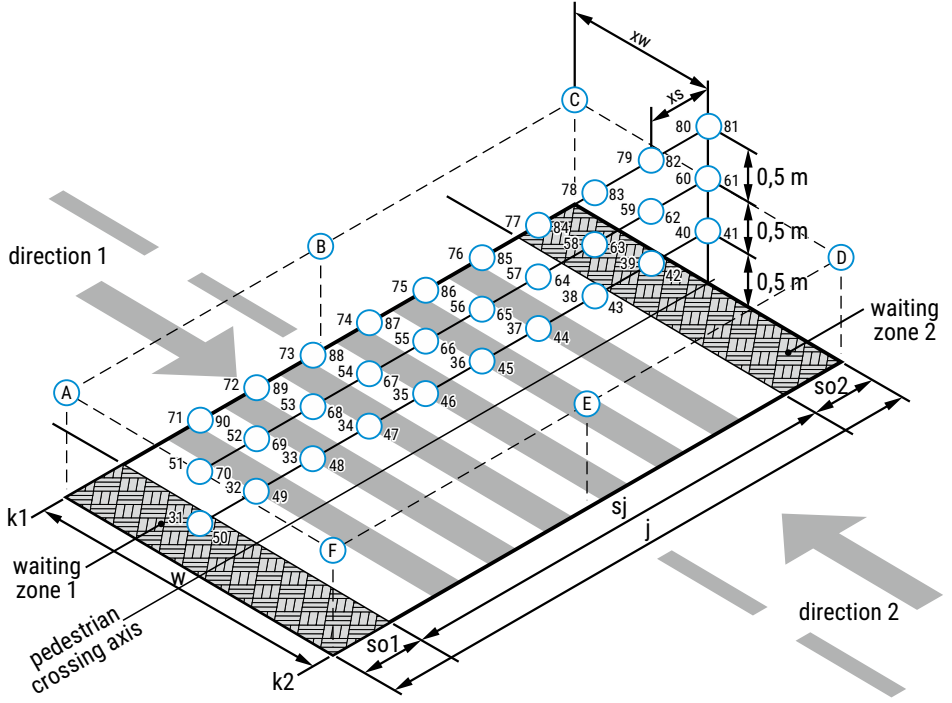
TABLE 6.2. Operating requirements of PC classes for the road in class M [3]

Road lighting		Pedestrian crossing lighting					
Values before and after the pedestrian crossing		PC classes	Measuring planes				Point A, B, C, D, E, F
M classes	L_m		Vertical		Horizontal		
	[cd/m ²]		E_{vm}	U_{0v}	E_{hm}	U_{0h}	$E_{v\min(A,B...)}$
			[lx]	[-]	[lx]	[-]	[lx]
M1	2.00	No need for dedicated solutions					
M2	1.50	PC1	75	0.35	75	0.4	5.0
M3	1.00	PC2	50	0.35	50	0.4	4.0
M4	0.75	PC3	35	0.35	35	0.4	4.0
M5	0.50	PC4	25	0.35	25	0.4	3.0
M6	0.30	PC5	15	0.35	15	0.4	2.0

TABLE 6.3. Operating requirements of PC classes for the road in class C [3]

Road lighting		Pedestrian crossing lighting					
Values before and after the pedestrian crossing		PC classes	Measuring planes				Point A, B, C, D, E, F
C classes	E_m		Vertical		Horizontal		
	[lx]		E_{vm}	U_{0v}	E_{hm}	U_{0h}	$E_{v\min}$
			[lx]	[-]	[lx]	[-]	[lx]
C0	50	No need for dedicated solutions					
C1	30	PC1	75	0.35	75	0.4	5.0
C2	20	PC2	50	0.35	50	0.4	4.0
C3	15	PC3	35	0.35	35	0.4	4.0
C4	10	PC4	25	0.35	25	0.4	3.0
C5	7.5	PC5	15	0.35	15	0.4	2.0

a)



b)

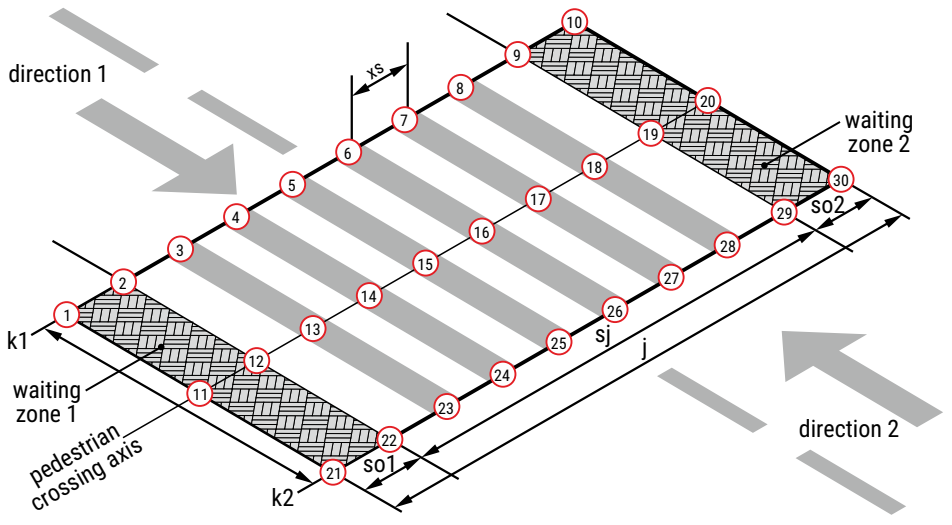


FIGURE 6.3. Geometry of illuminance measurement: a) vertical, b) horizontal

luminance in lighting of pedestrian crossings

A common feature of the presented requirements and guidelines for lighting pedestrian crossings are only the quantitative and qualitative parameters of lighting intensity. There is no analysis of the luminance of objects (mainly pedestrian luminance) that may be at the crossings. Luminance, or more precisely the luminance contrast C between the observed object and the background (1) allows to detect objects [6]:

$$C = \frac{L_o - L_T}{L_T} \rightarrow L_o = \frac{\rho \cdot E_v}{\pi} \rightarrow C = \frac{\left(\frac{\rho \cdot E_v}{\pi} - L_T \right)}{L_T}, \quad (6.1)$$

where:

- C – luminance contrast,
- ρ – total reflection coefficient of the objects,
- E_v – vertical illuminance [lx],
- L_o – object luminance [cd/m^2],
- L_T – background luminance [cd/m^2].



FIGURE 6.4. Measurement of the luminance distribution of the observed environment [6]

When analyzing the results of the measurement of the luminance distribution visible in Figure 6.4, it can be stated, that there are situations when it is difficult or even impossible to detect the object despite lighting the area according to the requirements [2, 5]. In the event that the luminance contrast C is close to one, there is a high probability of not noticing the object on the road. Obtaining sufficiently high luminance contrast values across the entire width of the pedestrian crossing requires a different view of the lighting problem. The situation can be solved by using a lighting system that could dynamically modify the distribution of light using for this purpose optical systems with advanced structures [7, 8].

Numerical calculations in DIALux software

In order to check in which lighting situations the above described phenomenon may occur, simulation calculations were performed using DIALux software. Road lighting was designed (Fig. 6.5) along with the infrastructure with parameters included in Table 6.4. Various configurations of the location of the pedestrian crossing with respect to the road lighting poles and the possibility of pedestrian movement in the axis of the crossing and at its edges were considered. The pedestrian crossing was considered with the location:

- directly behind the lighting pole,
- between lighting columns,
- directly in front of the lighting column.



FIGURE 6.5. View of the road lighting project in the DIALux software

TABLE 6.4. Parameters of the road designed in the DIALux software

Parameter	Value
Road class according to PN-EN 13201	M3
Average road luminance	$L_m = 1.00 \text{ [cd/m}^2\text{]}$
Uniformity	$U_0 \geq 0.40 \quad U_l \geq 0.60$
Road width	7 [m]
Road surface	R3, $q_0=0.07$
f_{TI}	$\leq 15\%$

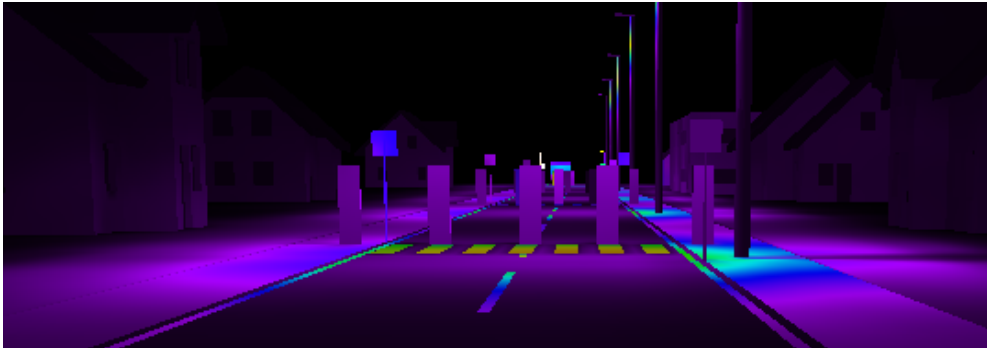


FIGURE 6.6. Luminance distribution from the driver's perspective

In the DIALux software, pedestrians are represented as a cuboid for which the value of the coefficient of reflection of the surface of the side walls was changed successively by 0.1; 0.4; 0.8, which in practice may mean a different color of clothing for pedestrians. Based on the results of the simulation, the average luminance of the cuboid wall seen from the driver's side was calculated, and the background luminance value to determine the luminance contrast. In each case, the illuminance value of the silhouette of the pedestrian model did not change.

The analysis of the results leads to the conclusion that for different values of the reflection coefficient, the luminance contrast value can differ significantly from 1. In this case, there is an insufficient luminance contrast difference, which can lead to a distorted perception of the object on the road. The contrast itself should be analyzed as an absolute value calculated according to the formula (1). Luminance contrast C , both negative and positive, is only acceptable in selected pedestrian configurations relative to pedestrian crossing positions [9].

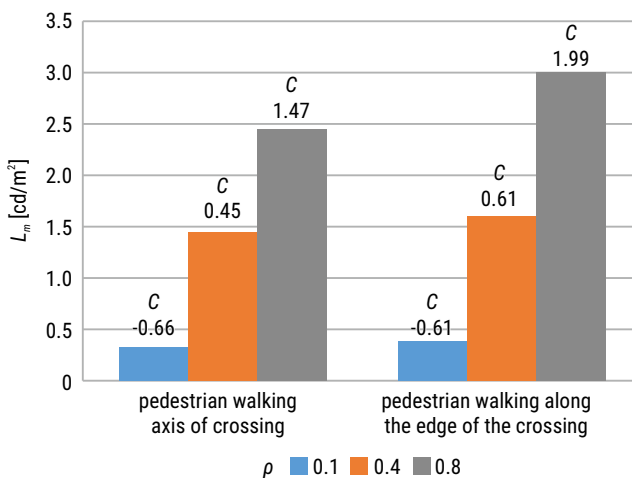


FIGURE 6.7. Value of the average luminance of the pedestrian model and calculated luminance contrasts, pedestrian crossing directly behind the lighting column

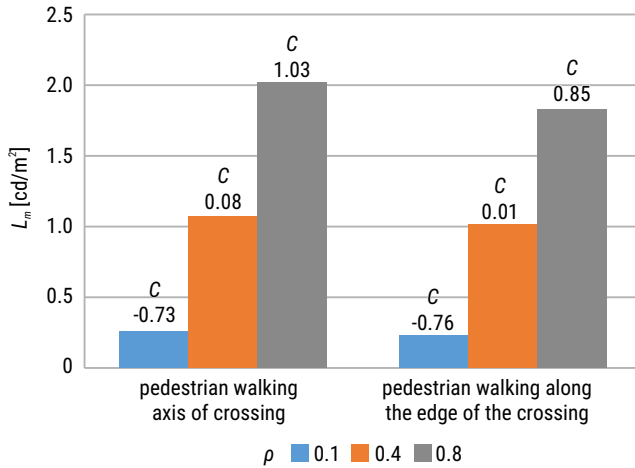


FIGURE 6.8. The value of the average luminance of the pedestrian model and calculated luminance contrasts, pedestrian crossing between lighting columns.

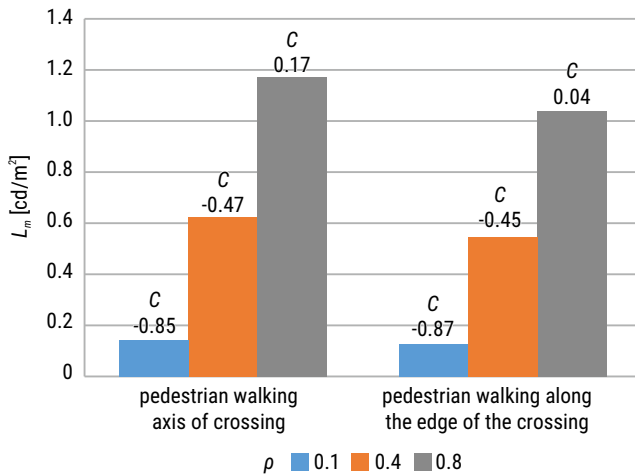


FIGURE 6.9. The value of the average luminance of the pedestrian model and the calculated luminance contrasts, pedestrian crossing in front of the lighting column

In the considered case, a dedicated pedestrian crossing lighting system recommended by regulatory requirements was also analyzed [2, 3, 5]. Figure 6.10 presents an increase in the luminance contrast value using a dedicated lighting system, however, when the pedestrian reflection coefficient is 0.1, the contrast value is $C \leq 1$. This situation proves that the requirements of the standards, taking into account only the distribution of illuminance, may be insufficient and require an additional assessment of the luminance arrangement.

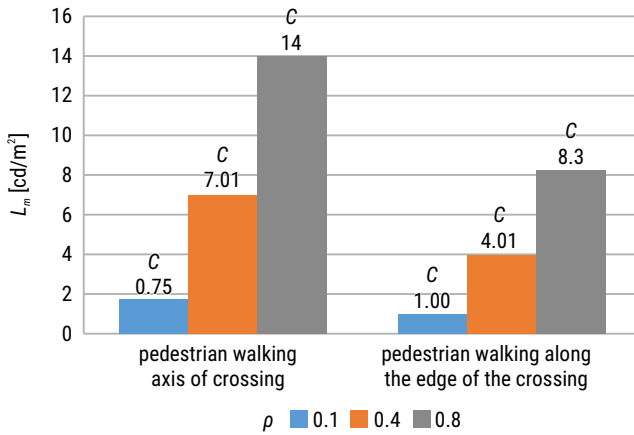


FIGURE 6.10. The value of the average luminance of the pedestrian model and calculated luminance contrasts, pedestrian crossing with a dedicated lighting system

Conclusion

The use of road lighting is an obligation arising from standards and legal provisions. Current requirements allow for the use of dedicated lighting systems for pedestrian crossings to see the pedestrian as early as possible. Specific values of illumination within the pedestrian crossing must be met, depending on the lighting class of the road on which the crossing is located. Unfortunately, the presented analyses may face the problem of the correct process of visibility on the road. The current requirements do not address the aspect of luminance contrast in relation to pedestrian crossings. High luminance contrast ensures the ability to correctly observe the field of view. In extremely unfavorable lighting conditions it may happen that the luminance of the surroundings and the pedestrian luminance are similar, which may result in an accident. Adverse conditions do not necessarily mean an unlit road. It is therefore necessary to create a lighting system that could analyze the luminance contrast within the pedestrian crossing. In addition, it should allow for dynamic change in light beam distribution. This feature can allow for proper lighting of pedestrians walking not only within the crossing axis, but also in any of its areas.

The article was financed as part of the work S/WE 3/2018.

Authors: D. Tyniecki (e-mail: d.tyniecki@pb.edu.pl), M. Zajkowski (e-mail: m.zajkowski@pb.edu.pl), Ł. Budzyński (e-mail: l.budzynski@pb.edu.pl), Białystok University of Technology, Faculty of Electrical Engineering, Wiejska 45D Str., 15-351 Białystok, Poland.

References

- [1] System ewidencji wypadków i kolizji 2018.
- [2] PN-EN 13201-1-5 Oświetlenie dróg, PKN, Warszawa 2016.
- [3] K. Jamroz, P. Tomczuk, T. Mackun, M. Chrzanowicz, “Wytyczne organizacji bezpiecznego ruchu pieszych. Wytyczne prawidłowego oświetlenia przejść dla pieszych,” Ministerstwo Infrastruktury, Warszawa 2017.
- [4] Ministerstvo Dopravy, “Osvětlení pozemních komunikací,” Praga 2015
- [5] Generalna Dyrekcja Dróg Krajowych i Autostrad, “ Wytyczne oświetlania przejść dla pieszych realizowanych przez GDDKiA”, Poznań 2018.
- [6] P. Tomczuk, “Zasady oświetlania przejść dla pieszych,” III Ogólnopolskie forum specjalistyczne Organizacja Ruchu, Kraków 2016.
- [7] M. Zajkowski, Ł. Budzyński, D. Tyniecki, “Luminous flux ring mixer,” [in]: *VI. IEEE Lighting Conference of the Visegrad Countries: LUMEN V4: Proceedings* [online], 2016, pp. 201–204.
- [8] J. Kuszniar, M. Zajkowski, Ł. Budzyński, D. Tyniecki, “Ring optical mixer for LED with truncated surfaces,” *Optical Fibres and Their Applications 2017, Proceedings of SPIE*, Vol. 10325, p. 8.
- [9] P. Tomczuk, “Ocena jakości oświetlenia sylwetki pieszego na przejściu dla pieszych,” *Prace Naukowe Politechniki Warszawskiej, Transport*, Vol. 87, 2012.

Chapter 7

Low voltage electrical installations – energy efficiency functional aspects

Honorata Sierocka, Marcin A. Sulkowski
Bialystok University of Technology, Faculty of Electrical Engineering

This article is based on IEC 60364-8-1 Energy Efficiency standard. It presents the most important aspects contained in the standard. It describes the procedures for increasing the energy efficiency of existing and new, still being designed, electrical installations. The most important aspects that the designer should pay attention to are presented, concerning the design, construction, operation and verification of all types of low voltage electrical installations. Attention is drawn to the necessity of analyzing the location of elements of installations and receivers already at the stage of designing the structure. The barycentric method of placing loads in the electrical installation is discussed and an example of correct and incorrect placement of the transformer in relation to the bar center is shown. The method of determining the load curve of the building and making measurements necessary for this purpose is described and the possibility of using synthetic load curves is mentioned. Part of the article is also devoted to the selection of appropriate meters for making such measurements and the influence of external factors on their accuracy. The benefits of increasing energy efficiency for companies and the environment are described as well. The article also shows how to manage energy efficiency and the obligations it involves.

Index terms: efficiency classes, electrical installations, energy efficiency, energy management systems

Introduction

The optimization of electrical energy usage can be facilitated by appropriate design and installation considerations. It is important that this can be done in existing electrical installations in buildings and in new installations. An electrical installation can provide the required level of service and safety for the lowest electrical consumption. The design of the whole installation has therefore to take into account inputs from users, suppliers and utilities.

Additional requirements, measures and recommendations for the design, erection, operation and verification of all types of low voltage electrical installations including local production and storage of energy for optimizing the overall efficient use of electricity are included in IEC 60364-8-1: Energy efficiency. According to the definition contained in the standard, electrical energy efficiency EEE is a systemic approach to optimizing the efficiency of electricity usage. Energy efficiency improvement measures take into account:

- both the consumption (kWh) and price of electricity,
- technology,
- environmental impact.

The energy efficiency of an electrical installation is rated into one of the following classes from lower efficiency to higher efficiency: EE0, EE1, EE2, EE3, EE4, and EE5 (Fig. 7.1).

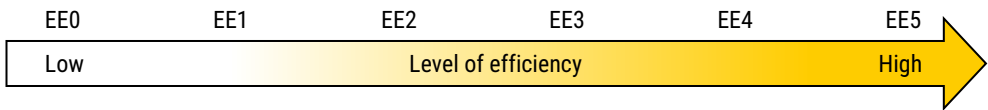


FIGURE 7.1. Level of efficiency of the electrical installation efficiency classes

Design principles

The basic issue to keep in mind when applying all energy efficiency measures is the full electrical availability of the customer and/or service and the level of performance required by the user. However, the electrical installation should have provisions to change the arrangements for the management of energy efficiency by the user, for example when they need to increase the room temperature when they are ill.

The design principles of IEC 60364-8-1 take into account the following aspects:

- load energy profile (active and reactive);
- availability of local generation (PV, wind turbine, generator, etc.) and storage;
- reduction of energy losses in the electrical installation;
- the arrangement of the circuits with regard of energy efficiency;
- the customer's power use distribution over time;
- tariff structure offered by the supplier of the electrical energy.

The assessment of the installation should be carried out preferably by measurement, but a calculation -based assessment is also acceptable.

The intensity of inspections of the electrical installation should be determined taking into account its type, equipment, use and operation, factors and external influences to which it is exposed.

It is recommended that the maximum interval for follow-up assessment does not exceed:

- five years for commercial installations;
- three years for industrial and infrastructure ones.

After assessing the installation, an action plan should be established to improve its energy efficiency.

If the analysis concerned a new installation and showed a lower than required electrical efficiency class, actions should be taken to correct these discrepancies.

If this was a periodic assessment of an existing installation and showed too low a level of energy efficiency in relation to the required value, then an action plan is needed to provide the required or desired energy efficiency class.

Designing requirements and recommendations

Designing electrical installation it is worth to define its load energy profile. This can be done on the basis of existing similar synthetic profiles (typical load energy curves) derived from loads or load groups. If measurements or synthetic profiles are not available, it is possible to create a load energy profile based on the main loads and their expected operating time.

Because of the energy efficiency and specific features requiring a specific implementation methodology, four basic sectors of electrical installations can be identified:

- residential installations;
- commercial installations;
- industrial installations;
- infrastructure installations.

It is worthwhile for people designing an electrical installation to be able to assign it to one of the above sectors.

Another important point is to determine the position of the transformer and the switchboard using the barycenter method. In looking for the best place to locate them, it is important to pay attention to the use, construction and availability of space in the building. If it is possible, it should be discussed with the owner of the building and the designer before the construction process starts.

Placing the main loads as close as possible to the main switchboards and transformers (according to the building's limitations) will help to reduce wiring losses to the minimum. Thanks to the barycenter method we can determine load distribution (uniform or localized).

The building layout in Fig. 2 shows the building topology. Without using the barycenter tool, the switchboard rooms were originally located in position 1. By calculation of the total load barycenter (purple circle with number 2), the result shows clearly that position 2 is much closer to receptors of high power (utilities) and consequently will improve cable utilization and thereby reduce cable losses.

The next issue that needs to be considered in order to find the optimal solution for the transformer is:

- the optimum number and location of HV/LV substations;
- the working point of transformer;
- the efficiency of the transformer;
- the load energy profile.

The required power, building area and load distribution determine the number of HV/LV substations and their distribution, which affects the length and cross-section of the cables. Having the knowledge of the barycenter location, we can decide whether to choose one or more HV/LV substations.

With a transformer load of 30% to 50% of its rated power the losses in iron and copper are equal. In such a situation we have to deal with the maximum efficiency of the transformer.

On this basis we should choose the point of work of the transformer to ensure the highest energy efficiency of the installation.

A properly selected transformer has a huge impact on the energy efficiency of the entire installation. By choosing a transformer with the highest energy efficiency class, we can make a lot of savings, even though it involves higher initial costs. The cost of a more expensive transformer with a higher energy efficiency class pays for itself in a few years, which in comparison with its whole life is relatively short. More information about the energy efficiency of transformers, installation details and limitations and payback time can be found in the information from manufacturers.

It is also possible to improve energy efficiency through the use of renewable energy sources and related energy storage. We can use warehouses or discharge energy to the grid, which improves the efficiency of local production.

Another aspect that has an impact on the energy efficiency of the installation is the selection of the cable cross-section. Increasing the cross-section of cables in distribution circuits and in end circuits (supplying high power loads) reduces voltage drops. The selection of the cross-section of conductors should be based on the economic and technical analysis. Selecting a cable, one should take into account not only the cost of the cable, but also its installation and assembly, as well as energy losses in the cable during its expected lifetime.

The method that allows to calculate such cost is included in IEC 60287-3-2.

Another important issue is the improvement of power factor and the reduction of harmonic currents.

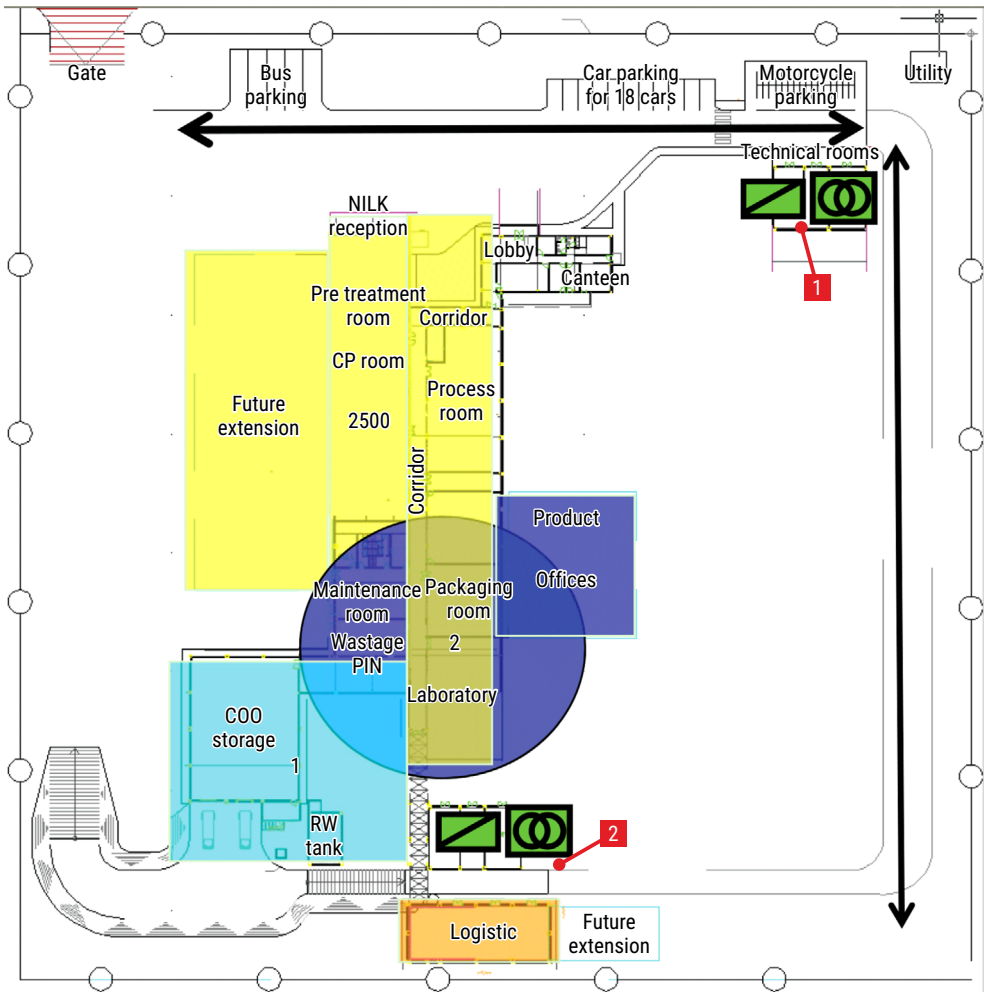


FIGURE 7.2. Example of location of the barycenter in an industrial building

The power factor can be reduced by reducing reactive power consumption. Reducing it at a load level reduces heat loss in the power side wiring. The power factor can be improved centrally or at a load level.

The reduction of harmonics at a load level is possible by selecting suitable consumers free of harmonics. This can also be done by:

- using harmonic filters at respective load circuits;
- increasing the cross-sectional area of the conductors;
- using methods that produce less harmonics, like Sinusoidal Pulse Width Modulation (SPWM), in the renewable energy resources' inverters connected to the Point Of Connection (POC).

Energy efficiency and load management system

An energy efficiency and load management system controls the usage of the consumed energy, taking into account the loads, local production and storage and user requirements (Fig.3).

The basis for determining and evaluating the efficiency of a building is the performance of measurements. The measurement of electrical parameters is required to determine electricity consumption and has to be completed by the measurement of forcing parameters, such as:

- presence of people;
- temperature;
- quality of air (e.g. CO₂);
- day light;
- operating time;
- cost of energy.

Another very important aspect is the selection of an appropriate device. Thanks to this, the installation user knows what the energy consumption is. In buildings such as apartments, stores or offices the highest precision of measurement is necessary at the origin of the installation. It is this measurement that is used for billing and on its base we pay the bills, and also thanks to such measurement we can assess the energy efficiency of the whole installation. These measurements, as well as the measurements of power quality in the connector can be part of the process of evaluating the energy efficiency of the installation.

It is also important to remember to use the measuring devices properly in according to their purpose and location in the installation. Where applicable, measurements and monitoring shall be carried out in each phase.

The standard IEC 61557-12 defines power metering and monitoring device (PMD) classification with minimal required functions according to its application:

- PMD-1: Energy efficiency: energy usage analysis for energy efficiency assessment;
- PMD-2: Basic power monitoring: power monitoring for electrical energy distribution monitoring and control within the installation;
- PMD-3: Advanced power monitoring and network performance: advanced power monitoring and network performance monitoring.

It is very important that all activities related to the energy management system with regard to energy efficiency do not interfere with the communication ensuring safety, control or operation of the equipment or devices.

Information on expected loads can also be found from historical data. This can be very helpful. According to IEC 62974-1, a communication system between all required and predicted data must be provided.

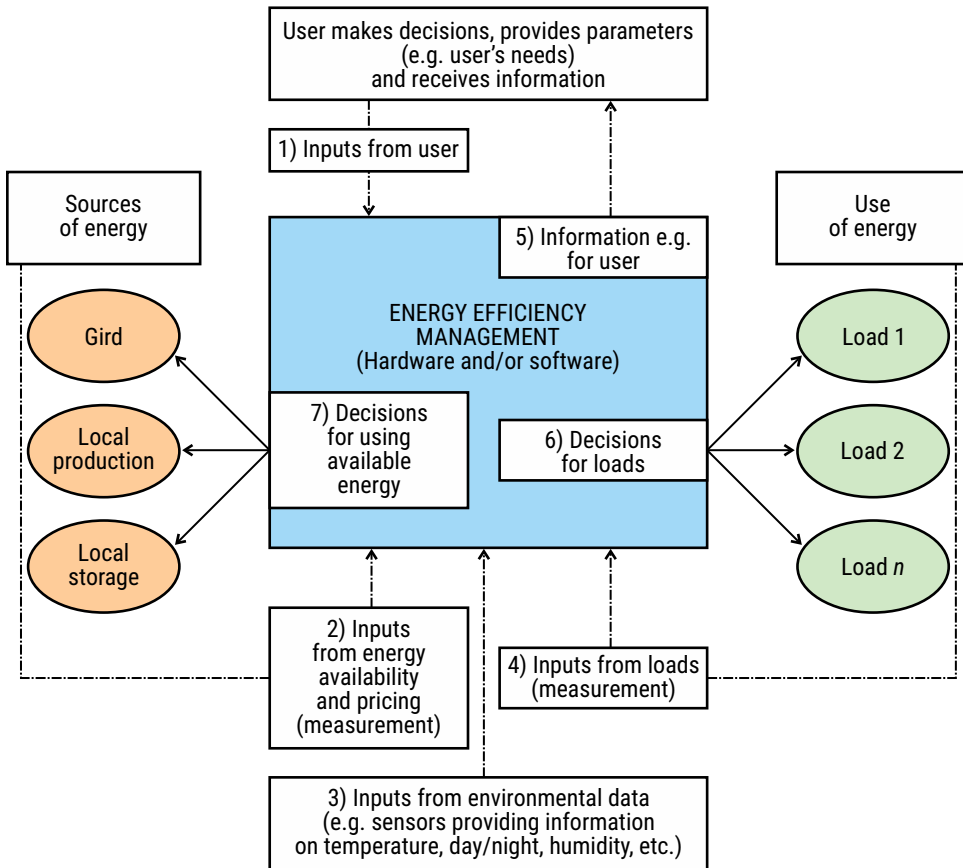


FIGURE 7.3. Energy efficiency and load management system overview.

The main parameter that defines energy efficiency is active energy (kWh). The complete system for measuring electrical energy is made up of measuring devices associated with external current and/or voltage sensors. The performance class of the system depends on the sensor class and on the performance class of the meter. The class shall be selected so that it is equal or lower than the meter or PMD class.

The sensors should also be selected based on the maximum current in the circuit and the minimum current that needs to be monitored, they must also be selected in accordance with IEC 61869-2.

Choosing the sensors, one should also remember about possible external influences. Deviations from the accuracy of measurements can be influenced by factors such as temperature. The factors that may generate such deviations are specified in IEC 61557-12. If the sensor complies with the measurement class defined in these standards, it meets the requirements for maximum deviations under these values.

Electrical energy management system (EEMS)

The energy efficiency management system manages the entire electrical installation, including loads, local production and storage. It can monitor the electrical installation manually (in the simplest cases) or automatically (in most cases) in order to optimize the total cost and consumption of the system, taking into account user requirements and input parameters from the network, local electricity generation and storage, loads, sensors, forecasts, etc.

The Electrical Energy Management System includes:

- measurement (e.g. energy consumption) and mesh monitoring;
- control;
- energy quality;
- reporting;
- warnings: status of monitoring devices;
- tariff management, if any;
- data security;
- display function for users and/or public awareness.

It is possible to maintain and increase the efficiency of the installation by implementing appropriate energy efficiency measures, active or passive. This requires an integrated approach to the electrical installation and the consideration of all the ways the installation operates. The energy efficiency claim process and responsibilities are presented in Table 7.1.

TABLE 7.1. Process for electrical energy efficiency management and responsibilities

Action	Details	Generally performed by
Energy audit and measure	<ul style="list-style-type: none"> • Analysis of data from installed power metering and monitoring devices and/or non installed measurement equipment 	Auditor or energy manager
Set the basics	<ul style="list-style-type: none"> • Initial equipment selection, higher efficiency consumption devices • Initial service settings, etc. 	Designer and/or installer
Optimize	<ul style="list-style-type: none"> • HVAC control • Lighting control • Variable speed drives • Automatic power factor correction, etc. 	Installer/tenant or user, energy manager
Monitor, maintain the performance	<ul style="list-style-type: none"> • Power metering and monitoring devices installation • Monitoring services • Electrical energy efficiency analysis, software, etc. 	Energy manager/tenant or user
Control, improve	<ul style="list-style-type: none"> • Verification, maintenance, etc. 	Energy manager/tenant or user

Measurement, optimization and monitoring are important for energy efficiency:

- a) Audit of energy consumption by means of measures that will provide an indication of the situation and the main routes leading to savings (where the main consumptions are located, what is their pattern). An initial assessment can be carried out based on a set of measurements for the different meshes within the installation and a comparison with the comparative energy consumption criteria established for a combination of appliances within the network or installation. Although this may help to identify areas that can be analyzed in more detail, determining whether an installation is efficient will depend on more precise measurements and an evaluation of parts of the installation compared to the overall energy consumption.
- b) Optimization through continuous automation or control. As already highlighted, everything that consumes energy needs to be actively addressed in order to achieve sustainable benefits. Continuous control is crucial to achieve maximum efficiency.
- c) Monitoring, maintenance and improvement of the electrical installation. As targets are set for a long period of time, energy efficiency programs represent a lasting improvement over time.

Conclusion

The energy efficiency of the installation requires a lot of work on the part of the designer. The above standard definitely helps to determine the most important elements of the installation and how they will affect its energy efficiency. An important effect of these procedures is to reduce the negative impact on the environment.

By the maximization of energy efficiency we reduce the consumption of energy resources. Thanks to this, companies or businesses operate more efficiently and economically, and become more competitive. Moreover, thanks to such measures we can contribute to the reduction of electricity imports from other countries and aspire to energy independence.

From the presented contents it follows that when planning an electrical installation, its location and the chosen equipment, it is worth paying higher costs of such an installation in return for better energy efficiency and reduction of operating costs in the future.

Continuous improvement is also important because it is essential to ensure energy efficiency. In the last stages the differences decrease due to the elimination of the most significant losses. Thanks to such measures, the electrical installation generates the smallest possible losses.

Authors: H. Sierocka (e-mail: h.sierocka@pb.edu.pl), M. A. Sulkowski (e-mail: m.sulkowski@pb.edu.pl), Białystok University of Technology, Faculty of Electrical Engineering, Wiejska 45D Str., 15-351 Białystok, Poland.

References

- [1] IEC 60364-8-1:2018 Energy efficiency.
- [2] IEC 61869-2:2012 Instrument transformers – Part 2: Additional requirements for current transformers.
- [3] IEC 62974-1:2017 Monitoring and measuring systems used for data collection, gathering and analysis – Part 1: Device requirements.
- [4] IEC 60287-3-2:2012 Electric cables – Calculation of the current rating – Part 3–2: Sections on operating conditions – Economic optimization of power cable size.
- [5] IEC 61557-12:2018 Electrical safety in low voltage distribution systems up to 1 000 V AC and 1 500 V DC – Equipment for testing, measuring or monitoring of protective measures – Part 12: Power metering and monitoring devices (PMD).

Chapter 8

The impact of electric energy receivers used in modern households on energy efficiency in the low-voltage network

Kacper Szadkowski, Grzegorz Hołdyński
Białystok University of Technology, Faculty of Electrical Engineering

This paper deals with the issues of power losses in low-voltage supply networks caused by the impact of electricity loads in modern households. These power losses have a direct impact on energy efficiency. The authors analyze the influence of reactive power and higher harmonics and base their considerations based on the studies which include typical modern household receivers. Based on the measurement results for single receivers and simple formulas, approximate losses in low-voltage networks are presented. The final results show the need for further analysis of the topic, preceded by a more complex computer simulation.

Index terms: energy efficiency, higher harmonics, household receivers, reactive power

Introduction

A typical home user of electrical equipment when choosing a receiver, e.g. a light source, pays attention to active power consumption. This is reasonable because this parameter will affect the amount on the electricity bill. The fact is that active power consumption of typical household appliances has decreased. A good example is the transition from incandescent light sources (e.g. a traditional light bulb) to LED sources, where active power consumption has been reduced many times while maintaining a similar luminous flux value. However, the use of LED sources and an increasing number of electronic receivers that use impulse power supplies bring an increase in reactive power consumption and deformation power, which results from the deformed nature of the current. This paper presents the possible effects of using electricity receivers that are present in the modern household, which brings the issue of energy efficiency.

Increase in active power losses caused by the flow of reactive power

To understand the mechanism of increase in active power caused by the flow of reactive power, considerations should start with the relationship between active, reactive power and apparent power. These relationships are presented in equation 8.1 and Figure 8.1 [1]:

$$S = \sqrt{P^2 + Q^2}, \tag{8.1}$$

where:

- S – apparent power,
- P – active power,
- Q – reactive power.

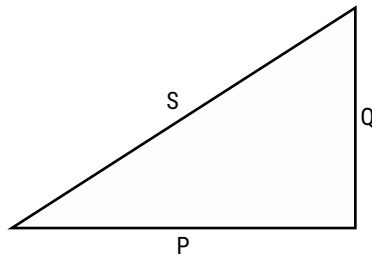


FIGURE 8.1. Power triangle

Analyzing equation (1) and Figure 8.1, it can be observed that an increase of active power P or reactive power Q causes an increase of apparent power S . The value of apparent power defines the RMS value of the current flowing through the grid according to the relation form equation (2):

$$I = \frac{S}{U}, \tag{8.2}$$

where:

- I – RMS value of current intensity,
- U – RMS value of voltage.

Active power losses resulting from the presence of resistance of the three-phase low-voltage network can be calculated based on equation (8.3) [2, 3, 4, 5, 6, 7]:

$$\Delta P = 3 \cdot I^2 R = \frac{P^2 + Q^2}{U^2} \cdot R = \frac{P^2 \cdot (1 + \text{tg}^2 \varphi)}{U^2} \cdot R, \tag{8.3}$$

where:

- ΔP – active power losses,
- R – resistance of single-phase wire,
- $\text{tg} \varphi$ – power factor (tangent).

Here it can be seen that an increase in reactive power will result in an increase in apparent power and thus in a value of effective current. A loss of active power in a grid resistance is proportional to the square of this value. Equation (3) also shows the dependance of these losses on the power factor in the form of tangents. The formula (8.4) [8] and Figure 8.2 show a relative increase of active power losses based on the power factor in the form of cosine.

$$\delta\Delta P_Q = \operatorname{tg}^2\varphi \cdot 100\% = \left(\frac{1}{\cos^2\varphi} - 1 \right) \cdot 100\%, \quad (8.4)$$

where:

$\delta\Delta P$ – relative increase of active power losses caused by reactive power flow,
 $\cos\varphi$ – power factor (cosine).

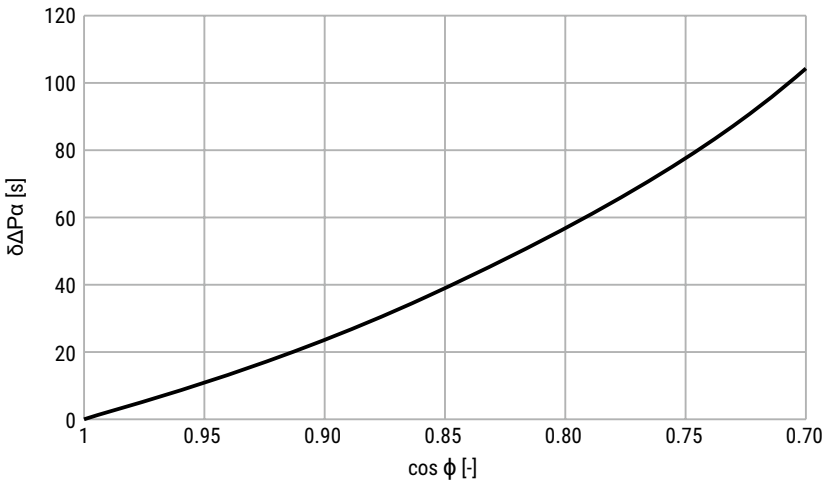


FIGURE 8.2. Characteristics of relative increase of active power loss as a function of power factor values

With a power factor of 0.82, active power losses increase by 50% compared to no reactive power state, and with a value of 0.71 – an increase by 100%.

In addition to the active power losses in the resistance of household power supply cables, there is also an increase in the load active power losses in the power supply transformer, resulting from the flow of the current with a higher RMS value through transformer windings which, like power supply cables, have their resistance.

Increase in active power losses caused by the flow of distorted current

A. Increase in active power losses caused by increase in apparent power

The effects of reactive power flow associated with an increase in RMS value of the current become more pronounced when dealing with distorted current consumption. The power triangle in Figure 8.1 is then supplemented for deformation power, which modifies the mentioned figure to the spatial form of the so-called power cuboid [9] presented in Figure 8.3.

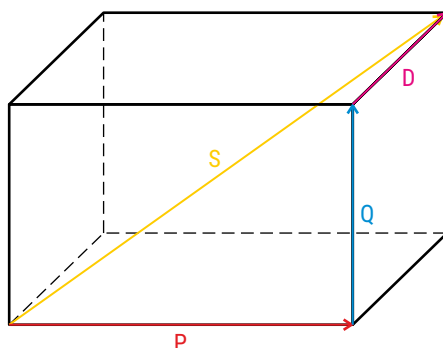


FIGURE 8.3. Power cuboid

The apparent power can then be determined by means of formula (8.5):

$$S = \sqrt{P^2 + Q^2 + D^2}, \quad (8.5)$$

where:

D – deformation power.

The mechanism of increasing active power losses is analogous to the previous point of the paper.

B. Impact of higher harmonics on wire losses

When analyzing the impact of higher harmonics, two points should be noted:

- skin effect,
- summation of higher harmonics of every third order in a neutral wire N or protective earth neutral wire PEN.

A skin effect is an increase in the resistance of a wire for high frequency currents. A higher frequency causes that the flow is not uniform throughout the cross-section. The density of the current in the middle of the cross-section decreases, which makes it practically inactive and the density in the part distant from the middle

of the cross section increases. The useful cross-section of the wire is reduced, which results in the resistance increase depending on the height of frequency of the flowing current according to formula 8.6 [10, 11]:

$$R_h = \delta_{Rh} \cdot R_{DC} \approx \sqrt{h} \cdot R_{DC}, \quad (8.6)$$

where:

- R_h – wire resistance for h-th harmonic flow,
- δ_{Rh} – wire resistance gain factor for h-th harmonic flow,
- R_{DC} – wire resistance for DC current,
- h – harmonic order.

An increase in resistance for a given current RMS value will lead to an increase in active power losses in the wires where the current containing higher harmonics will flow, as shown by formula 8.7 [10]:

$$\Delta P = \sum_{h=1}^{\infty} (R_h \cdot I_h^2), \quad (8.7)$$

where:

- I_h – RMS value of current intensity of h-th harmonic.

When considering a power supply consisting of three-phase wires and a neutral wire, formula (8.7) can be modified to (8.8) [11]:

$$\Delta P = R_{DC} \cdot \sum_{h=1}^{\infty} \left[\sqrt{h} \cdot (I_{hL1}^2 + I_{hL2}^2 + I_{hL3}^2 + I_{hN}^2) \right], \quad (8.8)$$

where:

- $I_{hL1,L2,L3,N}$ – RMS value of current intensity of h-th harmonic in individual wires.

Based on the fact that active power losses, in the absence of higher harmonics, are caused by the first harmonic, it is possible to present a relative increase of active power losses caused by the flow of distorted current by means of relation (8.9) [11]:

$$\delta \Delta P = \frac{\sum_{h=2}^{\infty} \left[\sqrt{h} \cdot (I_{hL1}^2 + I_{hL2}^2 + I_{hL3}^2 + I_{hN}^2) \right]}{I_{1L1}^2 + I_{1L2}^2 + I_{1L3}^2 + I_{1N}^2}, \quad (8.9)$$

where:

- $\delta \Delta P$ – relative increase of active power losses caused by the flow of distorted current.

Focusing on a single phase, a relative increase in active power losses in a single phase can be presented using formula (8.10):

$$\delta \Delta P = \frac{\sum_{h=2}^{\infty} (\sqrt{h} \cdot I_{hL1}^2)}{I_{1L1}^2}. \quad (8.10)$$

Another phenomenon that increases the losses of active power is the accumulation of h-th higher harmonics of the current in the N or PEN wire. They form symmetrical systems of the zero order [12], which makes it possible that in the situation when identical single-phase receivers are connected to three different phases, in a neutral wire e.g. a third harmonic with the amplitude being the sum of the harmonic amplitudes of the third harmonics of individual receivers will be present, as shown by formula (8.11) and Figure 8.4 [13]. Such a situation would not occur if the mentioned receivers were linear. By combining the summation of the mentioned harmonics and the skin effect, it can be observed that an increase of active power losses in the N or PEN wire can be significant.

$$I_N = I_R + I_S + I_T = \sum_{n=1}^{\infty} \left[I_{R(3n)} + I_{S(3n)} + I_{T(3n)} \right], \tag{8.11}$$

where:

- n – natural number,
- $I_{R(3n)}$ – RMS value of current intensity of 3n-th harmonic in R-phase wire,
- $I_{S(3n)}$ – RMS value of current intensity of 3n-th harmonic in S-phase wire,
- $I_{T(3n)}$ – RMS value of current intensity of 3n-th harmonic in T-phase wire.

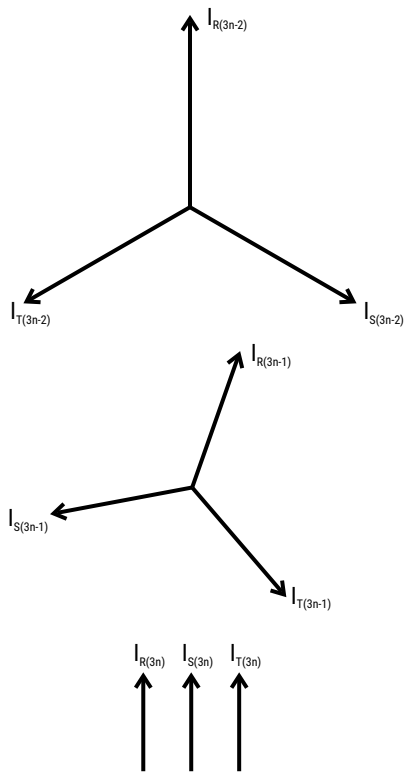


FIGURE 8.4. Relationship between successive harmonics in three phases

C. Impact of higher harmonics on transformer losses

Just like in the wires, one of the reasons for the increase in active power losses in a transformer is the skin effect, which increases the resistance of its windings. Additionally, the presence of higher harmonics causes an increase in core losses from eddy currents and hysteresis losses [14].

The influence of eddy currents on the losses of active power can be presented by means of the K factor described in relation (8.12), which refers to the ratio of these losses in the course of a deformed current flow to losses during sinusoidal flow [15].

$$K = \frac{1}{I_{rms}} \sum_{h=1}^{\infty} [I_h^2 \cdot h^2], \quad (8.12)$$

where:

I_{rms} – RMS value of current intensity

ANALYSIS OF CURRENTS AND POWER RECEIVED BY SELECTED HOUSEHOLD RECEIVERS

A. Measurement results

To make the measurements, the Sonel PQM-701 power quality meter was applied. For this purpose, the measuring system with the diagram shown in Figure 8.5 was used [13, 16].

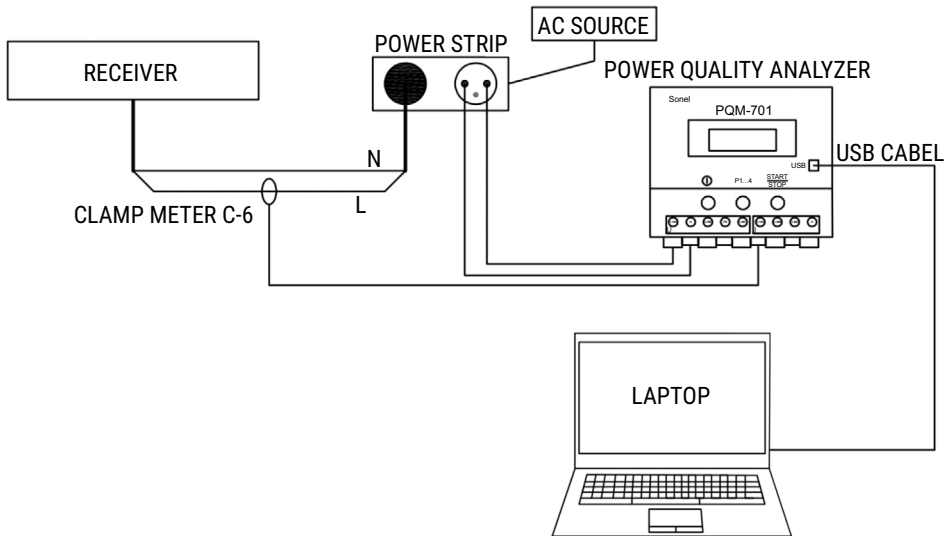


FIGURE 8.5. Diagram of the measuring system

The measurement of a single receiver lasted about one minute and included several 10-second measurement cycles. One of the middle cycles was selected in order to avoid the influence of transient states during switching on and off the tested devices. During the measurement, selected electrical parameters as well as current and voltage waveforms were recorded.

Table 8.1 presents the results of measurements of electrical parameters of selected, representative receivers in a typical household. Reactive power marked with a minus means it has a capacitive character.

Figures 8.7 – 8.12 present current waveforms of selected receivers and their harmonic spectra. More receivers were overviewed in [13].

TABLE 8.1 Values of active power, reactive power, deformation power, complex power, power factor PF (cosine) and total distortion factor of current THD_i

Device	P [W]	Q [var]	D [var]	S [VA]	PF [-]	THDi [%]
Satellite receiver	17.14	-6.77	28.59	34.02	0.51	152.43
Home Cinema	39.94	-1.70	61.29	72.85	0.54	152.69
Smartphone charger No. 1	13.35	-2.05	20.41	24.47	0.55	147.76
Smartphone charger No. 2	6.94	-1.44	10.08	12.32	0.56	138.54
Tablet charger	12.60	-3.24	20.65	24.40	0.52	155.86
Video game console	112.10	-32.44	39.67	123.25	0.91	34.04
Compact fluorescent lamp	8.00	-3.94	9.55	13.07	0.61	107.31
LED lamp No. 1	6.27	-7.06	7.21	11.88	0.53	75.40
LED lamp No. 2	12.40	-5.30	15.92	20.86	0.60	117.91
Laptop No. 1	8.00	-8.04	21.50	24.31	0.33	187.32
Laptop No. 2	13.40	-6.62	28.73	32.38	0.41	183.35
Desktop computer	72.87	4.34	74.51	104.31	0.70	101.97
LCD monitor	40.00	-6.08	61.40	73.53	0.54	149.99
LCD TV	135.69	-46.61	27.79	146.14	0.93	19.80
LED TV	44.00	-11.99	68.04	81.91	0.54	147.21

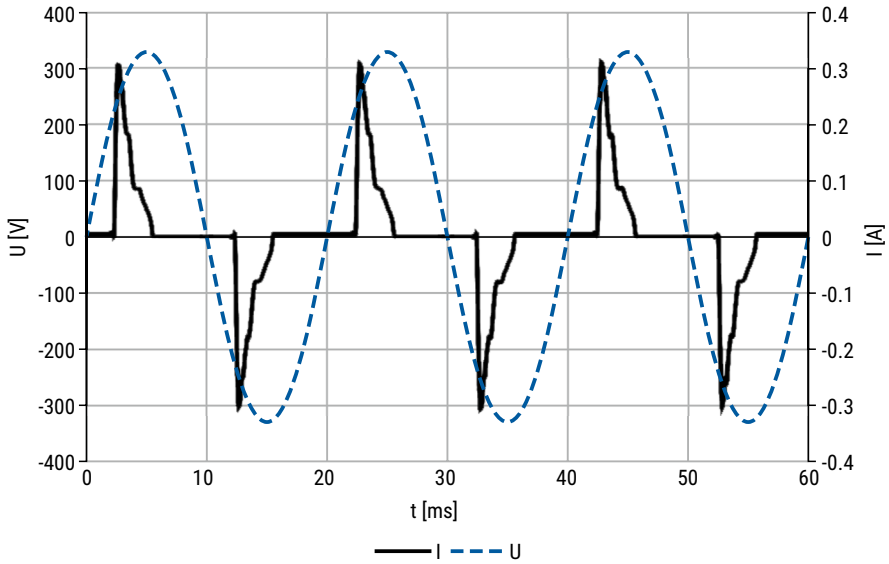


FIGURE 8.6. Current and voltage waveforms for LED source

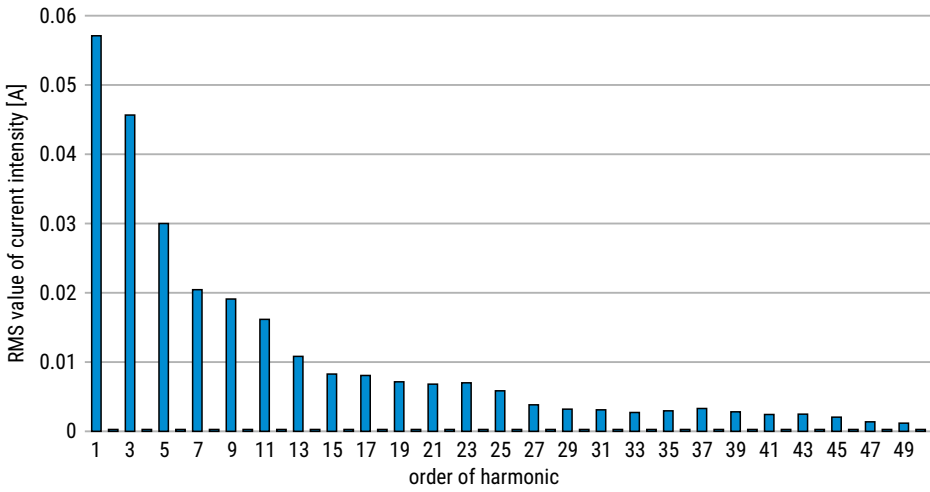


FIGURE 8.7. Harmonic spectrum of current received by LED source

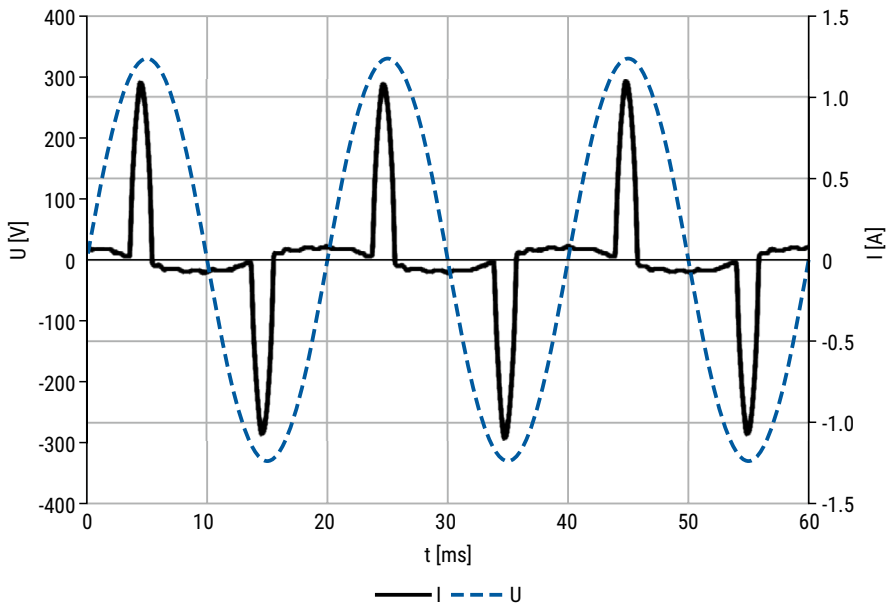


FIGURE 8.8. Current and voltage waveforms for LED TV

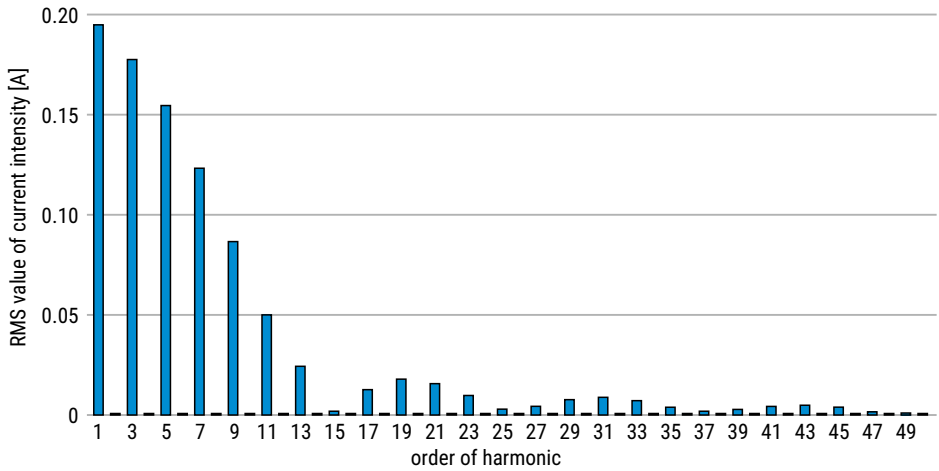


FIGURE 8.9. Harmonic spectrum of current received by LED TV

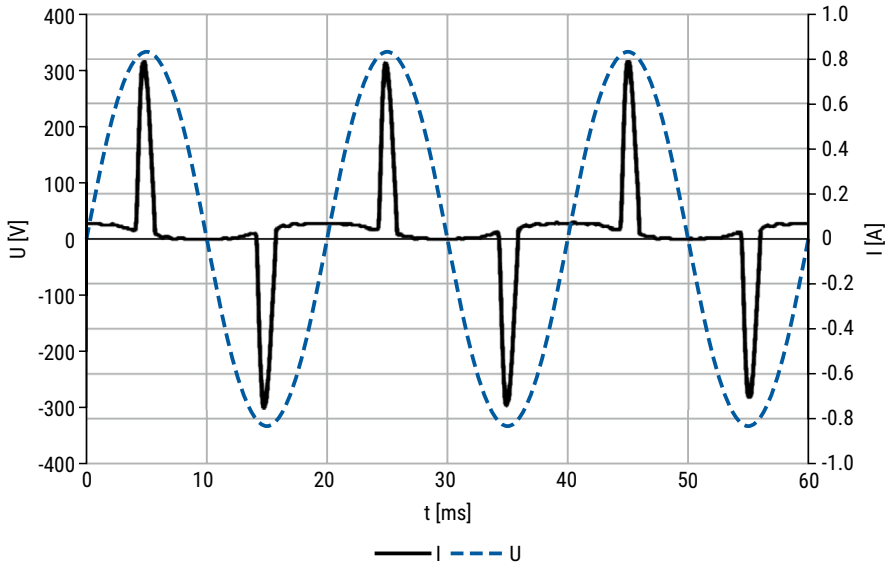


FIGURE 8.10. Current and voltage waveforms for laptop

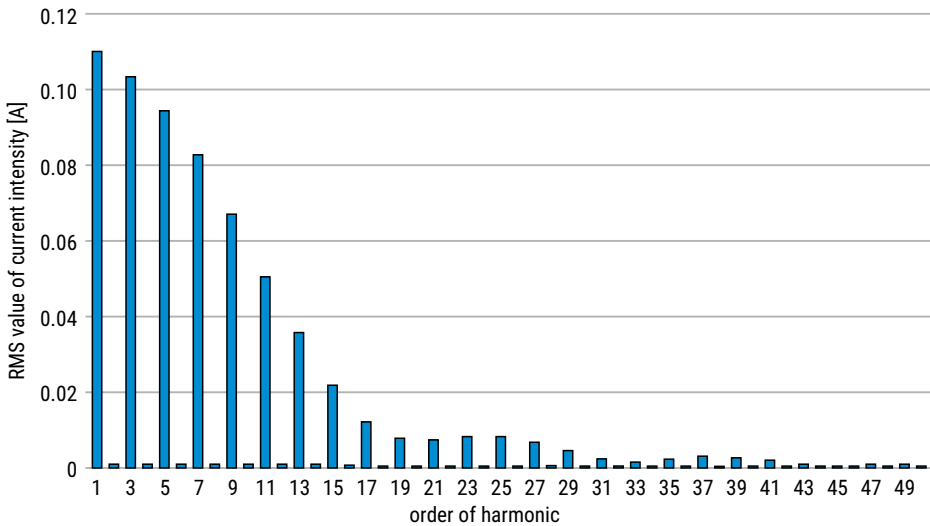


FIGURE 8.11. Harmonic spectrum of current received by laptop

B. Analysis of measurement results

Most of the receivers presented above receive strongly distorted current, as evidenced by the THDi value exceeding 100%. 13 out of 17 receivers presented in Table 8.1. This consumed more of the deformation power than the active power and in case of laptops more than twice as much. Figures 8.7, 8.9 and 8.11 show that in the harmonic spectrum

of received impulse currents, mainly odd harmonics are present, whose amplitude decreases with a harmonic order increase. The third harmonic has the highest value, and a significant value of the ninth harmonic can also be observed.

Capacitive reactive power consumption is also noticeable, which is about 25% of the value of the active power consumption of the presented set of receivers.

To observe the approximate effect of reactive power consumption and deformed current on active power losses, calculations were made on the basis of formulas (4) and (10), the results of which are presented in the tabular Table 8.2. The calculation assumes that the resistance of circuit is 1.5 Ω .

TABLE 8.2 The results of calculations presenting the approximate influence of modern receivers on the loss of active power in power supply wires

Device	$\cos\phi$ [-]	$\delta\Delta P_Q$ [%]	$\delta\Delta P_h$ [%]	ΔP [mW]	ΔP_Q [mW]	ΔP_h [mW]
Satellite receiver	0.93	13.50	553.83	8.33	1.12	46.14
Home Cinema	1.00	0.18	532.91	45.23	0.08	241.05
Smartphone charger No. 1	0.99	2.30	521.88	5.05	0.12	26.37
Smartphone charger No. 2	0.98	4.13	494.12	1.37	0.06	6.75
Tablet charger	0.97	6.20	658.20	4.50	0.28	29.63
Video game console	0.96	7.73	21.34	356.33	27.53	76.04
Compact fluorescent lamp	0.90	19.52	271.12	1.81	0.35	4.92
LED lamp No. 1	0.66	55.91	119.69	1.11	0.62	1.33
LED lamp No. 2	0.91	15.45	336.01	4.36	0.67	14.65
Laptop No. 1	0.71	50.25	1043.49	1.81	0.91	18.94
Laptop No. 2	0.90	19.62	887.98	5.09	1.00	45.21
Desktop computer	1.00	0.35	206.78	150.57	0.53	311.34
LCD monitor	0.99	2.26	511.42	45.37	1.02	232.02
LCD TV	0.95	10.55	7.88	522.07	55.10	41.14
LED TV	0.96	6.91	491.13	54.90	3.79	269.61
Total				1207.91	93.21	1365.15

It should be emphasized that the results of the calculations presented in Table 8.2 in the case of reactive power are reliable. However, in the case of harmonic influence they are approximate due to the complexity of the problem, which in the presented solutions is considered in a simplified way using the assumption that the increase of resistance for a given harmonic is proportional to \sqrt{h} .

Conclusions

The presented measurement results show that electrical energy receivers in a modern household – despite low active power consumption – entail passive and deformation power consumption, the latter of which, by significant values, has a noticeable impact on the value of apparent power. As mentioned in the theoretical part, an increase in apparent power is equivalent to an increase in the effective current value and thus losses of active power in the resistance of the wires of the low-voltage network and the transformer windings. However, the theoretical considerations based on measurements of single receivers are not reliable because while the reactive power can be summed up, for the deformation power it is not as simple, which can be observed in [13], where separate measurements of two single LED sources and measurements of the same sources switched on simultaneously are presented. You can see that while the sum of the reactive power is similar, the sum of the deformation power already diverges. This is due to the fact that harmonics of the same order in two different receivers may have a different phase shift and thus the resultant spectrum will look different.

In order to take into account the approximate influence of higher harmonics, calculations were made based on the effective values of individual harmonics included in [13]. The results are presented in Table 8.2 together with the results of calculations of active power losses resulting from reactive power. The losses of active power caused by the flow of reactive power and deformed currents received by the selected set of receivers may amount to about 120% of the active power losses present in the absence of the mentioned phenomena. Assuming that similar devices are present e.g. in a housing estate consisting of 500 apartments, these losses may amount to approx. 700 W in the wires alone. It should be noted, however, that the increase of power losses from the flow of distorted current, which is the main component of additional losses, was calculated using the simplification of the proportionality of the conductor resistance to \sqrt{h} , which could overstate the obtained result.

It should be noted that losses are not limited to wires only. A sensitive device is also the transformer, which, nonetheless, was not included in the above calculations.

The presence of the 3rd and 9th harmonics can additionally increase these losses in the N or PEN wire because the harmonics of these orders can accumulate there.

From the analysis of the presented measurement results it can be concluded that modern electricity receivers commonly used in households, despite the low consumption of active power, are characterized by a noticeable consumption of reactive power and distorted current. A single household is not a big problem, but when all the apartments are added together, e.g. housing estates, these values can reach a high level. As mentioned in the previous paragraph, theoretical considerations can only outline the problem, due to the difficulty of interpreting individual results.

However, this urges the need to inspect the actual values of individual power and current flows consumed by individual apartments, blocks of apartments or housing estates in order to verify the real scale of the influence of modern households on energy efficiency.

Authors: G. Hołdyński(e-mail: g.holdynski@pb.edu.pl), K. Szadkowski (e-mail: szadek19977@wp.pl), Białystok University of Technology, Faculty of Electrical Engineering, Wiejska 45D Str., 15-351 Białystok, Poland.

References

- [1] Bolkowski S., “Teoria obwodów elektrycznych,” Wydawnictwa Naukowo-Techniczne, Warszawa, 2008.
- [2] Khal T., “Sieci elektroenergetyczne,” Wydawnictwa Naukowo-Techniczne, Warszawa, 1984.
- [3] Skliński R., Hołdyński G., Sulkowski M.A., “Odbiorniki mocy biernej w systemie elektroenergetycznym oraz wpływ mocy biernej na warunki pracy sieci zasilająco-rozdziałczej,” *Wiadomości Elektrotechniczne*, Vol. 76, No. 5, 2008, pp. 32–35.
- [4] Hołdyński G., Skibko Z., “Kompensacja mocy biernej układów z asymetrią prądową,” *Elektro Info*, No. 10, 2018, pp. 64–66.
- [5] Hołdyński G., “Kompensacja mocy biernej farm wiatrowych,” *Elektro Info*, No. 6, 2018.
- [6] Hołdyński G., Skibko Z., “Kompensacja mocy biernej przy przebiegach odkształconych.” Cz. 2,” *Elektro Info*, No. 4, 2017, pp. 88–90
- [7] Hołdyński G., Skibko Z., “Kompensacja mocy biernej przy przebiegach odkształconych. Cz. 1,” *Elektro Info*, No. 1–2, 2017, pp. 56–58.
- [8] Hołdyński, Skibko, “Wpływ kompensacji mocy biernej na straty w układach elektroenergetycznych,” *Wiadomości Elektrotechniczne*, Vol. 87, No. 5, 2019.
- [9] Firlit A., “Teorie mocy w obwodach prądu przemiennego,” Accessed: <https://www.elektro.info.pl/artukul/jakosc-energii-elektrycznej/3374,teorie-mocy-w-obwodach-pradu-przemienego>.
- [10] Hołdyński G., Skibko Z., “Obciążalność prądowa długotrwała przewodów zasilających odbiorniki nieliniowe,” *Przegląd Elektrotechniczny*, Vol. 85, No. 3, 2009, pp. 70–74.
- [11] Hołdyński G., Skibko Z., “Straty mocy w układach wyposażonych w filtry aktywne,” Konferencja Jakości Energii Elektrycznej w Turzynie, 2017.
- [12] Kowalski Z., “Jakość energii elektrycznej,” Wydawnictwo Politechniki Łódzkiej, Łódź, 2007.
- [13] Szadkowski K., “Analiza odkształcenia prądów pobieranych przez wybrane odbiorniki użytkowane w gospodarstwach domowych,” Engineer’s thesis, Politechnika Białostocka, 2020.
- [14] Hanzelka Z., “Jakość energii elektrycznej. Część 4 –Wyższe harmoniczne napięć i prądów,” www.twelvee.com.pl.
- [15] Rak J., Gała M., Jagieła K., Kępiński M., “Analiza obciążenia i strat w transformatorach przekształtnikowych układów napędowych,” *Maszyny Elektryczne: zeszyty problemowe*, No. 1(89), 2011, pp. 139–147.
- [16] Szadkowski K., Hołdyński G., “Wyższe harmoniczne prądu we współczesnym gospodarstwie domowym,” *Wiadomości Elektrotechniczne*, Vol. 88, No. 6, 2020, pp. 9–16.

Chapter 9

The numerical analysis of the influence of geometry planar coil systems on the efficiency of the WPT system

Jacek Maciej Stankiewicz

Bialystok University of Technology, Faculty of Electrical Engineering

The article presents results for a numerical analysis of a Wireless Power Transfer (WPT) system consisting of transmitting and receiving plane coils. The analysis takes into account different variants of WPT system geometry (distance between the transmitting-receiving coils, number of turns). The influence of variable system geometry and the frequency on system efficiency is observed. The analysis is based on the Finite Element Method (FEM) with antiperiodicity boundary conditions. The obtained results indicate at which system parameters wireless energy transfer is possible.

Index terms: Finite Element Method (FEM), magnetic field, numerical methods, wireless power transfer (WPT).

Introduction

In recent years, there has been a clear increase in energy demand in wireless and mobile devices. Their computing power and the number of supported sensors (e.g. fingerprint sensor or iris scanner) grew [1–9, 14–20]. These factors affect the increasing demand for batteries with increased capacity, extend the charging time and determine the mobility of devices. One way to supply mobile devices with energy is charging using wireless power transfer (WPT).

However, the topology of parallel flat coils, working as a group of transmitters and receivers, is still not fully developed. This article presents one of such systems which includes non-periodic structure arranged transceivers and receivers coils. The proposed WPT system could be used to charge electric devices as a wireless power transfer system. An analysis of the influence of system parameters is carried

out, including number of turns, distance between coils and frequency of system operation on the efficiency of energy transmission. The article presents and describes the results of numerical analysis.

Wireless power transfer systems

One way to supply mobile devices with energy is charging using WPT, which becomes more accessible in scattered grids of many interdependent sources and loads. Due to the concept of inductive power transfer wireless charging of modern technology (smartphones, laptops) [1, 6] is possible. WPT is increasingly used, among others in the automotive industry in solutions for hybrid and electric cars [4–5, 9]. Charging an Audi car with WPT was first proposed in 2007 (Fig. 9.1).



FIGURE 9.1. Audi wireless charging for electric vehicles [9]

Wireless charging is also considered in lighting in hard-to-reach places [10] or intelligent buildings with sensors inside the walls and in the systems of beacons in hard-to-reach places [3, 14–18, 20]. WPT is also used in LED-based lighting. This approach does not use wired power such as a battery. Thanks to this, it is possible to use cabin lighting and many architectural possibilities are created (Fig. 9.2).



FIGURE 9.2. The use of WPT for LED lighting [12]

The authors [12, 19] presented a WPT charging solution for e.g. laptops or smart-phones. They found that in the next 10 years, such a solution would account for up to 80% of applications. The possibility of charging the battery from a distance of 10 cm without the use of cables is described in [12].

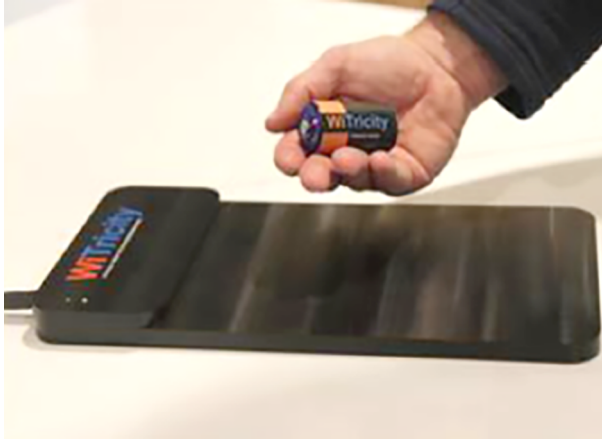


FIGURE 9.3. Wireless battery charger [12]

WPT also has medical applications. Resonant coupling has been recognized in medical devices. Today, an internal battery powers most implantable medical devices and sensors. WPT technology reduces the need for a built-in power source to ensure the autonomy of this type of device.

Analyzed model of wireless power transfer

The article proposes a method of wireless charging through the use of a periodic system containing a plane made of transmitting coils and a plane of receiving coils (Fig. 9.4). The pair: transmitter-receiver, consisting of coils with a radius $r = 30$ mm and number of turns n_t is treated as a WPT cell with dimensions $d \times d$, where $d \approx 2r$. The transmitting and receiving coils are placed at a distance h (Figs. 9.4, 9.5). The turns are placed on a plastic carcass. The compensating capacitor connected with the coil is settling. A configuration of WPT cells on the plane leads the occurrence of energy transmission. The system here is aperiodicity – different directions of winding the turns (Fig. 4). The transmitting surface is powered so that each transmitter is connected in parallel with a sinusoidal voltage source with the effective value U . The analyzed model of the WPT system guarantees an increase in the density of transmitted power in the area between the receiving and transmitting surfaces. Each WPT cell is connected with a separate load (Z).

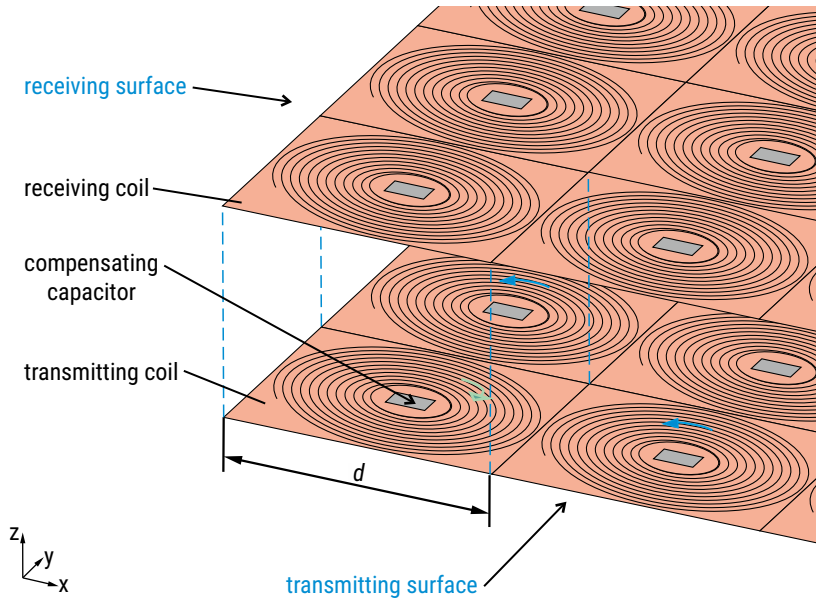


FIGURE 9.4. Analyzed WPT system

Numerical analysis of WPT system

In the analysis of the proposed WPT system the Finite Element Method (FEM) was used. This numerical method allows to analyze energy transfer in a system composed of many WPT cells. The following need to be taken into account: coil turns distribution, coil geometry, WPT cell number and elements of the electric circuit connected to each coil.

The analysis omits the carcass in the model, assuming that it is made of non-conductive and non-magnetic material ($\mu = \mu_0$). The capacitor is modelled as an element with a concentrated capacity C . Each transmitting coil was connected to a voltage source with an effective value U and frequency f , forcing the flow current transmitter I .

In the analysis all cells forming the transmitting and receiving surfaces are taken into account. Due to the application of system periodicity, the analysis of the WPT system can be reduced to a set of transmitting-receiving coils (Fig. 9.5).

In this case, the WPT system will be simplified to a single cell filled with air and containing a pair of transmitting and receiving coils (Fig. 9.5). PML absorption conditions were used on the surfaces parallel to the XY surface. On the side surfaces, the antiperiodicity boundary option built into the Comsol program was used, which allowed for the analysis of the system with variable winding of the coils.

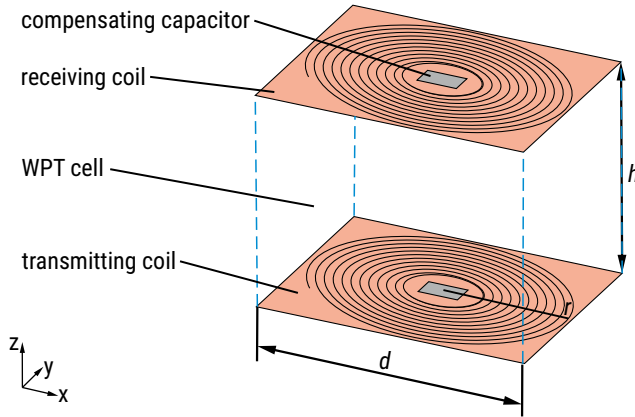


FIGURE 9.5. A single WPT cell containing a transmitting and receiving coil

Using magnetic vector potential could solve the problem of energy transport in the analyzed model

$$\mathbf{A} = [A_x \ A_y \ A_z]. \quad (9.1)$$

The use of the Helmholtz equation could provide a description of magnetic phenomena in the frequency domain

$$\nabla \cdot (\mu_0^{-1} \nabla \cdot \mathbf{A}) - j\omega\sigma\mathbf{A} = \mathbf{J}_{ext}, \quad (9.2)$$

where:

- ω – pulsation [rad/s],
- σ – conductivity [S/m],
- \mathbf{J}_{ext} – external current density vector [A/m²].

The values used in numerical analysis are presented in Table 9.1. Analysis connected with frequency domain from $f_{min} = 100$ kHz to $f_{max} = 1000$ kHz.

TABLE 9.1. Values used in the calculations

parameter	symbol	value
wire with a diameter	w	250 μm
conductivity of wire	σ	$5.6 \cdot 10^7$ S/m
source with an effective value	U	5 V
thickness of wire insulation	i	10 μm
load	Z	50 Ω

The influence of the model coils of radius ($r = 30$ mm) and different number of turns (n_t) and distance between the transmitter and receiver coil (h) on the efficiency of the system was analyzed (Tab. 2).

TABLE 9.2. Considered variants of the WPT system

r [mm]	n_t	h [mm]
30	35	15 ($r/2$) and 30 (r)
30	70	15 ($r/2$) and 30 (r)
30	105	15 ($r/2$) and 30 (r)

Results of the analysis

The results of the analysis of the WPT system were obtained by the numerical method. The norm of the current intensity of the transmitting (I_z) and receiving coil (I_o) and the transfer efficiency (η) were analyzed, depending on the structure of the model. The numerical model was created in the *Comsol Multiphysics program*, using included coil approximation models with an attached circular part and boundary conditions (PML and antiperiodicity), and solved using the FEM method. The analyzed model contained 652140 degrees of freedom.

Figures 9.6–9.11 present comparisons of WPT efficiency (Figs. 9.10, 9.11), the transmitter current (Figs. 9.6, 9.7), the receiver current (Figs. 9.8, 9.9) for different values of the number of turns of the transmitting and receiving coils and different distances between these coils.

The characteristics for the model, where the distance between the coils was half the radius ($h = 15$ mm), are shown in Figs. 9.6, 9.8, 9.10. On the other hand, Figs. 9.7, 9.9, 9.11 show the characteristics for the model, where the distance between the coils was equal to the radius ($h = 30$ mm).

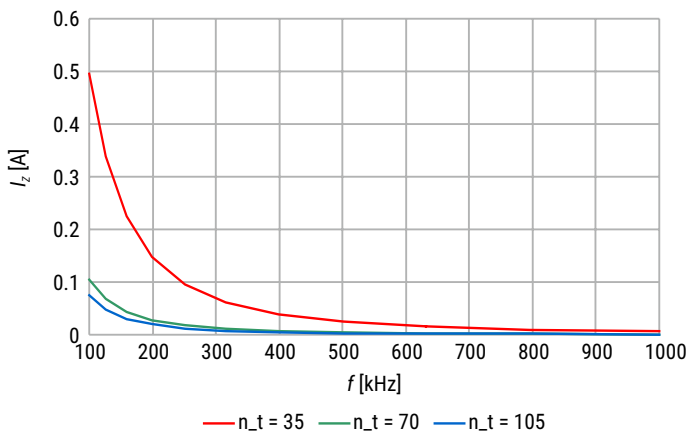


FIGURE 9.6. Results comparison of transmitter current (I_z) dependent on the number of turns (n_t) for the case $h = 15$ mm.

In Figure 9.6, it can be seen that the transmitter current decreases with increasing frequency. A similar dependence is observed for the receiver current, as shown in Figure 9.7. The smaller the number of turns causes, the greater the value of the current intensity.

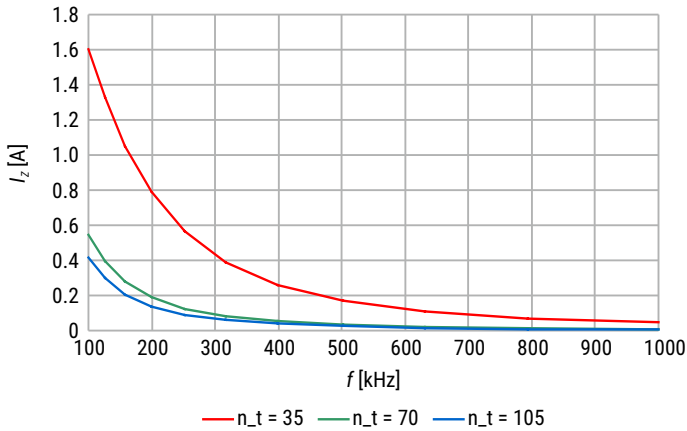


FIGURE 9.7. Results comparison of transmitter current (I_z) dependent on the number of turns (n_t) for the case $h = 30$ mm.

The efficiency of energy transfer increases with increasing frequency and already at approx. 200 kHz, it reaches the maximum value of approx. 96%, as shown in Figure 9.10.

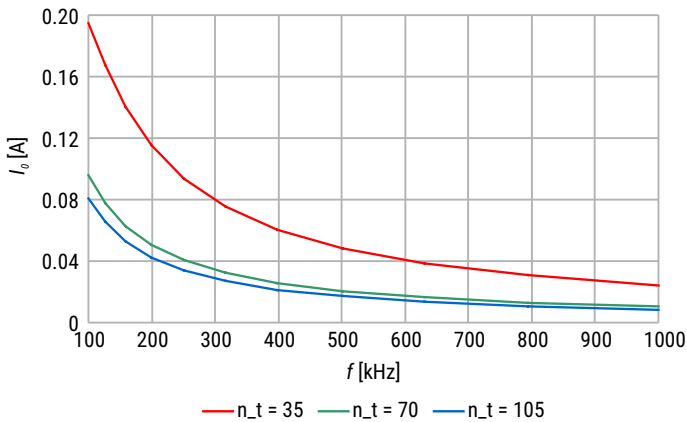


FIGURE 9.8. Results comparison of receiver current (I_o) dependent on the number of turns (n_t) for the case $h = 15$ mm.

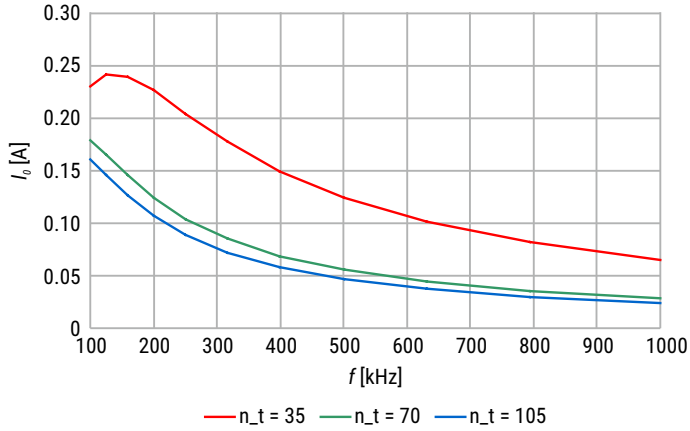


FIGURE 9.9. Results comparison of receiver current (I_o) dependent on the number of turns (n_t) for the case $h = 30$ mm.

Figs. 9.7, 9.9, 9.11 show the effect of the number of turns and frequency on the transmitter current, receiver current and system efficiency for the model, where the distance between the coils was the same as the radius, i.e. 30 mm.

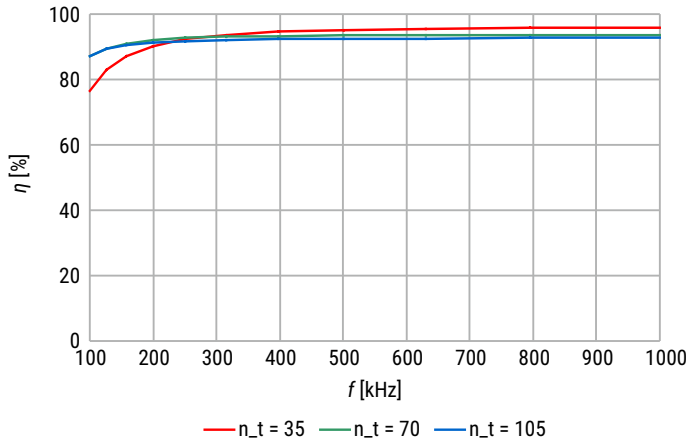


FIGURE 9.10. Results comparison of power transfer efficiency (η) dependent on the number of turns (n_t) for the case $h = 15$ mm.

The waveform of the transmitter and receiver current is similar to the previous case, i.e. the currents decrease with increasing frequency. With one difference. As can be seen in Figure 9.9, for the number of turns equal to 35, the receiver current increases with increasing frequency and reaches its maximum value when the efficiency of the system is 50%, and then decreases. The efficiency of energy transfer increases with increasing frequency and reaches the maximum value of approx. 94% only at approx. 600 kHz, which is noticeable in Figure 9.11.

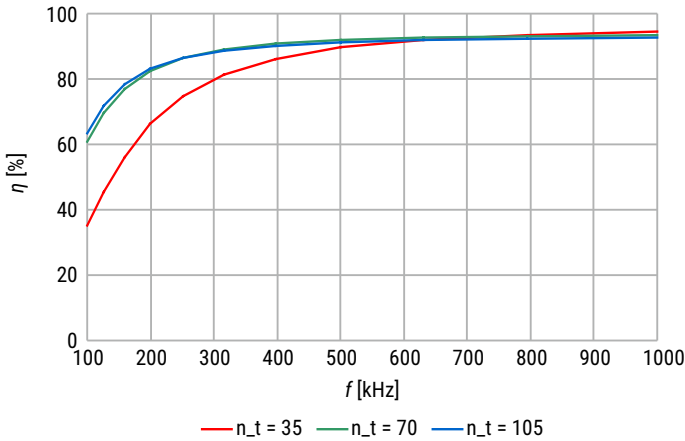


FIGURE 9.11. Results comparison of power transfer efficiency (η) dependent on the number of turns (n_t) for the case $h = 30$ mm.

In the initial frequency range, efficiency is much lower for the model where the distance between the coils is the same as the radius, i.e. 30 mm, than for the model where the distance between the coils is half the radius, i.e. 15 mm. However, for higher frequencies, the efficiency values for both models are similar.

Conclusions

The presented non-periodic wireless power transfer system was investigated using the numerical method. The article presents the author's numerical model containing two planes of transmitting and receiving coils forming the WPT system. The influence of e.g. the distance between the transmitter and the receiver, the number of turns on the efficiency of the WPT system was analyzed. The analysis covered a wide frequency range.

In the initial frequency range, efficiency is much lower for the model where the distance between the coils is the same as the radius, i.e. 30 mm, than for the model where the distance between the coils is half the radius, i.e. 15 mm. However, for higher frequencies, the efficiency values for both models are similar.

The numerical analysis of energy transfer in the system consisting of many WPT cells requires consideration of the details of the model structure, such as: geometry of the coils, winding distribution, number of WPT cells, as well as elements of the electric circuit connected to each of the coils and the adopted boundary conditions. An increase in the accuracy of the mapping of the model results in an increase in the number of degrees of freedom and computation time.

The proposed configuration of the system ensures an increase in power transmitted density in the area between the receiving and transmitting surfaces. It also enables the selection of power conditions, depending on the imposed requirements. The proposed solution can be used for wireless charging of mobile devices, and to shape the distribution of the magnetic field. Due to the FEM method, it is possible to analyze the influence of the number of turns, radius of the coil, distance between coils, and size of the WPT cell on the efficiency of the system. The presented results of the numerical analysis can be helpful with the use of optimization algorithms in order to obtain maximum efficiency of the WPT system.

This work was supported by the Ministry of Science and Higher Education in Poland at Bialystok University of Technology under research subsidy No. WI/WE-IA/11/2020.

Author: J. M. Stankiewicz (e-mail: j.stankiewicz@doktoranci.pb.edu.pl), Bialystok University of Technology, Faculty of Electrical Engineering, Wiejska 45D Str., 15-351 Bialystok, Poland.

References

- [1] S. D. Barman, A. W. Reza, N. Kumar, Md. E. Karim, A. B. Munir, "Wireless powering by magnetic resonant coupling: Recent trends in wireless power transfer system and its applications," *Renewable and Sustainable Energy Reviews*, Vol. 51, pp. 1525–1552, 2015.
- [2] X. Liu, G. Wang, "A Novel Wireless Power Transfer System With Double Intermediate Resonant Coils," *IEEE Transactions on Industrial Electronics*, Vol. 63, pp. 2174–2180, 2016.
- [3] Z. Wenxing, L. Chi Kwan, S. Y. R. Hui, "General analysis on the use of Tesla's resonators in domino forms for wireless power transfer," *IEEE Transactions on Industrial Electronics*, Vol. 60, No. 1, pp. 261–70, 2013.
- [4] C. T. Rim, C. Mi, "Wireless Power Transfer for Electric Vehicles and Mobile Devices," John Wiley & Sons, Ltd.: Hoboken, United States, pp. 473–490, 2017.
- [5] K. Fujimoto, K. Itoh, "Antennas for Small Mobile Terminals," 2nd ed., Artech House: Norwood, USA, pp. 30–70, 2018.
- [6] S. Liu, J. Su, J. Lai, "Accurate Expressions of Mutual Inductance and Their Calculation of Archimedean Spiral Coils," *Energies*, Vol. 12, No. 10, pp. 1–14, 2017.
- [7] "Alternative Energy," EETimes; June 21, 2010.
- [8] S. Mohan, M. Hershenson, S. Boyd, T. Lee, "Simple Accurate Expressions for Planar Spiral Inductances," *IEEE Journal of solid-state circuits*, Vol. 34, No. 10, pp. 1419–1424, 1999.
- [9] AudiUrbanConcept.Ingolstadt,Germany. Accessed: <http://mb.cision.com/Public/Migrated/Wpy/89774/9160790/a30c4d7a8486de84.pdf>; 2011, p. 7.
- [10] P. Martin, B. J. Ho, N. Grupen, S. Muñoz, M. Srivastasa, "An iBeacon Primer for Indoor Localization," [in:] *Proceedings of the 1st ACM Conference on Embedded Systems for Energy-Efficient Buildings (BuildSys'14)*, Memphis, USA, pp. 190–191, November 2014.
- [11] D. Fitzpatrick, "Implantable Electronic Medical Devices," Academic Press: San Diego, United States, pp. 7–35, 2014.
- [12] M. Kesler, "Highly Resonant wireless power transfer: safe, efficient and over distance," WiTricity Corporation, 2013.

- [13] Z. Luo, X. Wei, "Analysis of Square and Circular Planar Spiral Coils in Wireless Power Transfer System for Electric Vehicles," *IEEE Transactions on Industrial Electronics*, Vol. 65, pp. 331–341, 2018.
- [14] A. Steckiewicz, J. M. Stankiewicz, A. Choroszucho, "Numerical and Circuit Modeling of the Low-Power Periodic WPT Systems," *Energies*, Vol. 13, No. 10, pp. 1–17, 2020.
- [15] Z. Zhang, H. Pang, A. Georgiadis, C. Cecati, "Wireless Power Transfer-An Overview," *IEEE Trans. Ind. Electron.*, 66, No. 2, pp. 1044–1058, 2019.
- [16] D. C. Meeker, "An improved continuum skin and proximity effect model for hexagonally packed wires," *Journal of Computational and Applied Mathematics – Elsevier*, Vol. 236, pp. 4635–4644, 2012.
- [17] D. Kim, A. Abu-Siada, A. Sutinjo, "State-of-the-art literature review of WPT: Current limitations and solutions on IPT," *Electr. Pow. Syst. Res.*, Vol. 154, pp. 493–502, 2018.
- [18] T. Batra, E. Schaltz, S. Ahn, "Effect of ferrite addition above the base ferrite on the coupling factor of wireless power transfer for vehicle applications," *Journal of Applied Physics*, Vol. 117, 17D517, 2015.
- [19] P. Manivannan, S. Bharathiraja, "Qi Open Wireless Charging Standard – A Wireless Technology for the Future," *IJECS*, Vol. 2, No. 3, pp. 573–579, 2013.
- [20] M. M. El Rayes, G. Nagib, W. G. A. Abdelaal, "A Review on Wireless Power Transfer," *IJETT*, Vol. 40, pp. 272–280, 2016.

Chapter 10

Estimation of the maximum load power in periodic WPT systems

Jacek Maciej Stankiewicz

Bialystok University of Technology, Faculty of Electrical Engineering

The article presents results for a proposed analytical solution to the analysis of the periodic Wireless Power Transfer (WPT) system. The model consists of transmitting and receiving plane coils. The analysis takes into account different variants of geometry like distance between the transmitting and receiving coils and the number of turns. The influence of variable system geometry and the frequency on system efficiency is observed. The obtained results indicate at which system parameters wireless energy transfer is possible. The proposed systems can be used for wireless charging of mobile devices, and to shape the distribution of the magnetic field. The given solution allows for studying the influence of coil geometry on power transmission.

Index terms: wireless power transfer (WPT), magnetic field, analytical methods, inductive elements.

Introduction

The demand for energy in wireless devices continues to increase. Along with the growing demand for such energy, problems arise regarding the requirements for: batteries with increased capacity or limited charging time. It is becoming more common to power mobile devices by charging with the use of wireless power transfer (WPT) [1–8].

WPT is increasingly used, among others in the automotive industry, in solutions for hybrid and electric cars [4–9]. In order to charge the batteries while driving, distributed coils along the path of the car were used. Thanks to such use of WPT, it is possible to use electric vehicles, e.g. in factories.

The WPT system is an alternative method of charging wireless devices, where a pair of coils [9–13] or an array of coils [14, 15] is used. The WPT system is also considered in the systems of beacons [10], medical implants in human body [11] and inside buildings with sensors [24–25].

WPT systems are still analyzed by using various solutions and configurations of this type of systems [16–20]. Every solution requires a multi-variant analysis and verification of the results. In order to avoid early prototyping and performing a number of analyzes, it is possible to apply analytical and numerical methods at the design stage.

In the article, the WPT system, in which a set of several coils participating in energy transfer was replaced with surfaces made of periodically distributed planar coils, was analyzed. Adjacent segments containing a pair of coils (transmit and receive) between which energy is exchanged, can be used to power multiple independent loads or replace conventional WPT systems. The developed analytical method for solving WPT systems was presented. Its target is to quickly determine the parameters of the system (e.g. power, efficiency) without the need to make complex models and solve them using numerical methods.

Calculations were performed to determine the parameters of WPT systems, i.e. equivalent properties, source power, receiver power and efficiency. The analysis was multi-variant – the number of turns, their parameters and the distance between coils were changed.

The article presents the approach and results of the analytical method. By an appropriate selection of load resistance, it was possible to calculate the maximum power of the receiver of the WPT system. The proposed method may be an alternative to the use of experimental prototypes applied in WPT systems.

Analyzed model

This article presents the periodic wireless power transfer system with many inductive elements. The considered system is composed of many pairs of transmitters and receivers, which constitute a WPT cell with outer dimensions $d \times d$ (Fig. 10.1).

The coils are identical with parameters: radius (r), where $d \approx 2r$ and number of turns (n). The windings are wound around a dielectric carcass with additional compensating capacitors. The transmitting and receiving coils are placed at a distance (h). The analyzed periodic distribution of WPT cells give transmitting and receiving surfaces, where between them the energy transmission occurs. The transmitting surface consist of coils which are connected parallel to a sinusoidal voltage source (U).

Planar spiral coils were wound by several dozen of turns, made of ultra-thin wires with diameter w and insulated from each other by an electrical insulator of thickness i . The compensating capacitor can be modeled as an element with lumped capacity C . A voltage source (U) with specified frequency (f) is connected with the transmitting coil, while load Z is connected with the receiving coil.

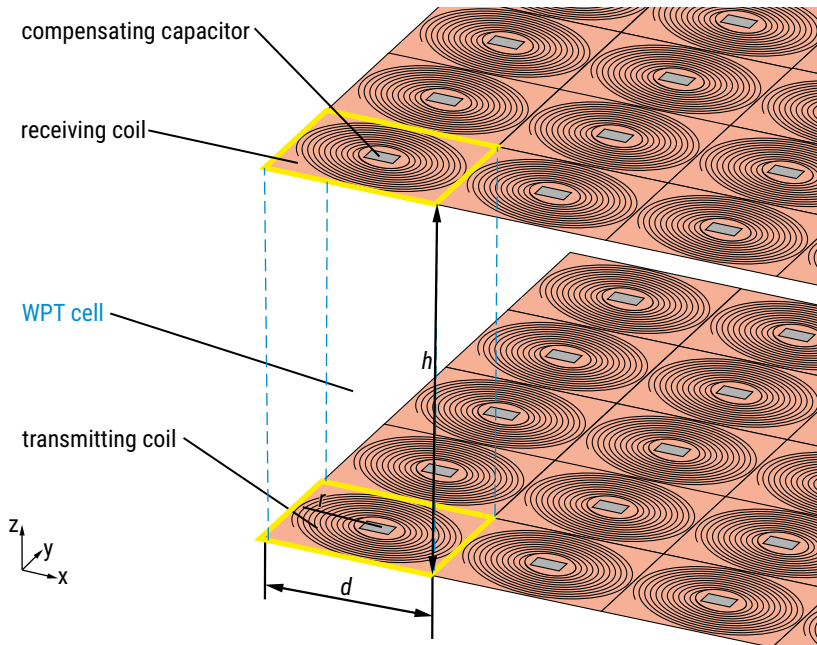


FIGURE 10.1. Periodic wireless power transfer system

Analytical approach

The implementation of the numerical model is more difficult than the analytical one due to, inter alia, the appropriate selection of boundary conditions and many necessary simplifications imposed by the adopted numerical method. Therefore, in many cases a simpler model is desirable, providing a faster initial solution.

The article presents the developed analytical solution for the model of periodic WPT system (Fig. 10.1). The analysis of the infinitely extensive periodic network was reduced to the case of a single WPT cell. The solution of the analytical model in the frequency domain can be performed using methods of circuit analysis (Fig. 10.2). The main problem in this type of analysis is to determine the values of the lumped parameters, taking into account the influence of adjacent segments on the equivalent inductances of the transmitting coil L_{tr} and the receiving coil L_{re} and their mutual inductance M_{tr} .

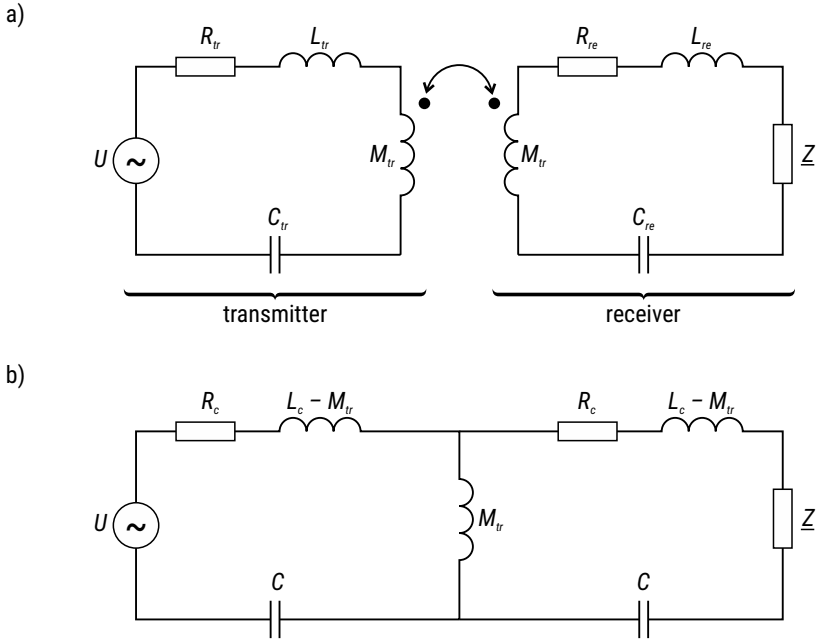


FIGURE 10.2. Analytical model of the WPT cell: (a) overall model of periodic cell, (b) replacement model of the cell for identical transmitting and receiving coils

The resistance of a coil is determined by replacing the spiral structure of windings converging circles of equal width $w+i$. The whole length of all circles is represented by:

$$l_{sum} = 2\pi n[r - (n-1)(w+i)]. \quad (10.1)$$

The equation determining the resistance of a conductor is described by:

$$R_c = \frac{l_{sum}}{\sigma\pi \frac{w^2}{4}} \quad (10.2)$$

The self-inductance of a spiral planar coil is calculated using equation [14]:

$$L_{self} = \frac{\mu_0 c_1 d_m n^2}{2} \left[\ln\left(\frac{c_2}{wsp}\right) + c_3 wsp + c_4 wsp^2 \right], \quad (10.3)$$

where d_m – diameter and wsp is a fill factor;

$$d_m = \frac{2r + 2[r - n(w+i)]}{2}, \quad (10.4)$$

$$wsp = \frac{2r - 2[r - n(w+i)]}{2r + 2[r - n(w+i)]}. \quad (10.5)$$

Coefficients c_1, c_2, c_3, c_4 used in the equation (10.3) depend on the shape of a coil [14]. For identical transmitting and receiving coils the calculated inductances are equal to $L_c = L_{tr} = L_{re}$ (Figure 10.2). Mutual inductance M_{pe} , which directly results from the periodic distribution of coils arranged on the surface, is a sum of all mutual inductances [8, 21]

$$M_{pe} = \sum_i \sum_j (M_{x+i,y+j}) - M_{x,y}, \quad (10.6)$$

where:

$M_{x+i,y+j}$ – mutual inductance between the coil and the coil at i -th column and j -th row,
 $M_{x,y} = L_{self}$ is self-inductance.

Taking into account the assumptions that the system is periodic and symmetrical ($M_{x+i,y+j} = M_{x-i,y-j}$), equation (10.6) is simplified to the formula:

$$M_{pe} = 8M_{x,y+1}, \quad (10.7)$$

where:

$M_{x,y+1}$ is mutual inductance between the coil and an edge of the adjacent coil (Figure 10.2) and is calculated on the basis of the formula [8, 14, 21]

$$M_{x,y+1} = \frac{\mu_0 p^2}{4\pi} \int_{\Phi_1}^{\Phi_0} \int_{\Phi_1}^{\Phi_0} \frac{[(1 + \phi_1 \phi_2) \cos(\phi_2 - \phi_1) - (\phi_2 - \phi_1) \sin(\phi_2 - \phi_1)] d\phi_1 d\phi_2}{\sqrt{(d_m + p\phi_2 \cos \phi_2 - p\phi_1 \cos \phi_1)^2 + (p\phi_2 \sin \phi_2 - p\phi_1 \sin \phi_1)^2}} \quad (10.8)$$

where:

$$p = (w+i)/(2\pi),$$

$$\Phi_1 = [r - (w+i)n]/p,$$

$$\Phi_0 = r/p.$$

Assuming equation (10.7), the inductance of the considered coil in the segment $A_{x,y}$ takes a form of:

$$L_c = L_{self} + M_{pe} = L_{self} + 8M_{x,y+1}. \quad (10.9)$$

Compensating capacity C at definite frequency is represented by:

$$C(f) = \frac{1}{4\pi^2 f^2 L_c} = \frac{1}{4\pi^2 f^2 (L_{self} + M_{pe})} = \frac{1}{4\pi^2 f^2 (L_{self} + 8M_{x,y+1})} \quad (10.10)$$

Mutual inductance M_{tr} between the transmitter and the receiver is presented by

$$M_{tr} = \frac{\mu_0 p^2}{4\pi} \int_{\Phi_1}^{\Phi_0} \int_{\Phi_1}^{\Phi_0} \frac{[(1 + \phi_1 \phi_2) \cos(\phi_2 - \phi_1) - (\phi_2 - \phi_1) \sin(\phi_2 - \phi_1)] d\phi_1 d\phi_2}{\sqrt{h^2 + p^2 \phi_1^2 + p^2 \phi_2^2 - 2p^2 \phi_1 \phi_2 \cos(\phi_2 - \phi_1)}} \quad (10.11)$$

Assumptions of the analysis

Using the proposed analytical method, many variants of the periodic WPT systems were analyzed (Table 1). With the same coil radius, the number of turns and the distance between the coils (transmitter and receiver) were changed.

TABLE 10.1. Geometrical parameters for analyzed models

r [mm]	n	h [mm]
25	40	12.5 ($r/2$) and 25 (r)
25	50	12.5 ($r/2$) and 25 (r)
25	60	12.5 ($r/2$) and 25 (r)
25	70	12.5 ($r/2$) and 25 (r)
25	80	12.5 ($r/2$) and 25 (r)
25	90	12.5 ($r/2$) and 25 (r)

The values, which were used in the analysis, are presented in Table 10.2.

TABLE 10.2. Values used in the analysis

parameter	symbol	value
wire with a diameter	w	200 μm
conductivity of wire	σ	$5.6 \cdot 10^7$ S/m
source with an effective value	U	1 V
thickness of wire insulation	i	5 μm

The analysis is connected with the frequency domain from $f_{min} = 100$ kHz to $f_{max} = 1000$ kHz. The value of coefficients used in equation (10.3) are $c_1 = 1$, $c_2 = 2.5$, $c_3 = 0$, $c_4 = 0.2$.

On the basis of the obtained results for several exemplary periodic WPT systems, the correctness of the proposed analytical model was verified by comparing the active power of the receiver:

$$P_o = Z \left| I_{re} \right|^2, \quad (10.12)$$

where I_{re} is a current flowing through the receiving coil.

Transmitter power is represented by:

$$P_z = U I_{tr}, \quad (10.13)$$

where I_{tr} is a current flowing through the transmitting coil.

Using equations (12) and (13), the power transfer efficiency was described by:

$$\eta = \frac{P_o}{P_z} 100\%. \quad (10.14)$$

Additionally, the results were based on the correct selection of Z_p (optimal load impedance) to make the maximum power transfer:

$$Z_p = R_c + \frac{\omega^2 M_{tr}^2}{R_c}. \quad (10.15)$$

Results of the analysis

The results of the analysis of the WPT system were obtained by the analytical method. The results were related to the maximum load power. In order to determine the maximum power transmitted to the receiver, the values of the load impedance were calculated, taking into account the number of turns and the distance between the coils. The transmitter power (P_z) (Figs. 3, 6, 9, 12), the receiver power (P_o) (Figs. 4, 7, 10, 13), power transfer efficiency (η) (Figs. 5, 8, 11, 14) were presented on this basis.

The characteristics for the model, where the distance between the coils was half the radius ($h = 12.5$ mm) are shown in Figs. 10.3–10.8. Figures 10.9–10.14 show the characteristics for the model, where the distance between the coils was equal to the radius ($h = 25$ mm).

The efficiency of the system for $n = 40 \div 60$ with $h = 12.5$ mm reaches 50% with P_o in the range of 62÷84 mW. However, for a larger number of turns, with a lower receiver power (50÷56 mW), a higher efficiency of the WPT system is achieved.

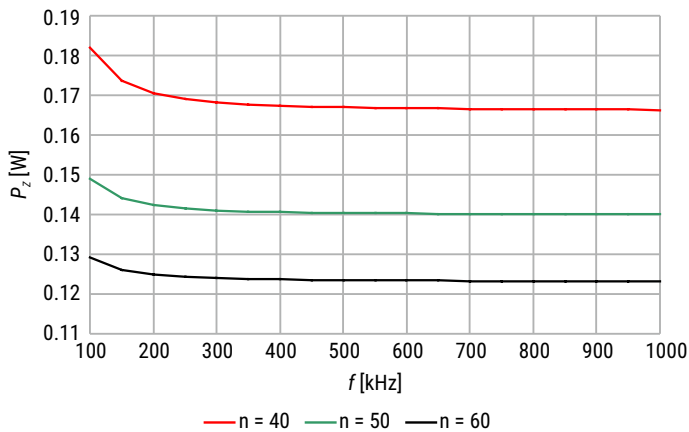


FIGURE 10.3. Results of transmitter power (P_z) dependent on the number of turns ($n=40\div60$) at distance $h=12.5$ mm

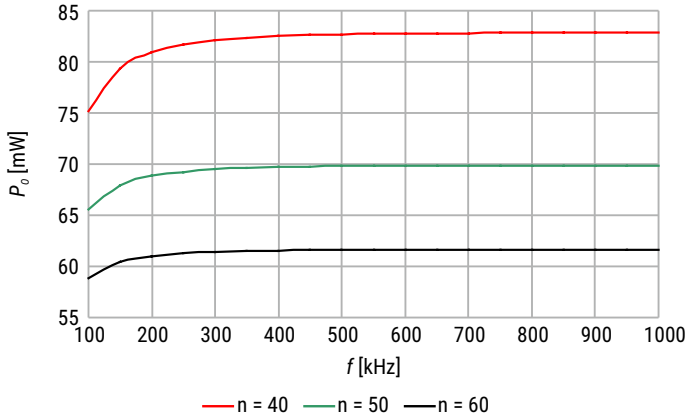


FIGURE 10.4. Results of receiver power (P_o) dependent on the number of turns ($n=40\div 60$) at distance $h=12.5$ mm

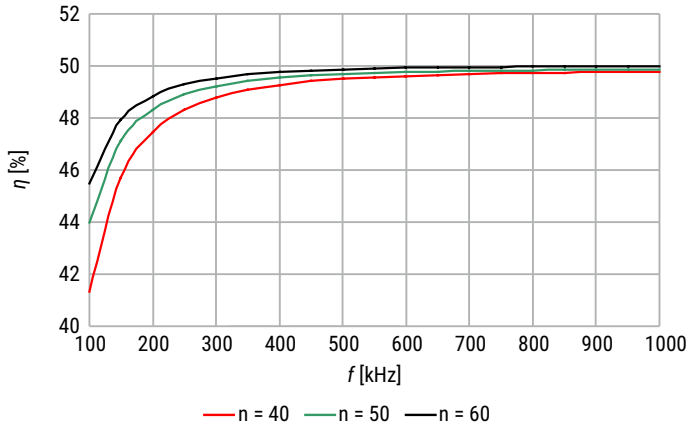


FIGURE 10.5. Results of power transfer efficiency dependent on the number of turns ($n=40\div 60$) at distance $h=12.5$ mm

Doubling the distance causes the transmitter power to have higher values than at $h = 12.5$ mm by even 70% (Figs. 10.3, 10.9).

Doubling the distance between the coils results in lower efficiency system values. For $n = 40\div 60$, the efficiency does not reach 50% (Fig. 10.11). At 500 kHz and twice the distance between the coils, the efficiency is 10% lower than for the half-radius distance (Figs. 10.5, 10.11). A similar relationship is for a larger number of turns ($n = 70\div 90$). For $h = 12.5$ mm, the efficiency reaches 50% already at $f = 200\div 400$ kHz (Fig. 10.8). However, for twice the distance between the coils, the system reaches 50% efficiency only at 1000 kHz (Fig. 10.14).

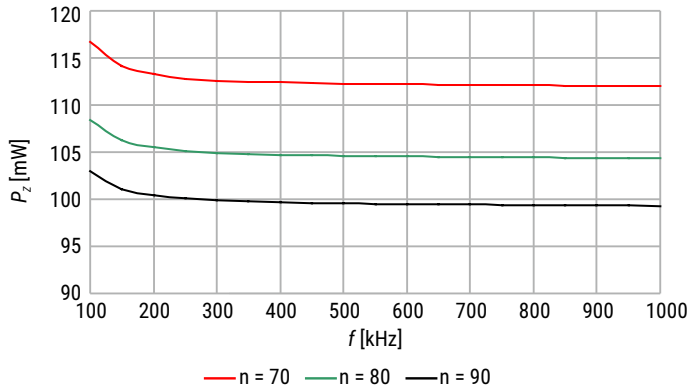


FIGURE 10.6. Results of transmitter power (P_z) dependent on the number of turns ($n=70\div 90$) at distance $h=12.5$ mm

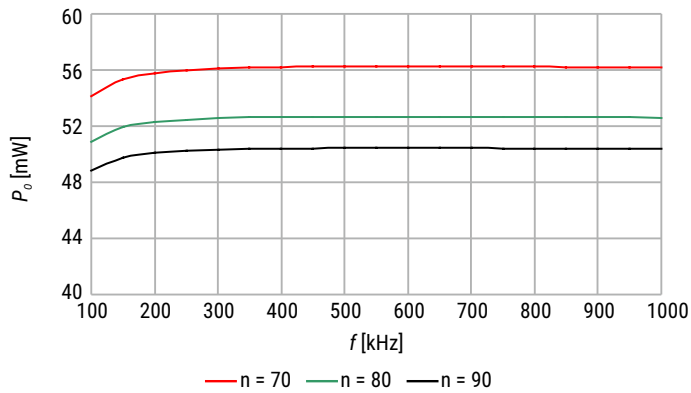


FIGURE 10.7. Results of receiver power (P_o) dependent on the number of turns ($n=70\div 90$) at distance $h=12.5$ mm

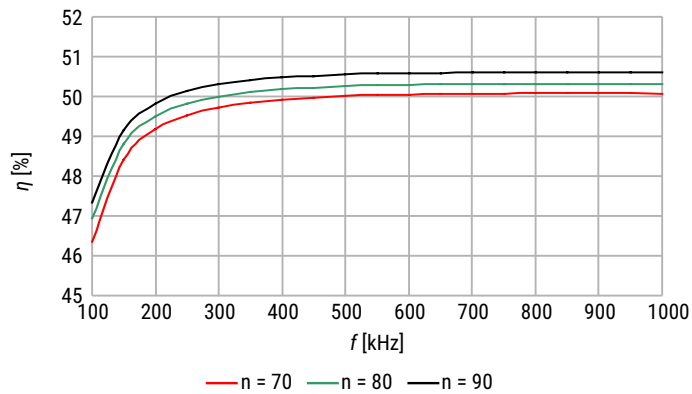


FIGURE 10.8. Results of power transfer efficiency dependent on the number of turns ($n=70\div 90$) at distance $h=12.5$ mm

At $h = 25$ mm, the efficiency of the system has similar values for a different number of turns ($n = 70 \div 90$) (Fig. 10.14), although the receiver power has different values (Fig. 10.13). The efficiency is 50% at 700 kHz when $n = 40 \div 60$ and the distance between the coils is half the radius (12.5 mm) (Fig. 10.5). Whereas for $n = 70 \div 90$, efficiency is higher than 50% already at 300 kHz (Fig. 10.8).

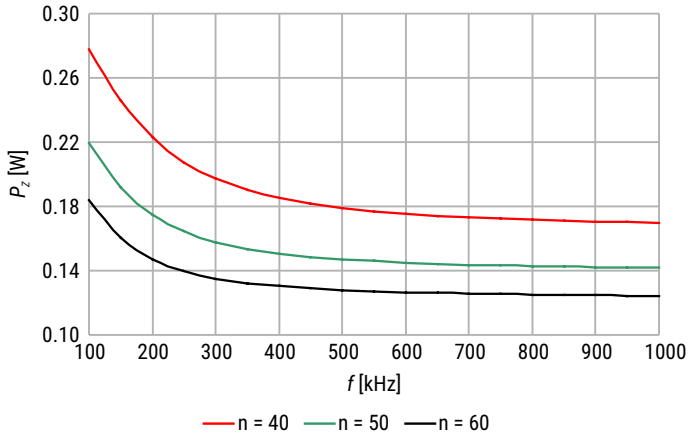


FIGURE 10.9. Results of transmitter power (P_z) dependent on the number of turns ($n=40 \div 60$) at distance $h=25$ mm

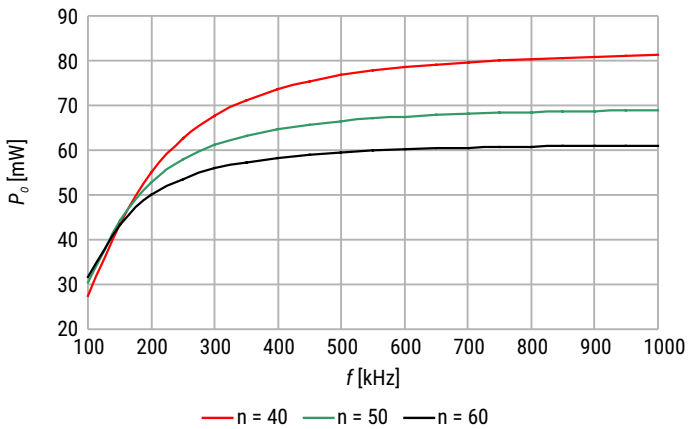


FIGURE 10.10. Results of receiver power (P_o) dependent on the number of turns ($n=40 \div 60$) at distance $h=25$ mm

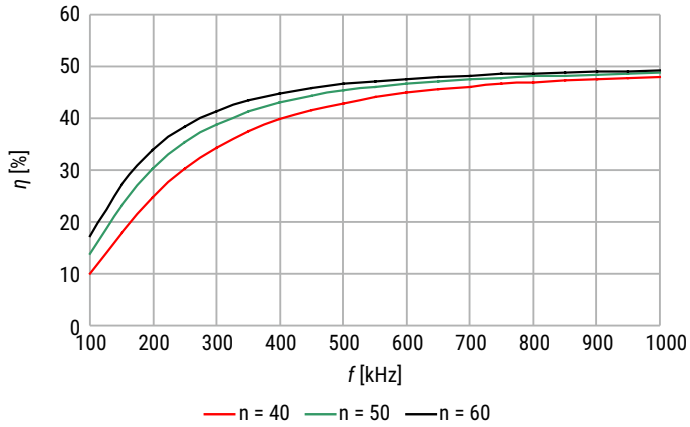


FIGURE 10.11. Results of power transfer efficiency dependent on the number of turns ($n=40\div 60$) at distance $h=25$ mm.

Due to the fact that the characteristics of receiver power were “stabilizing” along with the efficiency tending to 50%, by increasing n it was possible to compensate this effect and broaden the frequency range of the maximum load power.

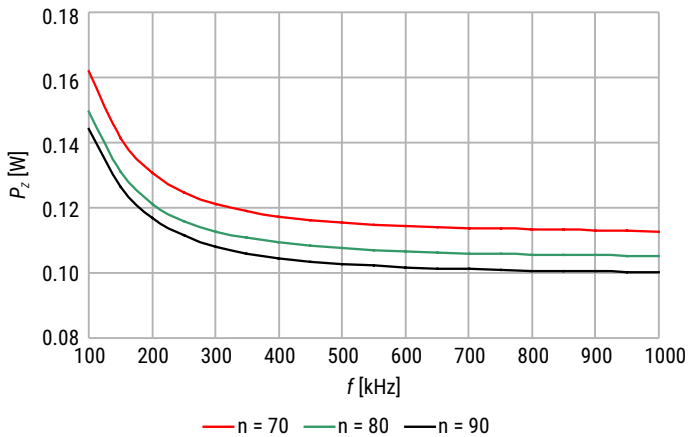


FIGURE 10.12. Results of transmitter power (P_z) dependent on the number of turns ($n=70\div 90$) at distance $h=25$ mm

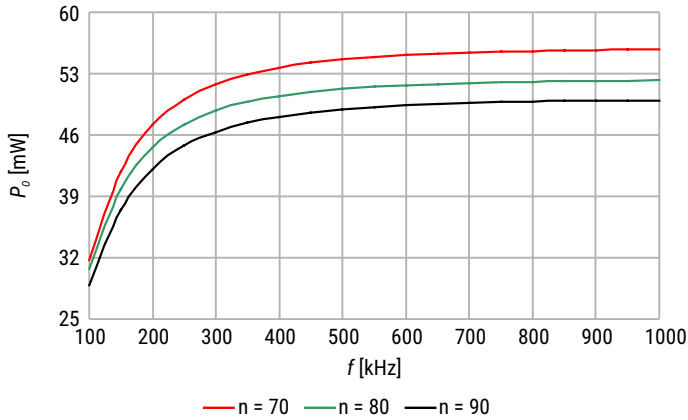


FIGURE 10.13. Results of receiver power (P_o) dependent on the number of turns ($n=70\div 90$) at distance $h=25$ mm

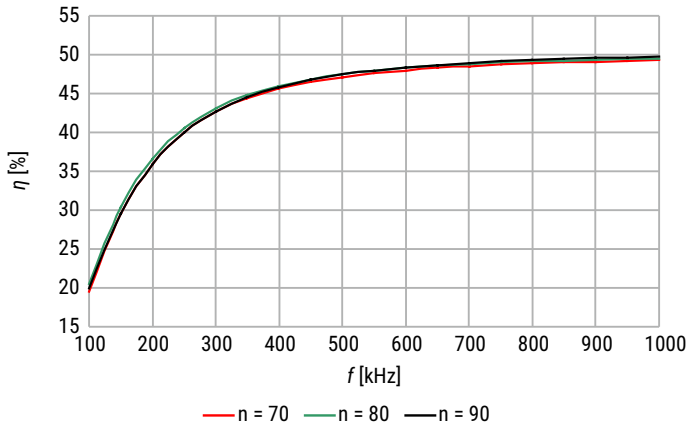


FIGURE 10.14. Results of power transfer efficiency dependent on the number of turns ($n=70\div 90$) at distance $h=25$ mm

Conclusion

The maximum load power in periodic WPT systems was estimated based on exemplary structures with many magnetic couplings between constituent inductors. The models used for solving considered structures, arranged of many spiral planar coils, were developed. The purpose was to quickly determine the output parameters (e.g. power, efficiency) by using analytical equations. The utilization of the electrical circuit, representing a single cell of the WPT system, eliminated the need to make very complex models, which are solved using numerical methods.

The given solutions, adopted in electrical models, allow for studying the influence of coil geometry and a distance between the transmitter and the receiver on power transmission. Calculations were performed over a wide frequency range. The analysis concerned the influence of geometrical parameters of coils in the WPT cell (e.g. number of turns) on the efficiency of the system and the power of the transmitter and the receiver. By simply adjusting the number of turns and increasing the frequency of a current, it was possible to obtain high power transmission for the supplied loads using the proposed system, without the use of intermediate coils or iron cores. By an appropriate selection of load impedance it was possible to determine the power transferred to the receiver and corresponding efficiency.

This work was supported by the Ministry of Science and Higher Education in Poland at Bialystok University of Technology under research subsidy No. WI/WE-IA/11/2020.

Author: J. M. Stankiewicz (e-mail: j.stankiewicz@doktoranci.pb.edu.pl), Bialystok University of Technology, Faculty of Electrical Engineering, Wiejska 45D Str., 15-351 Bialystok, Poland.

References

- [1] S. D. Barman, A. W. Reza, N. Kumar, Md. E. Karim, A. B. Munir, "Wireless powering by magnetic resonant coupling: Recent trends in wireless power transfer system and its applications," *Renewable and Sustainable Energy Reviews*, Vol. 51, pp. 1525–1552, 2015.
- [2] X. Liu, G. Wang, "A Novel Wireless Power Transfer System With Double Intermediate Resonant Coils," *IEEE Transactions on Industrial Electronics*, Vol. 63, pp. 2174–2180, 2016.
- [3] Z. Wenxing, L. Chi Kwan, S. Y. R. Hui, "General analysis on the use of Tesla's resonators in domino forms for wireless power transfer," *IEEE Transactions on Industrial Electronics*, Vol. 60, No. 1, pp. 261–70, 2013.
- [4] C.T.Rim, C.Mi, "Wireless Power Transfer for Electric Vehicles and Mobile Devices," John Wiley & Sons, Ltd.: Hoboken, United States, pp. 473–490, 2017.
- [5] K. Fujimoto, K. Itoh, "Antennas for Small Mobile Terminals," 2nd ed., Artech House: Norwood, USA, pp. 30–70, 2018.
- [6] S. Liu, J. Su, J. Lai, "Accurate Expressions of Mutual Inductance and Their Calculation of Archimedean Spiral Coils," *Energies*, Vol. 12, No. 10, pp. 1–14, 2017.
- [7] "Alternative Energy", EETimes; June 21, 2010.
- [8] S. Mohan, M. Hershenson, S. Boyd, T. Lee, "Simple Accurate Expressions for Planar Spiral Inductances," *IEEE Journal of solid-state circuits*, Vol. 34, No. 10, pp. 1419–1424, 1999.
- [9] C.T.Rim, C.Mi, "Wireless Power Transfer for Electric Vehicles and Mobile Devices," John Wiley & Sons, Ltd.: Hoboken, United States, pp. 473–490, 2017.
- [10] P. Martin, B. J. Ho, N. Grupen, S. Muñoz, M. Srivastasa, "An iBeacon Primer for Indoor Localization," [in:] *Proceedings of the 1st ACM Conference on Embedded Systems for Energy-Efficient Buildings (BuildSys'14)*, Memphis, USA, pp. 190–191, November 2014.
- [11] D. Fitzpatrick, "Implantable Electronic Medical Devices," Academic Press: San Diego, United States, pp. 7–35, 2014.
- [12] M. Kesler, "Highly Resonant wireless power transfer: safe, efficient and over distance," WiTricity Corporation, 2013.

- [13] Z. Luo, X. Wei, "Analysis of Square and Circular Planar Spiral Coils in Wireless Power Transfer System for Electric Vehicles," *IEEE Transactions on Industrial Electronics*, Vol. 65, pp. 331–341, 2018.
- [14] N. Tal, Y. Morag, Y. Levron, "Magnetic Induction Antenna Arrays for MIMO and Multiple-Frequency Communication Systems," *PIER C 2017*, 75, 155–167, 2017.
- [15] Z. Zhang, H. Pang, A. Georgiadis, C. Cecati, "Wireless Power Transfer-An Overview," *IEEE Trans. Ind. Electron.*, 66, No. 2, pp. 1044–1058, 2019.
- [16] D. C. Meeker, "An improved continuum skin and proximity effect model for hexagonally packed wires," *Journal of Computational and Applied Mathematics – Elsevier*, Vol. 236, pp. 4635–4644, 2012.
- [17] D. Kim, A. Abu-Siada, A. Sutinjo, "State-of-the-art literature review of WPT: Current limitations and solutions on IPT," *Electr. Pow. Syst. Res.*, Vol. 154, pp. 493–502, 2018.
- [18] T. Batra, E. Schaltz, S. Ahn, "Effect of ferrite addition above the base ferrite on the coupling factor of wireless power transfer for vehicle applications," *Journal of Applied Physics*, Vol. 117, 17D517, 2015.
- [19] P. Manivannan, S. Bharathiraja, "Qi Open Wireless Charging Standard – A Wireless Technology for the Future," *IJECS*, Vol. 2, No. 3, pp. 573–579, 2013.
- [20] M. M. El Rayes, G. Nagib, W. G. A. Abdelaal, "A Review on Wireless Power Transfer," *IJETT*, Vol. 40, pp. 272–280, 2016.
- [21] S. Liu, J. Su, J. Lai, "Accurate Expressions of Mutual Inductance and Their Calculation of Archimedean Spiral Coils," *Energies* 2019, 12, 2017.

List of Tables

Table 1.1. Measurement results	10
Table 3.1. Recommended illuminance level for football fields [2]	24
Table 3.2. Maximum obtrusive light permitted for exterior lighting installations [3]	25
Table 3.3. Lighting specifications for televised events [4]	26
Table 3.4. Enviromental factor [4]	27
Table 3.5. Average lighting distribution on adjusting streets surrounding the sports school in Bialystok.....	30
Table 4.1. Parameters of elements used in the measurement system.....	45
Table 4.2. The values of the measured supply voltage and line currents	45
Table 6.1. Road lighting classes and their applications in accordance with PN-EN 13201 [2]	67
Table 6.2. Operating requirements of PC classes for the road in class M [3]	68
Table 6.3. Operating requirements of PC classes for the road in class C [3]	68
Table 6.4. Parameters of the road designed in the DIALux software.....	71
Table 7.1. Process for electrical energy efficiency management and responsibilities	83
Table 8.1 Values of active power, reactive power, deformation power, complex power, power factor PF (cosine) and total distortion factor of current THD_1	93
Table 8.2 The results of calculations presenting the approximate influence of modern receivers on the loss of active power in power supply wires	97
Table 9.1. Values used in the calculations	104
Table 9.2. Considered variants of the WPT system.....	105
Table 10.1. Geometrical parameters for analyzed models.....	116
Table 10.2. Values used in the analysis	116

List of Figures

Figure 1.1. Algorithm used to calculate the number of π	7
Figure 1.2. Measurement diagram, PC, ESP32 – tested microcontroller, Zas – laboratory power supply.	7
Figure 1.3. Characteristics of the dependence of calculation time on clock frequency.	8
Figure 1.4. Family of characteristics showing energy consumption depending on processor clock speed including supply voltage.	9
Figure 1.5. Family of characteristics showing energy consumption as a function of supply voltage.	9
Figure 1.6. ESP32 processor power input structure from the manufacturer’s documentation [1].....	11
Figure 2.1. Short circuit loop L – PE in the TN system [3].....	15
Figure 2.2. Measurement of short circuit loop impedance by technical method [3]	16
Figure 2.3. Measurement of short circuit loop impedance by voltage drop method [3]	17
Figure 2.4. Scheme showing the idea of measuring short circuit loop impedance [4]	19
Figure 2.5. Block diagram of the meter implementing the proposed method of measuring the complex value of short circuit loop impedance [4]	21
Figure 3.1. Luminous flux balance.....	28
Figure 3.2. Graph of change in average illuminance as a function of tribune reflection coefficient [7]	29
Figure 3.3. Sports School in Bialystok – view in the DIALux program.....	30
Figure 3.4. Sports School in Bialystok – top view.....	31
Figure 3.5. Improving the energy efficiency of road lighting around the Sports School in Bialystok	32
Figure 3.6. Reduction of energy consumption for road lighting in the vicinity of the Municipal Stadium in Bialystok	32
Figure 3.7. Reduction of energy consumption for road lighting in the vicinity of the Sports School in Bialystok	33

Figure 4.1. LTI load supplied by a four-wire line.....	37
Figure 4.2. Unit symmetrical vectors.....	38
Figure 4.3. Balanced load, equivalent to the original load due to active and reactive power	39
Figure 4.4. The equivalent circuit of the unbalanced load with an asymmetrical sinusoidal supply voltage	42
Figure 4.5. View of the three-phase four-wire system with the asymmetrical sinusoidal voltage source	44
Figure 4.6. Diagram of the measurement circuit from Figure 4.5.....	45
Figure 4.7. The waveform of the instantaneous value of the phase voltage	46
Figure 4.8. The waveform of the instantaneous current value of the line	46
Figure 4.9. The waveform of the instantaneous value of the active current.....	47
Figure 4.10. The waveform of the instantaneous value of the reactive current	47
Figure 4.11. The waveform of the instantaneous value of the unbalanced current of the positive sequence	48
Figure 4.12. The waveform of the instantaneous value of the unbalanced current of the negative sequence	48
Figure 4.13. The waveform of the instantaneous value of the unbalanced current of the zero sequence.....	49
Figure 5.1. A view on the analyzed model with specified dimensions	57
Figure 5.2. Exemplary periodic porous structures: a) $di = 0.65$ mm ($kv = 0.99$); b) $di = 3.25$ mm ($kv = 0.75$); c) $di = 5.86$ mm ($kv = 0.19$)	58
Figure 5.3. Temperature distribution (yz plane) and heat flow conducted through the surface of the structure at $T_{ext} = 20^{\circ}\text{C}$ and $I = In$ in the system: a) without passive cooling; b) cooled by uniform plate; c) cooled by porous heat sink	59
Figure 5.4. Maximum relative temperature for different heat sinks and T_{ext} , $I = In$	60
Figure 5.5. Temperature difference between the hottest and coolest point at the system surface for different heat sink structures at $T_{ext} = \text{var}$ and $I = In$	60
Figure 5.6. Maximum relative temperature for different supply currents and three types of the systems at $T_{ext} = 20^{\circ}\text{C}$	61
Figure 5.7. Temperature decrease effectiveness of a coil with porous heat sink for different supply currents at $T_{ext} = 20^{\circ}\text{C}$	62
Figure 6.1. Example of dedicated pedestrian crossing lighting solution [3].....	66
Figure 6.2. Example of light distribution of luminaires for pedestrian crossing in the PC class [3]	67
Figure 6.3. Geometry of illuminance measurement: a) vertical, b) horizontal.....	69
Figure 6.4. Measurement of the luminance distribution of the observed environment [6].....	70

Figure 6.5. View of the road lighting project in the DIALux software 71

Figure 6.6. Luminance distribution from the driver's perspective 72

Figure 6.7. Value of the average luminance of the pedestrian model and calculated luminance contrasts, pedestrian crossing directly behind the lighting column 72

Figure 6.8. The value of the average luminance of the pedestrian model and calculated luminance contrasts, pedestrian crossing between lighting columns. 73

Figure 6.9. The value of the average luminance of the pedestrian model and the calculated luminance contrasts, pedestrian crossing in front of the lighting column 73

Figure 6.10. The value of the average luminance of the pedestrian model and calculated luminance contrasts, pedestrian crossing with a dedicated lighting system 74

Figure 7.1. Level of efficiency of the electrical installation efficiency classes 77

Figure 7.2. Example of location of the barycenter in an industrial building 80

Figure 7.3. Energy efficiency and load management system overview..... 82

Figure 8.1. Power triangle 87

Figure 8.2. Characteristics of relative increase of active power loss as a function of power factor values 88

Figure 8.3. Power cuboid..... 89

Figure 8.4. Relationship between successive harmonics in three phases 91

Figure 8.5. Diagram of the measuring system..... 92

Figure 8.6. Current and voltage waveforms for LED source..... 94

Figure 8.7. Harmonic spectrum of current received by LED source 94

Figure 8.8. Current and voltage waveforms for LED TV..... 95

Figure 8.9. Harmonic spectrum of current received by LED TV..... 95

Figure 8.10. Current and voltage waveforms for laptop 96

Figure 8.11. Harmonic spectrum of current received by laptop..... 96

Figure 9.1. Audi wireless charging for electric vehicles [9] 101

Figure 9.2. The use of WPT for LED lighting [12] 101

Figure 9.3. Wireless battery charger [12] 102

Figure 9.4. Analyzed WPT system..... 103

Figure 9.5. A single WPT cell containing a transmitting and receiving coil 104

Figure 9.6. Results comparison of transmitter current (I_2) dependent on the number of turns (n_t) for the case $h = 15$ mm. 105

Figure 9.7. Results comparison of transmitter current (I_2) dependent on the number of turns (n_t) for the case $h = 30$ mm. 106

Figure 9.8. Results comparison of receiver current (I_o) dependent on the number of turns (n_t) for the case $h = 15$ mm. 106

Figure 9.9. Results comparison of receiver current (I_o) dependent on the number of turns (n_t) for the case $h = 30$ mm.	107
Figure 9.10. Results comparison of power transfer efficiency (η) dependent on the number of turns (n_t) for the case $h = 15$ mm.	107
Figure 9.11. Results comparison of power transfer efficiency (η) dependent on the number of turns (n_t) for the case $h = 30$ mm.	108
Figure 10.1. Periodic wireless power transfer system	113
Figure 10.2. Analytical model of the WPT cell: (a) overall model of periodic cell, (b) replacement model of the cell for identical transmitting and receiving coils	114
Figure 10.3. Results of transmitter power (P_z) dependent on the number of turns ($n=40\div 60$) at distance $h=12.5$ mm	117
Figure 10.4. Results of receiver power (P_o) dependent on the number of turns ($n=40\div 60$) at distance $h=12.5$ mm	118
Figure 10.5. Results of power transfer efficiency dependent on the number of turns ($n=40\div 60$) at distance $h=12.5$ mm	118
Figure 10.6. Results of transmitter power (P_z) dependent on the number of turns ($n=70\div 90$) at distance $h=12.5$ mm	119
Figure 10.7. Results of receiver power (P_o) dependent on the number of turns ($n=70\div 90$) at distance $h=12.5$ mm	119
Figure 10.8. Results of power transfer efficiency dependent on the number of turns ($n=70\div 90$) at distance $h=12.5$ mm	119
Figure 10.9. Results of transmitter power (P_z) dependent on the number of turns ($n=40\div 60$) at distance $h=25$ mm	120
Figure 10.10. Results of receiver power (P_o) dependent on the number of turns ($n=40\div 60$) at distance $h=25$ mm	120
Figure 10.11. Results of power transfer efficiency dependent on the number of turns ($n=40\div 60$) at distance $h=25$ mm.	121
Figure 10.12. Results of transmitter power (P_z) dependent on the number of turns ($n=70\div 90$) at distance $h=25$ mm	121
Figure 10.13. Results of receiver power (P_o) dependent on the number of turns ($n=70\div 90$) at distance $h=25$ mm	122
Figure 10.14. Results of power transfer efficiency dependent on the number of turns ($n=70\div 90$) at distance $h=25$ mm	122

 Politechnika
Białostocka